Laser Linking of Metal Interconnect: Process Considerations and Failure Analysis using Focused Ion Beam Milling

by

Roy L. Rasera

Submitted to the Department of Materials Science and Engineering
in partial fulfillment of the requirements for the degree of

Master of Science
in Materials Science and Engineering

at the

MASSACHUSETTS INSTITUTE OF TECHNOLOGY

September, 1995

Author ....
Materials Science and Engineering
August 11, 1995

Certified by ....
Dr. Joseph B. Bernstein
Linclon Laboratory Research Staff
Thesis Supervisor

Certified by ....
Carl V. Thompson II
Professor of Electronic Materials
Thesis Supervisor

Accepted by ....
Carl V. Thompson II
Professor of Electronic Materials
Chair, Departmental Committee on Graduate Students

Laser Linking of Metal Interconnect: Process Considerations and Failure Analysis using Focused Ion Beam Milling

by

Roy L. Rasera

Submitted to the Department of Materials Science and Engineering
on August 11, 1995, in partial fulfillment of the
requirements for the degree of
Master of Science
in Materials Science and Engineering

Abstract

A novel method of connecting two adjacent lines on the same level of metallization in integrated circuits using a laser was previously developed with programmable gate array applications and customized chips in mind. This work reports a study of failure mechanisms in the laser linking process. Experiments relating critical processing parameters (laser power and target alignment) to the visual failure modes were performed. A Focused Ion Beam (FIB) was used to cross-section and image failed links. The images were compared with previously published linking models. Finite element analysis was used to simulate laser absorption and subsequent thermal diffusion, and to justify a simple model defining the process window for laser linking. The research correlated theoretical predictions for the failure modes with the critical processing parameters.

Thesis Supervisor: Dr. Joseph B. Bernstein
Title: Lincoln Laboratory Research Staff

Thesis Supervisor: Carl V. Thompson
Title: Professor of Electronic Materials

Acknowledgments

I would like to thank my advisors Dr. Joseph Bernstein and Prof. Carl Thompson for their optimism and encouragement during this project. Without their support, this document would not exist. Appreciation must also be expressed to the National Security Agency and Department of Defense for funding this project.

I would also like to thank Frank Ross for putting up with me as I ranted and raved over the FIB, Janan Denneno for instructing me on the SEM, Yu-Lin Shen and Jeff Hebb for their expertise in the foreign world of modelling, and Barry Colella, Brett Knowlton, Libby Shaw, Tim McClure, Joe Adario, and Pat Kearney for their general guidance on my journey.

Once the packing material arrives, a huge round of applause will be sent FedEx to Don Ferrar, Don Marble, and Kim Tobin at FEI Company for resurrecting the dying FIB. Upon receipt, the applause should be fixed, tested, and returned by FedEx no later than graduation. A fax of all appropriate billing information will be forthcoming.

Similarly, Marilyn Tomlin at MARC Analysis Research Corporation has my undying thanks for waving her magic wand over the internet and dispelling my modelling woes.

Others, such as my parents, my sister, Mary Beth Rhodes, Thomas Chen, Larry Foley, Nathan Shapiro, and the MIT Logarhythms have my debt of gratitude for encouraging, tolerating, and humoring me during this ordeal.

A special thanks to all the teachers I have had in the past who encouraged and believed in me, especially Howard Hintze, Don Jones, Fred Briscoe, Lou Dutrow, Charlie Koppelman, and Linda Thompson. Thank you for expanding my mind, my music, and my soul.

Finally, I would like to thank the rock group Yes for persevering against the popular tide and ID Software for reducing the world's stress and productivity levels by creating DOOM.

Table of Contents

List of Figures

List of Tables

Chapter 1

Introduction

1.1 The Evolution of Laser Linking

Ever since the first coherent laser radiation was demonstrated in 1960, laser developments and applications have grown at a rapid pace. In the area of microelectronics, interest has focused on the future uses of lasers in application-specific circuit design, circuit restructuring, yield enhancement, etching, annealing, doping, patterning, and deposition. Due to its high degree of precision, resolution, and capability for automation, the laser is an ideal choice for many microelectronic processing steps.

Over the past few years, laser applications in the microelectronics industry have become fairly well-defined. Uses have proliferated throughout the semiconductor production line, ranging from laser scribing to laser-assisted mask repair [1]. One of today's more promising applications, however, lies in circuit repair systems. Currently, circuit repair is a labor- and time-intensive process. Laser-assisted chemical vapor deposition (LCVD) is one process for repairing flawed circuits through deposition of new metal lines. In LCVD, the laser is used to accelerate the overall deposition rate through photoadsorption and photodesorption of the precursor gas or dissociated products (see Figure 1.1). This is accomplished by tuning the laser so that it enhances the rate-limiting deposition step of the metallic precursor gas and thereby causes the metal to deposit where the laser beam strikes the substrate [2, 3]. A new metal line may thus be slowly "drawn" on the substrate as the laser spot moves across it. Ion and electron beam systems also utilize the same basic concepts for metal deposition [4, 5, 6, 7]. Unfortunately, many of these systems require ultra-high vacua which make them time-intensive, and therefore uneconomical, processes.

However, lasers retain a clear advantage over particle beams for this purpose in that they do not require vacuum for their operation, and are less likely to damage the substrate.

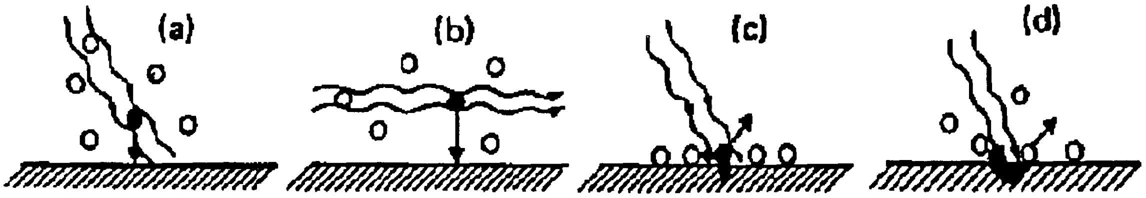

Figure 1.1: Laser excitation of gas phase species (a) with or (b) without the radiation on the surfaces may enhance chemisorption. Resonant excitation of the adsorbate may promote adsorbate-adsorbate and adsorbate-adsorbent interactions as well as molecular desorption (c). Direct laser excitation and heating of the substrate may also induce surface reactions and desorption (d). Resonant excitation of chemical species in the gas phase or in the adsorbed state is indicated by solid dots [2].

A circuit line may be cut with a laser at atmospheric pressure taking comparatively less time than LCVD, which must be done in an evacuated chamber. A finely focused laser pulse of appropriate power and duration is all that is needed to make a "cut." Such a technique was modelled and demonstrated with great efficacy on polysilicide links by C.Y. Lu *et al.* [8, 9] and on aluminum lines by H. Yamaguchi *et al.* [10]. J.D. Chlipala and L.M. Scarfone have done some follow-up reliability testing for polysilicon and polysilicide laser cutting [11]. They concluded that polysilicon links were more reliably cut than silicide-polysilicon links by both infrared and green lasers. As with metal deposition, ion beams may also be used to cut lines by means of sputtering [4, 12].

For some time laser cutting of lines has been applied to programmable redundancy [13]. Chip Express Corp., based in Santa Clara, CA, has taken this line-cutting application to the market with custom laser-programmable gate arrays [14]. However, there are two major drawbacks in using cut-only technology for customizing chips [15]. Since every possible connection must be made when the chip is fabricated, the resulting circuitry is untestable until all laser-cut operations have been performed. This can yield a flawed final product if one of the fabricated connections was actually defective. Furthermore, though laser cutting is a relatively quick process, the multitude of lines that must be cut to produce the desired chip circuitry creates a threshold process-time that cannot be reduced.

Ideally, both line drawing and line cutting systems should be combined and integrated into a semiconductor fabrication/testing line without the need for a vacuum chamber. If this were possible, the number of chips rejected on account of circuit flaws would be dramatically reduced due to the ease and speed of repair. In the push toward modular *in situ* fabrication plants, the potential for applications of such an instrument is enormous [16, 17].

Variations of this "at atmosphere" processing ideal have been successfully created and tested at Lincoln Laboratories [15, 18, 19, 20, 21]. Most of the systems are based on novel methods of cutting and connecting interconnects for wafer-scale integration and programmable gate array applications. For example, J. Raffel *et al.* have developed a laser-restructurable logic array that can be fully tested prior to packaging and is fabricated using a standard complementary metal-oxide-semiconductor (CMOS) process. The technology uses laser cutting and both diffused and vertical forms of "linking." Diffused links are created by laser-melting the silicon between two heavily doped regions (see Figure 1.2). An ohmic connection of 100 to 300 Ω is formed between the two regions after the dopants redistribute within the molten area.

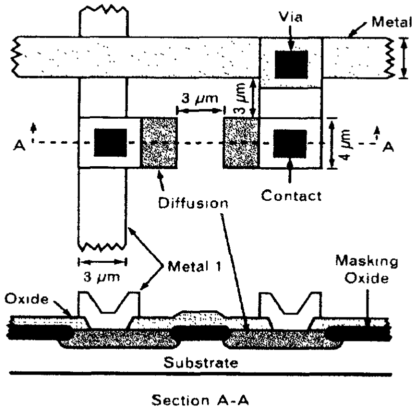

Figure 1.2: Diffused link at two-level metal intersection [15]

Vertical links may be formed where two levels of metallization cross (see Figure 1.3). When Metal 2 is melted by the laser, it alloys with the molten dielectric to form an aluminum-silicon connection to Metal 1. The main disadvantage of this method of linking is that it requires an additional fabrication step to deposit the link dielectric.

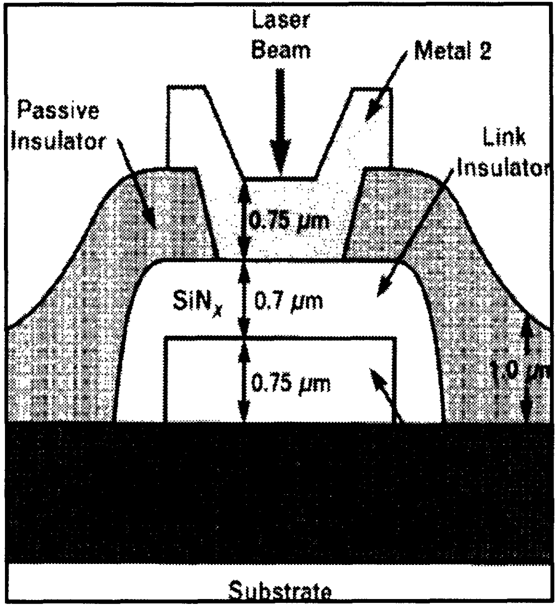

Figure 1.3: Cross-section of vertical link (not drawn to scale) The link dielectric can be silicon nitride or amorphous silicon [15].

A variation of the vertical linking method described above involves crack formation in the dielectric and metal flow through the crack to form the connection. H. Hartmann and T. Hillmann-Ruge, as well as M. Rouillon-Martin *et al.*, helped pioneer this method, though only reached link yields of 95 to 98% [22, 23]. J. Bernstein *et al.* increased the yield by focusing the laser on Metal 1 through an annular region of Metal 2 (see Figure 1.4) [24]. Link yields using these structures have approached 99% and are CMOS compatible.

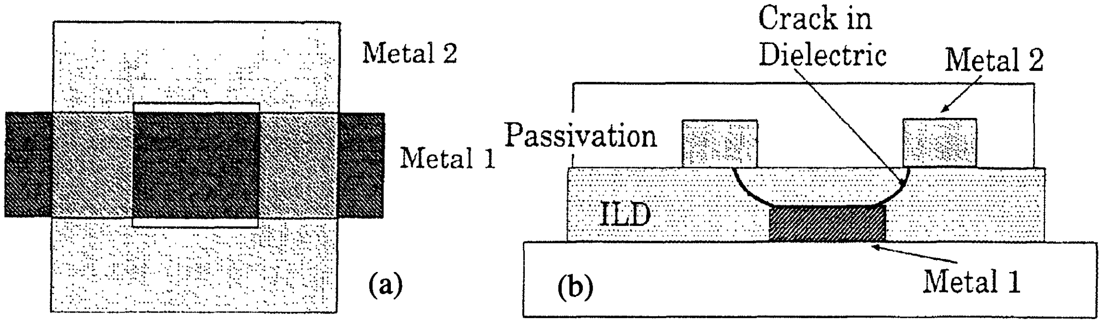

Figure 1.4: Design layout for an improved laser link structure. (a) Top view, and (b) cross-sectional view showing the vertical fracture path and link filament. [24]

There are drawbacks to all of these technologies. Many of them use large geometries in comparison to typical "state of the art" line widths and spacings. Additionally, link yields have not reached industry standards. Some linking methods even require extra processing steps in CMOS fabrication. Reduction of link structure size, increase in link yield, and seamless compatibility with standard CMOS processing steps are crucial elements for widespread utility of laser-restructurable circuits.

J. Bernstein at Lincoln Laboratories has developed a method of connecting adjacent metal lines on the same level of metallization [25, 26]. His method of lateral laser linking, described in Chapter 3, lends itself to incorporation with standard CMOS processing, has achieved very high yields, uses a small-scale link architecture, and has potential for far-reaching applications.

1.2 Objectives and Organization

Reliability is important in microelectronic production equipment, and though the repeatability of the linking process is approaching industry standards [25, 26], the intended connections are sometimes damaged or not successful. The reasons for these failures must be determined in order to reduce their occurrence. The failure mechanisms may be investigated by cross-sectioning and imaging the intended links. A Focused Ion Beam (FIB) was employed to this end. This relatively new instrument is becoming indispensable in the microelectronics industry due to its ability to make cross-sections and depositions on a submicron scale [4, 27, 28, 29, 30].

To observe the modes of failure, failed links were cross-sectioned with a FIB 500D focused ion beam system from FEI Co. The resulting vertical plane-face was then imaged with the FIB or a standard Scanning Electron Microscope (SEM) from Amray Co. Through the correlation of the resulting pictures with the linking test conditions, the reasons for the failures can be identified and their frequency of occurrence minimized.

The research reported here deals specifically with the use of the FIB for cross-sectioning and imaging as well as some simple modelling to determine modes of failure in laser linking. Since the repeatability of the process has nearly achieved industrial tolerances, it is crucial to characterize and categorize the potential failures. Looking at failed or damaged links that were purposefully caused will allow future process engineers to diagnose the problem areas when failures occur. The basic objectives of this research are as follows:

1. To assess the ease of cross-sectioning by means of the FIB as a failure analysis tool;
2. To visually categorize the modes of link failure and damage, and to relate them to the process parameters;
3. To verify or refute previous linking models with experimental data;
4. To create a simple processing window for optimized linking.

Chapter Two covers the operation of the laser table and FIB used for this research. The dynamics of the linking process are discussed in Chapter Three. Models of various aspects of linking are found in Chapter Four. A number of experiments designed to determine failure modes and discussion of their subsequent results are contained in Chapters Five and

Six, respectively. Chapter Seven presents the conclusions of this research and some suggestions for future work.

Chapter 2

Equipment

2.1 Laser Table

2.1.1 Laser Basics

In basic form, a laser consists of three components (see Figure 2.1). One component is the active medium which produces optical radiation under the proper stimulation conditions. This medium may be solid, liquid, or gaseous, although liquid lasers are generally of far too low a power to be of use in microelectronic fabrication. Another crucial element in a laser is the means of pumping. A flash lamp is typically used as a stimulator for solid state lasers and an electrical discharge for gas lasers. Lasing consists of coherent stimulated emission of photons from transitions between upper and lower energy states (see Figure 2.2). These states may be electronic, vibrational, or rotational transitions in atoms, molecules, or ions. The final component of a laser system is a pair of mirrors of specific curvature and reflectivity that provides optical feedback and output coupling.

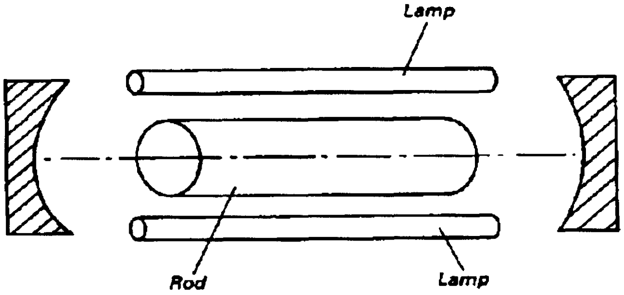

Figure 2.1: Simple schematic of a solid state laser [31].

Solid state lasers, like the Nd:YLF laser used in this research, are more compact but less powerful than gas lasers. They are particularly suited for use in the areas of trimming, marking, and circuit repair. In contrast, the more powerful gas lasers are typically used for welding, cutting, and drilling. For both high and low power applications, laser parameters greatly affect the processing parameters. These are summarized in Table 2.1

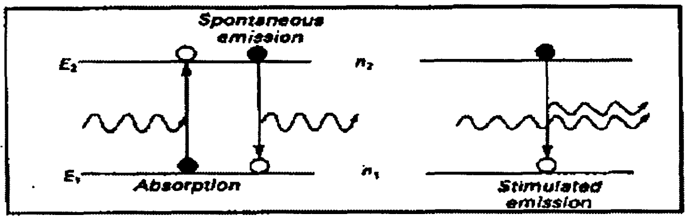

Figure 2.2: Optical process for transitions between two energy levels [3].

Table 2.1: Laser Parameters and Related Processing Parameters [2].

Laser Parameters	Processing Parameters
Power (average) (W)	Temperature (steady state) Process throughput
Wavelength (μm)	Optical absorption, reflection, and transmission Resolution Photochemical effects
Spectral linewidth (nm)	Temporal coherence Chromatic aberration
Beam size (mm)	Focal spot size Depth of focus Beam transformation characteristics Intensity
Mode structures	Intensity distribution Spatial uniformity Speckles Spatial coherence Modulation transfer function
Peak power (W)	Peak temperature Damage Nonlinear effects
Pulsewidth (sec)	Interaction time Transient processes
Stability (%)	Process latitude
Efficiency (%)	Cost
Reliability	Cost

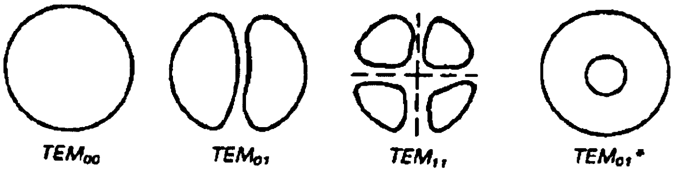

Figure 2.3: Transverse electromagnetic modes [31].

There are a number of ways that the intensity of an electromagnetic wave can be distributed transversely, called transverse electromagnetic modes (TEM). These TEM modes are denoted by two numbers following the acronym, TEM. They represent the number of nodes in perpendicular directions on a plane orthogonal to the laser beam (see Figure 2.3). For processing applications, it is desirable to operate in the TEM_{00} mode. In this mode the irradiance, I, follows the Gaussian distribution described by $I = I_o \exp(-2r^2/w^2)$ where I_0 is the irradiance at the beam center expressed in power per area, r is the distance from the center, and w is the spot radius. A Gaussian amplitude profile (TEM_{00}) is presented in Figure 2.4 in contrast to plots for two other modes.

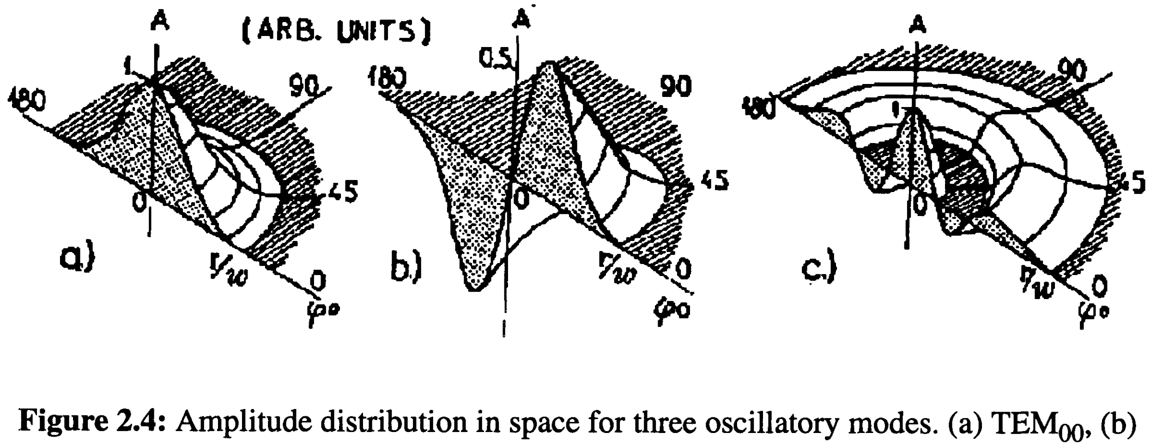

Figure 2.4: Amplitude distribution in space for three oscillatory modes. (a) TEM_{00}, (b) TEM_{10}, (c) TEM_{02} [32].

It is now helpful to examine a laser beam of Gaussian profile (TEM_{00} mode) with peak power, P_0, and spot size, w^2 (see Figure 2.5). The spot size is determined radially from the center of the beam where the beam intensity has fallen to $1/e^2$ of the maximum intensity. Most of the laser power (87%) falls within the diameter of the beam at $1/e^2$ below the peak, and thus this diameter is given when discussing a laser spot size.

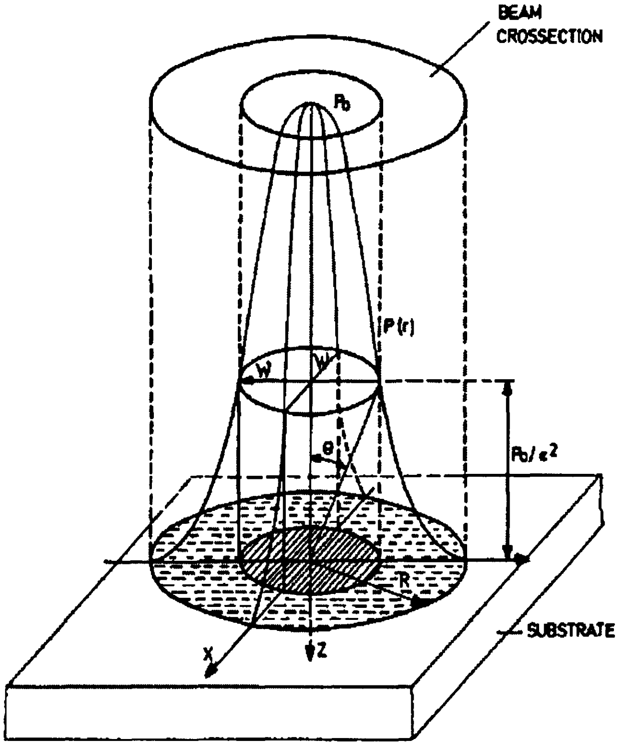

Figure 2.5: Laser Power Distribution [3].

2.1.2 System Setup

A schematic of the laser table is presented in Figure 2.6. The laser was a Spectra Physics diode-pumped Q-switched Nd:YLF laser (λ = 1047nm) operated in the saturated single-pulse mode. The pulses were directed through focussing optics and brought to impinge upon the chip surface. An electrical test socket affixed to an Anorad mechanical stage held the packaged chip during linking. In this manner, the chip could be electrically monitored with an ohmmeter to determine the success or failure of each linking attempt. The computer controlled system was programmed to (1) position the chip precisely under the laser spot, (2) pulse the laser, (3) measure the resistance of the attempted connection, and then (4) move on to the next link site.

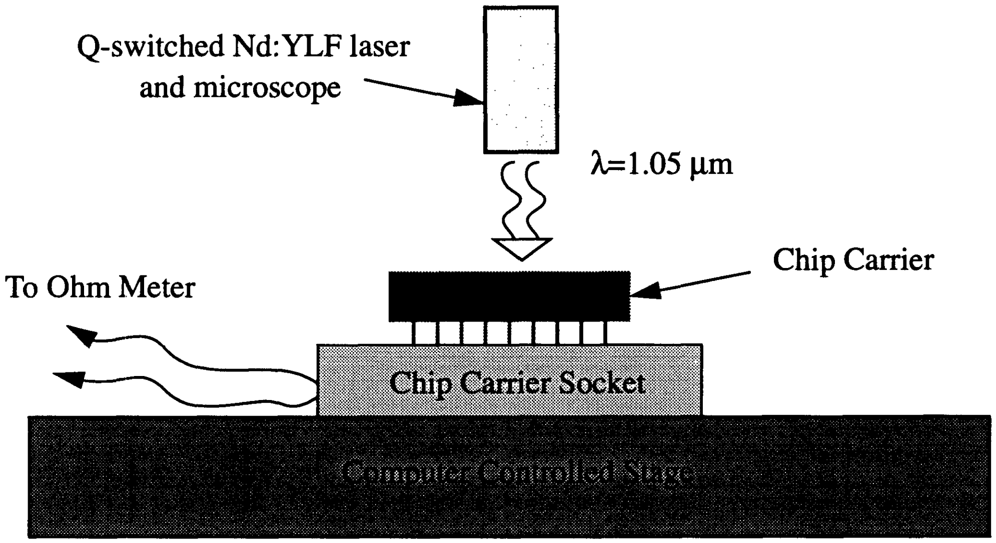

Figure 2.6: Schematic of laser linking setup

2.1.3 Operating Parameters

The laser has many variable parameters: focus, spot size, pulse length, pulse repetition frequency (PRF), and pump power. In these experiments, the focus was maintained constant to reduce the process's variability and will be excluded from this discussion. A $1/e^2$ spot size of approximately 6 μm, a pulse length of approximately 8 ns, and PRF of 180 Hz were also maintained for these experiments. The pump power, however, was varied from 570 to 730 mW in one of the experiments to determine the process window. The fixed parameters were optimized to produce the best linking yield for this setup.

Spot shape and wavelength also play an important role in the laser's effectiveness. To that end, every effort was made to maintain a circular spot shape. This was mainly done through careful alignment of mirrors. The laser's wavelength of 1047nm is adequate for linking because of its transparence in SiO_2 and Si_3N_4 and partial absorption by Al. Section 4.2 will elaborate more on these transparency and absorption issues.

2.2 Focused Ion Beam

The Focused Ion Beam (FIB) is a powerful and versatile tool. Once a beam of ions could be focused to a diameter on the order of submicrons [33, 34, 35], the use of the FIB and its applications in the microelectronics industry increased greatly. Its current utility for small-scale deposition, milling, and imaging have earned it an important and rapidly expanding place in semiconductor technology.

2.2.1 Focused Ion Beam Basics

Figure 2.7 presents a schematic of a typical focused ion beam system. An extraction electrode just below the liquid metal ion source (LMIS) ionizes the metal atoms at the tip of the source by creating the necessary electrostatic field. The beam is then focused and defined using electrostatic lenses and a variable aperture in order to achieve the desired beam current on the sample. Usually, an ion pump is used to keep the focussing column, containing the LMIS, at ultrahigh vacuum (less than 5×10^{-7} torr). With the achievement of such reduced pressure, source corrosion is minimized and the LMIS lifetime is increased. The sample chamber, however, need not be kept at such low pressure; typically, 5×10^{-6} torr is adequate. A differential pumping aperture separates the sample chamber from the focussing column in order to maintain the vacuum in the focussing column if gases are introduced in the sample chamber. A column isolation valve also separates the two chambers. It is opened during FIB operation after the chambers have achieved the required pressures.

The LMIS is a crucial component of the FIB system. It was developed during the 1970's by researchers trying to create liquid metal thrusters. Their research was based on the principle of field emission of a liquid metal film wetting a sharp needle [36]. In 1965 G.I. Taylor noted that electric fields could be used to form cusp-like deformations in conducting liquid surfaces [37]. These deformations later became known as Taylor cones. His predictions and observations became important to LMIS development when the phenomenon was accidentally observed by R. Clampit and coworkers exploring field emission from liquid metal wetted needles. They found that: (1) Blunt needles must be used in order to form and maintain the liquid metal Taylor cone, and (2) if the radius of curvature of the needle's tip is too large, multiple Taylor cones may form [38].

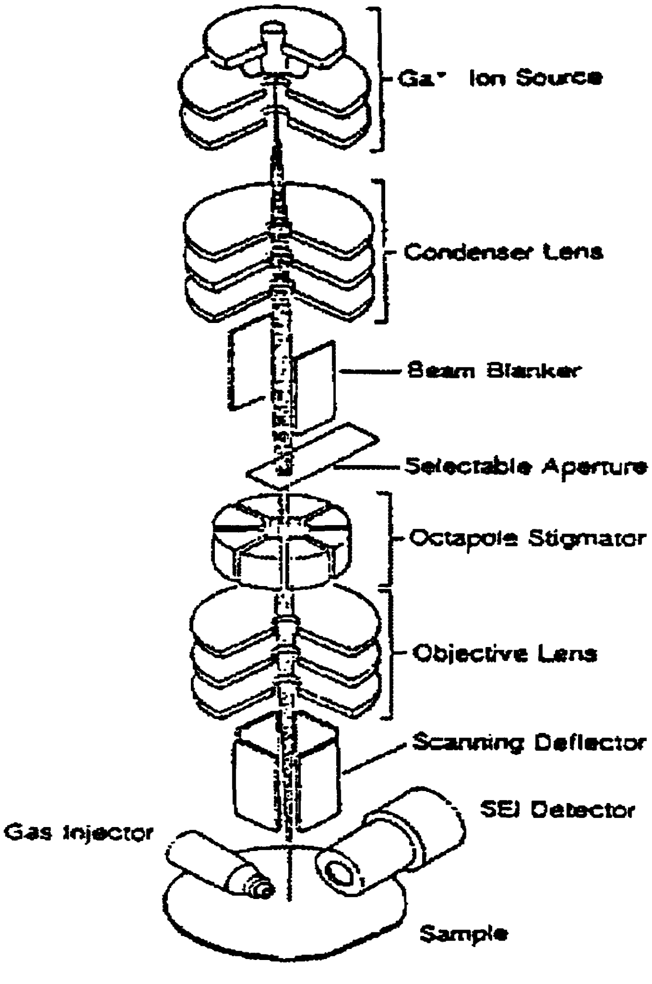

Figure 2.7: Schematic diagram of a typical focused ion beam system [12].

There are two different types of needle liquid metal sources: directly and indirectly heated. The most common directly heated source is presented in Figure 2.8a. In this simple "hairpin" design, the wire and needle are spot-welded together and the liquid metal source is concentrated at this joint. The source metal is heated and melted by passing current through the wire. This is the typical type of source used for Ga^+ LMIS, where both the wire and needle are made of tungsten. Though it has the advantage of simple construction, it is limited in its applications to other metal systems since the frame must be made of a weldable metal with which the LMIS will not react. A variation on this may be seen in Figure 2.8b where a ribbon heating source replaces the hairpin. Hughes Research Laboratory uses this geometry which has more mechanical stability and is slightly more versatile than the hairpin design since no spot welding is necessary [36].

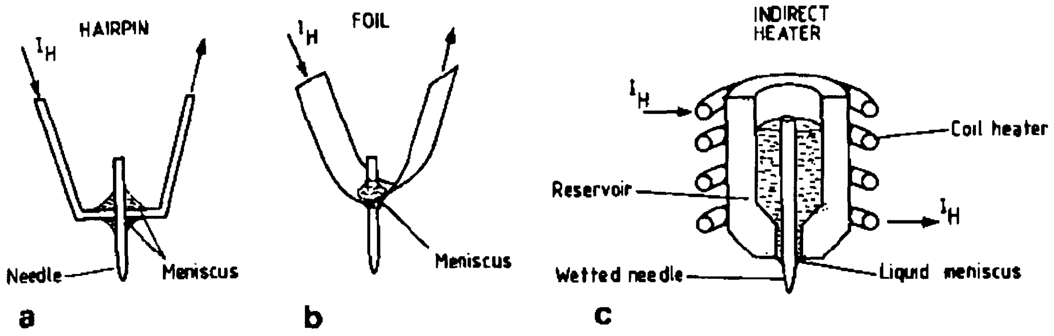

Figure 2.8: Three different forms of needle LMIS: (a) hairpin filament source, (b) Hughes type, (c) Culham type [36].

The indirectly heated source provides much more flexibility in material choice (see Figure 2.8c). Used by UKAEA Culham Laboratory, this source has a potentially much longer life than the directly heated sources, due to the liquid metal reservoir. The reservoir may be made from any appropriate material that can be machined or molded, as opposed to materials that come in wire or ribbon form. Though the needle may be spot welded to the back of the reservoir chamber, it may also be attached in less limiting ways, thereby extending the options for the source material selection. In addition, by having the heating filament outside of the reservoir, the choices of possible materials are expanded still further [36].

In order reliably to form a Taylor cone at the tip of the emitter needle, two requirements must be met. First, as mentioned above, the needle tip must be rounded in a parabolic shape so that the length of the needle shank to its tip forms a continuous, smooth surface. The radius of curvature is typically 1-10 µm. Furthermore, in order to keep the cusp wetted, sufficient pathways, or grooves, must lead from the liquid metal source to the tip (see Figure 2.9). This allows for consistent wetting and Taylor cone formation. Surprisingly, a smooth, ungroved shank has been found to restrict the flow of liquid to the tip, thus limiting the beam's current, causing pulsed emission, or even no emission at all [39, 40].

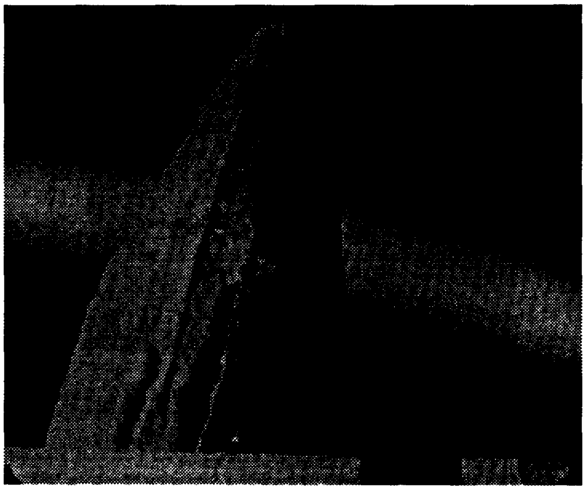

Figure 2.9: Electron micrograph showing grooves on the surface of a tungsten needle. (Note patches of gallium residing in the grooves). Scale: 100 µm [41].

Focused ion beams typically have a diameter between 0.05 and 2 µm, and are primarily limited by chromatic aberration. Since ions of different energies are focused to different points, it follows that heavier ions experience more chromatic aberration than lighter ones because they possess larger spreads in energies. Due to this aberration, the spot size is increased by d_c according to the equation

$$d_c = C_c \alpha \frac{\Delta E}{E} \tag{2.1}$$

where C_c is the chromatic aberration coefficient, α is the beam half-angle, ΔE is the energy spread about the nominal ion energy, and E is the beam voltage. Equation 2.1 clearly shows that operating at a high beam voltage reduces the effect of chromatic aberration, and thus helps minimize the beam size (see Figure 2.12).

Though not as prominent as chromatic aberration, spherical aberration also leads to beam distortion. In this mode, ions passing through a lens obtain different foci depending on their proximity to the lens center. This broadens the beam by d_s where

$$d_s = \frac{C_s \alpha^3}{2} \tag{2.2}$$

and C_s is the spherical aberration coefficient.

By combining the aberration effects and the broadening d_o due to the space charge effect, we can calculate the final beam size d by

$$d = \sqrt{d_o^2 M^2 + d_c^2 + d_s^2} \tag{2.3}$$

where M is the magnification [35, 42].

Higher resolution imaging is obtained with smaller beam size. For this reason the FIB cannot approach the resolution of a scanning electron microscope; however, the resolution is sufficient to utilize the FIB's primary functions: milling and deposition.

2.2.2 System Setup

A model FIB 500D ion beam focusing system by FEI Company was used in this research. Figure 2.10 is a block diagram of the 500D system. The sample must be affixed and grounded to a stud mounted in the specimen chamber before utilizing the FIB. The entire system is then evacuated to pressures less than 5 x 10^{-7} torr in the focusing column and 5 x 10^{-6} torr in the specimen chamber. These necessary pressures are obtained using a mechanical and turbo pump on the specimen chamber, and an ion pump for the focusing column.

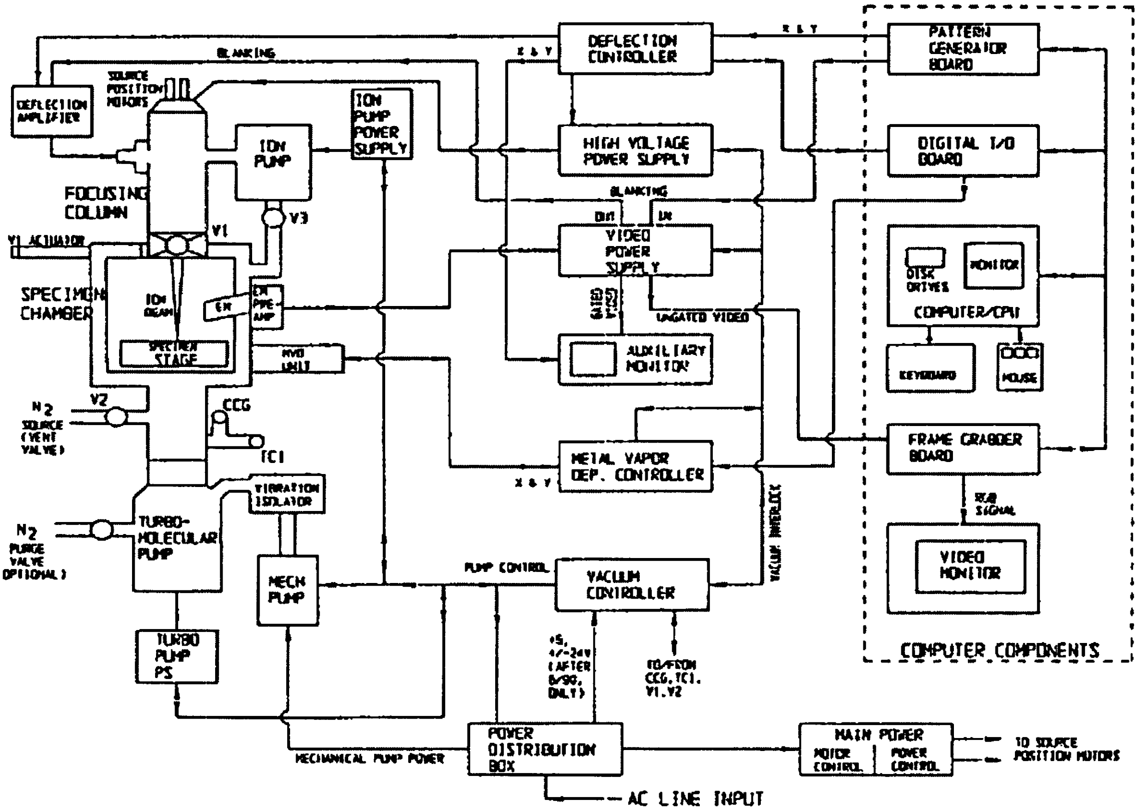

Figure 2.10: Block diagram of FEI's 500D FIB [FEI Company]

The 500D uses a field-emission-based gallium LMIS to create the ion beam. Once the Taylor cone is formed at the tip of the LMIS, a beam is drawn and is then directed through various apertures, lenses, and octupoles before impinging upon the sample (see Figure 2.11).

A standard channel electron multiplier (CEM) is used for imaging. As the ion beam rasters across the sample's surface, both ions and secondary electrons are emitted. The

CEM, depending on the sign of its bias, attracts either the electrons or ions. An image is created based on the electrical signal from the CEM as it collects the charged particles. The collected charge for a specific rastering location determines the brightness of its representative pixel.

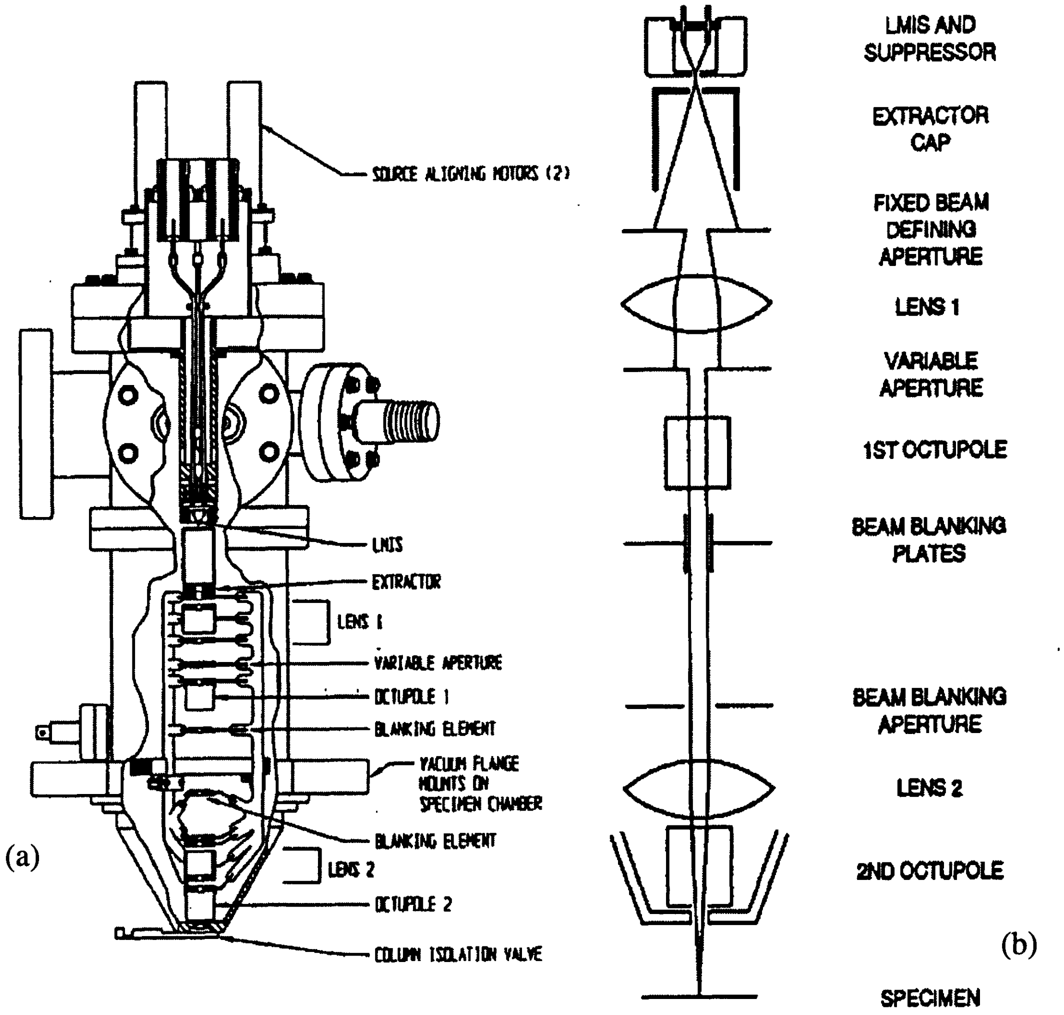

Figure 2.11: The Focusing Column (a) in detail, (b) a schematic [FEI Company].

The 500D has a tiltable stage and height control to adjust the working distance to the sample. This provides the advantage of being able to tilt the sample and view the cross-section that was just created. To aid in obtaining the size and current of the desired ion beam, a variable aperture is provided after the first lens. Under optimal operating conditions, the 500D can achieve magnifications of 20,000X or more, depending on the beam size.

2.2.3 Operating Parameters

The operation of the LMIS is governed by the suppressor voltage, extractor voltage, beam voltage, variable aperture, beam current, and lens voltages. Optimal settings from many of these parameters, suggested by FEI Company, were used for all the imaging and milling done for the present experiments.

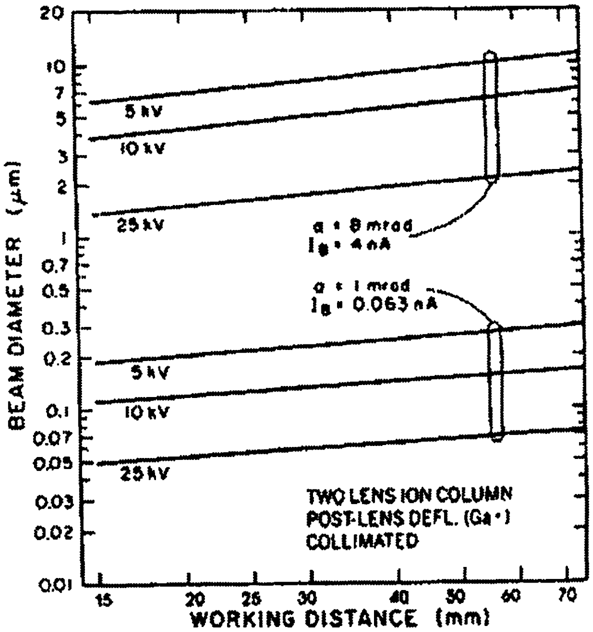

Figure 2.12: Dependence plot of beam diameter, beam voltage, aperture size, and working distance [FEI Company]

In order to maintain a drawn beam, voltages of -1 kV and 10 kV were used for the suppressor and extractor settings, respectively. The highest beam voltage (25 kV) was used because it provided the smallest beam diameter and thus the best performance (see Figure 2.12). Table 2.2 shows the dependence of beam current and lens voltages on aperture size for the suggested working distance of 25 mm, beam voltage of 25 kV, and extractor voltage of 10 kV. FEI Company has also tabulated these for different working distances and other beam voltages.

Table 2.2: 500D lens voltages, beam currents, and aperture sizes for a beam voltage of 25 kV, extractor voltage of 10 kV, and working distance of 25 mm [FEI Company]

Beam Current	Beam Semi-Angle	Spot Diameter	Lens#1 Voltage	Lens#2 Voltage
I_B (pA)	α_0 (mrad)	d (nm)	V_{f1} (kV)	V_{f2} (kV)
15.7	0.49	--	9.81	11.64
63	0.98	64	8.80	11.28
251	2.00	128	8.24	10.88
1005	4.15	362	7.85	10.26
4012	8.80	2010	7.72	9.89

2.2.4 Making a Cross-Section

There are three main steps in milling a cross-section using the FIB 500D: bulk material removal, face polishing, and verification. Bulk material removal is achieved with a large spot diameter and high beam current. This allows for rapid material removal via sputtering. We used the 4.15 mrad aperture for a beam diameter of 362 nm and current of 1005 pA. The 500D has a computer controlled cross-sectioning option where the operator defines a rectangular area to be sputtered, and the computer determines the dwell time, raster overlap, and depth of sputtering based on user-defined parameters.

When an area is defined for cross-sectional milling, it is divided into five horizontal rectangles (see Figure 2.13a). The upper edge of the top rectangle represents the plane of the desired cross-section face as viewed from the top. After the computer mills the entire area to a specified depth, it drops the bottom rectangle from the raster area and continues sputtering the upper four rectangles. This process continues until all rectangles have been dropped. A "stairway" leading down to the cross-section face is the result (see Figure 2.13b). The stairway grading allows the cross-section face to be viewed when the sample is tilted; however, due to the amount of material removed and the large beam diameter, the face of the cross-section often appears smeared. This comes from redepositing sputtered material on the face, as well as poor beam definition. Thus, polishing is required to clarify the cross-sectional features.

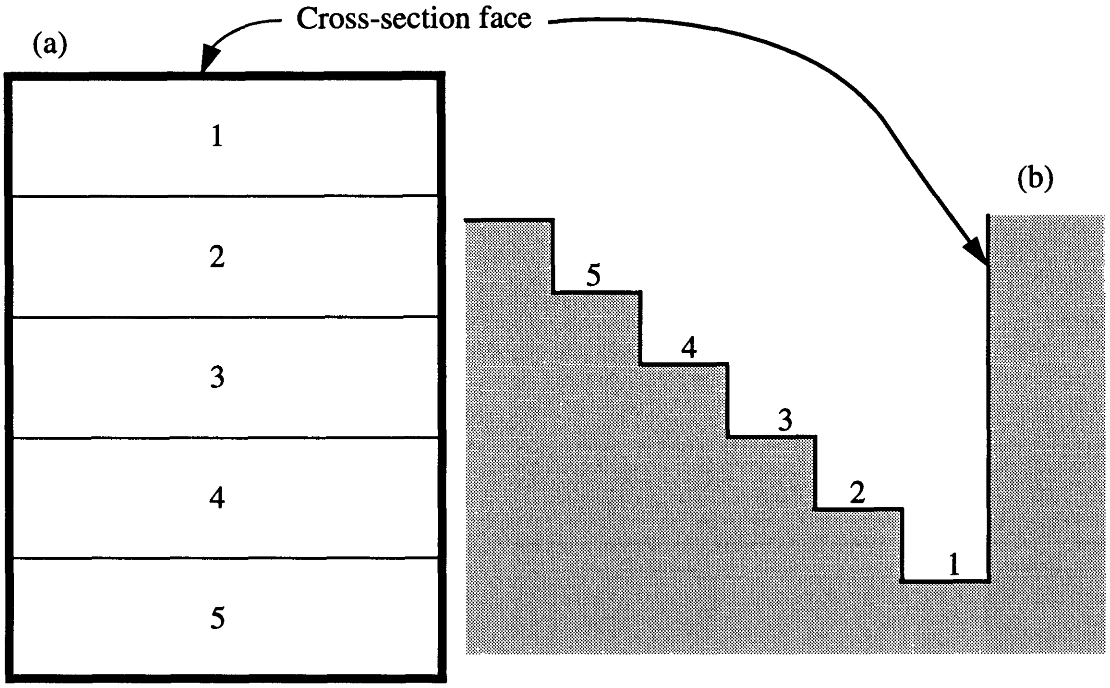

Figure 2.13: (a) User defined milling area divided into five horizontal rectangles. The entire area is milled to a specified depth, the bottom rectangle is dropped from the raster area, and the area is milled again until there are no more rectangles. (b) Schematic side view of resultant "stairway" down to the cross-section face.

A much smaller beam diameter is used when polishing for more precise sputtering. We used the 0.98 mrad aperture for a beam diameter of 64 nm and current of 63 pA. Rather than defining a cross-sectional area, this time only a thin box is defined. The box is drawn directly over the cross-sectional face and should be as wide and as thin as the visible area of the face as viewed from the top. Once defined, the area is milled to a desired depth. This has the effect of polishing the cross-section face and is analogous to using a finer grit sandpaper to smooth a surface.

The final step in cross-sectioning using a focused ion beam is verification of a clean face. By tilting the sample stage, the face may be viewed. If it still appears smeared or it was not milled deep enough, either of the previous two steps may be repeated. If the surface still looked smeared after polishing, the polishing was repeated using a smaller aperture.

It is important to note two things about viewing the cross-section face with the FIB. First, while viewing, the beam is sputtering the material. Viewing of the face must therefore be done very quickly lest the cross-sectioned area of interest be unintentionally sputtered away. Secondly, by passing the beam over the face quickly and at high magnification, it is possible to create greater image contrast between some materials. For example, when initially viewed, cross-sectioned Si_3N_4 and SiO_2 are both black (see Figure 2.14), but after a quick ion bombardment, the Si_3N_4 turns light grey due to surface charging (see Figure 2.15). This can be helpful in some cases or a hinderance in others. In this work, every attempt was made not to charge the Si_3N_4 in order to avoid obscuring the crack and link trajectories.

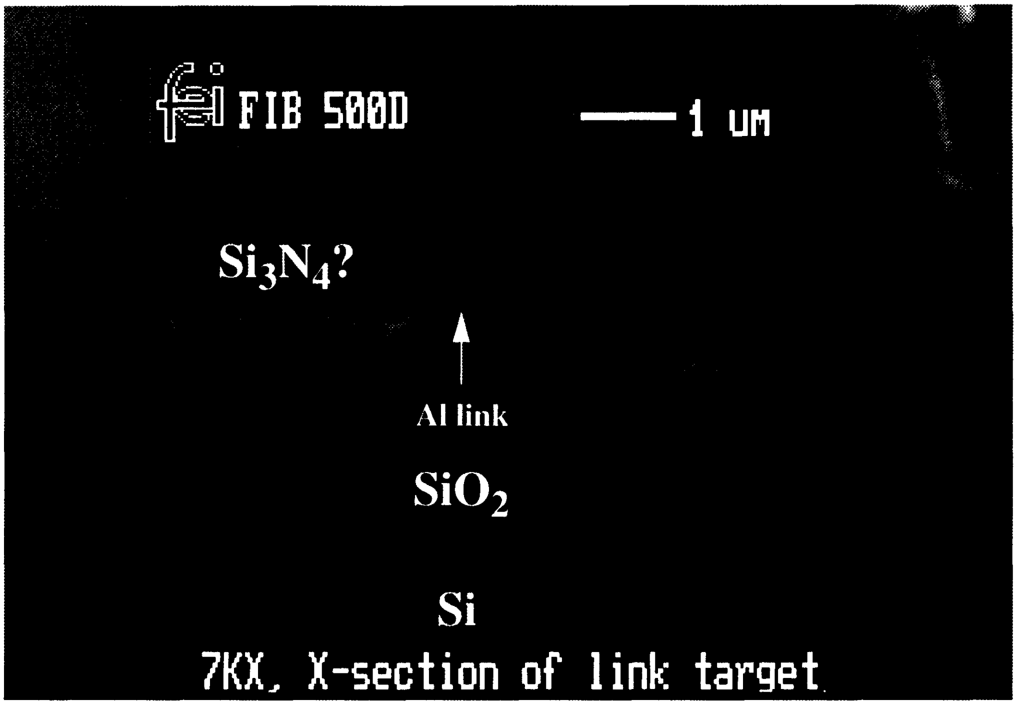

Figure 2.14: Cross-section of a linked line and tab, Si_3N_4 indistinguishable, link visible.

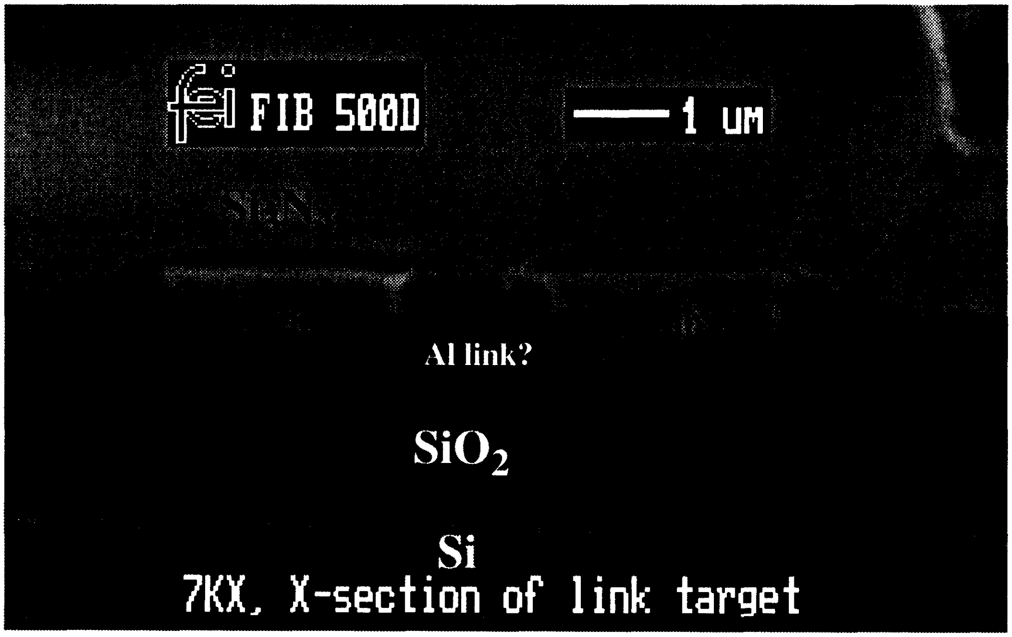

Figure 2.15: Same cross-section of link, Si_3N_4 visible, link indistinguishable.

Chapter 3

The Linking Process

3.1 Chip Architecture

The chips used in these experiments were provided by the U.S. Department of Defense using a standard 2-level metal CMOS process. The lower level of metallization was tungsten (Metal 1) and the upper one was aluminum with 1% silicon and 0.5% copper (Metal 2). The tungsten was deposited on a SiO_2 field oxide grown on the silicon substrate. Between the metal levels was an inter-level dielectric (ILD) consisting of SiO_2. It was deposited using tetraethyloxysilane-based (TEOS) plasma chemical vapor deposition (PCVD) at 390°C followed by a layer of spin-on-glass (SOG). In some areas, an aluminum via connected the Metal 2 lines down to the Metal 1 lines through the dielectric. The upper level of metallization was deposited by sputtering and contained a thin undercoating of TiW and an overcoating of Ti. TiW is a diffusion barrier and provides better contact with Metal 1 at the via, while Ti acts as an anti-reflective coating to increase the efficiency of future lithography steps. Metal 2 was coated with SiO_2 (silane PCVD at 400°C and SOG) followed by a passivation layer of silicon nitride (Si_3N_4, again PCVD at 400°C). The oxide bows down between the line and tab with about a 0.5 μm radius of curvature. This causes a slight dip in the surface of the Si_3N_4 as well. Lateral and horizontal step coverage at the corner of the Al by the oxide are both about 0.1 to 0.3 μm, respectively. The oxide is expected to exhibit a room temperature compressive stress of about 200MPa or less. Figures 3.1 and 3.2 illustrate the chip layout from a top and side view, respectively.

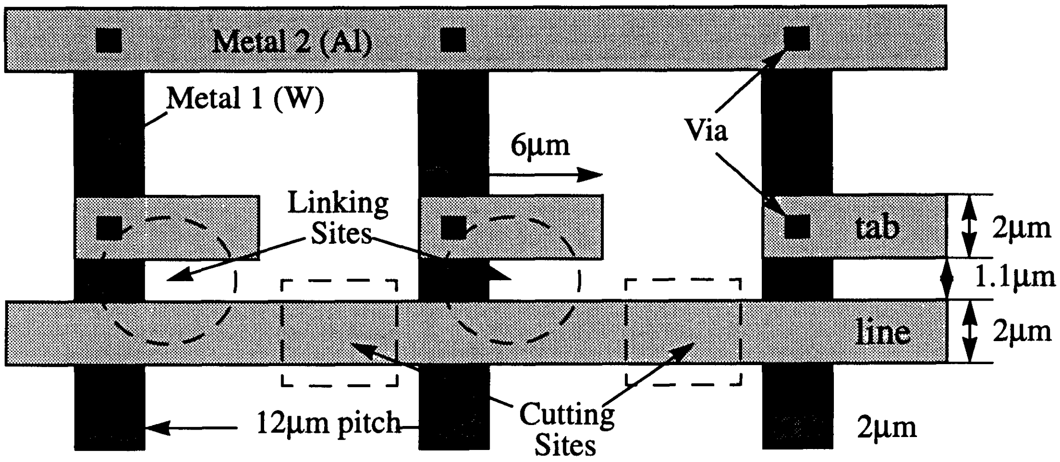

Figure 3.1: Top view of chip layout.

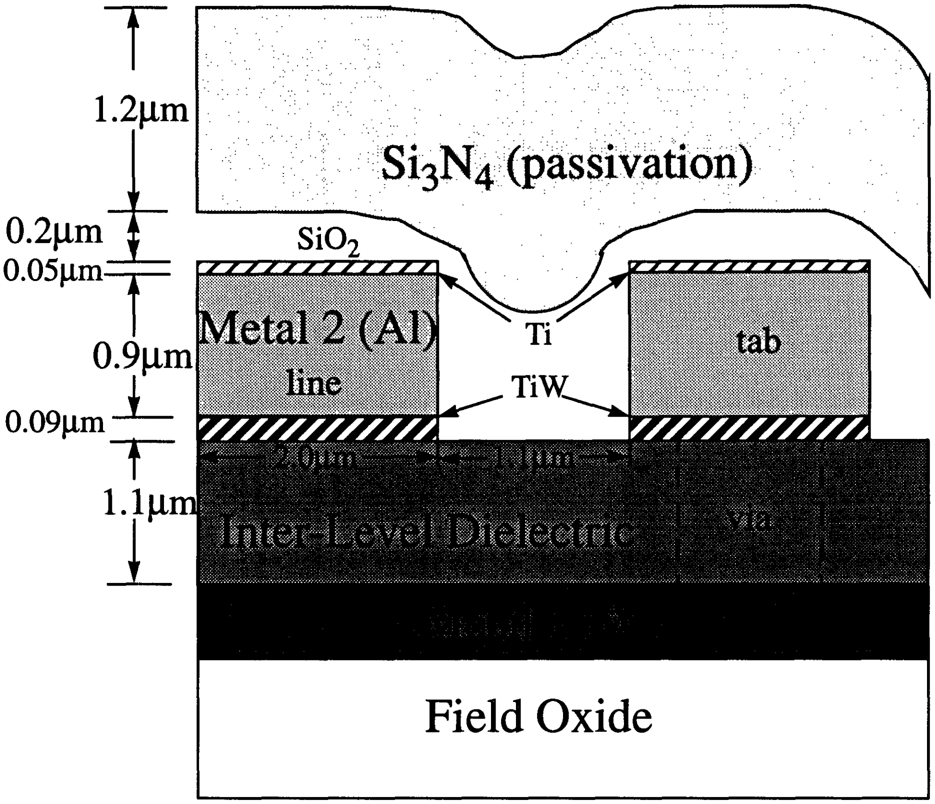

Figure 3.2: Block diagram cross-section of chip architecture with relevant dimensions given (not to scale).

3.2 Making a Link

Though the dynamics are fairly complex, making a link is relatively straightforward. This section provides a simplified overview of the salient steps in the linking process. A more detailed analysis is presented in Chapter 4. Figures 3.1 and 3.2 depict a top and side view of the linking site, respectively, and should be referred to throughout the following discussion.

First, a chip must be mounted beneath the laser, and the distance between the chip and laser must be adjusted so that the laser spot focuses on the linking target. The target in our test structures is a Metal 2 line and tab. Once the spot is centered between and is impinging upon both the tab and line, an 8-ns laser pulse is emitted. The laser energy passes through the Si_3N_4 and SiO_2 until it encounters the surfaces of Metal 2 where it is quickly absorbed. As the aluminum in both the line and tab heats up from the absorbed energy, it expands. Aluminum undergoes a large volumetric increase as it melts (about 6.5%), and the sudden expansion induces tensile stresses within the surrounding SiO_2. The maximum stresses are situated around the upper corners of the Al lines. In order to release the pressure caused by the expanding aluminum, cracks initiate in the SiO_2 from the Al corners. Due to the stress concentration in the oxide, the inner-corner cracks from the line and tab propagate toward each other. Once the cracks meet, a fissure is formed between the tab and line giving the heated and molten Al an avenue for pressure release. When the aluminum flows into the fissure from both sides, it creates a connection from the line to the tab, forming a link.

There are several important process parameters that determine the repeatability of laser linking. Initially, the laser is focused so that placement of its energy can be controlled. A circular spot shape, rather than a distorted or elongated one, must also be achieved for predictable linking behavior. The spot size may then be varied to ensure that it impinges simultaneously upon both the tab and line. Additionally, enough laser power must be provided so that the fraction absorbed by the Metal 2 will create the conditions needed for linking. As one might suppose, the spot size and laser power are inversely related. Finally, the spot should be aligned with the center of the target for optimal linking results. These are the main variables used to determine the process window model proposed in Chapter 4.

3.3 Experimental Steps

As mentioned in Section 2.1.2, the packaged chip is first inserted into a chip socket mounted to the computer controlled laser table. After focusing the beam, positioning the chip, and programming any linking/cutting patterns, we may begin the laser linking. All position movements and link resistances are recorded to a computer data file for future reference.

After all linking attempts are completed, failed or damaged links are analyzed with the FIB and SEM. However, before placing the sample in the FIB, it must be properly prepared. First, the chip must be removed from its packaging. This is accomplished by placing the chip package in a vise with one end protruding. The protruding end is then snapped off by hand. This process continues until the chip can be removed easily from its packaging.

For proper ion beam imaging, the sample must be gold coated (about 10-20 nm thick) to enhance surface charge dissipation. Following gold coating, the chips are affixed with silver paint to a small flat stud. Silver paint provides a direct connection from the chip to ground, since the metal stud is grounded when it is mounted on the FIB stage. This again protects the sample from undue surface charging when under the ion beam.

Once mounted on the FIB stage, the sample chamber is evacuated to less than 5 x 10^{-6} torr. An ion beam is drawn and used to image the sample's surface to find the desired areas for milling. After a cross-section is milled and polished, the stage is tilted 50-70^{o} to image the revealed cross-sectional face. Digitized pictures may be stored for future use. After the samples are removed from the chamber, they are again affixed to a stud with silver paint for the SEM. This stud, however, is at a 70^{o} angle relative to the FIB stud, which allows for quick viewing of all the cross-sections on all of the chips affixed to it. Pictures may then be taken on the SEM if better resolution is needed.

Chapter 4

Models

As depicted in Figure 3.2, the architecture of the test chips involves the use of many different materials. For the sake of simplicity, we will only be considering the three primary materials involved: aluminum, silicon dioxide, and silicon nitride. Their critical material properties are summarized in Table 4.1. Though the aluminum also contains 1% Si and 0.5% Cu, we will treat it as pure aluminum for these models. The reader should be aware, however, that the actual Metal 2 will have a slightly lower melting temperature than pure Al by about 20-60°C.

Table 4.1: Summary of Critical Material Parameters for Laser Linking at 298K

Parameter	Aluminum	Silicon Dioxide	Silicon Nitride
Melting Temp (K)	933.5	n/a	2151 decomposes
Density @ 298K (kg/m^3)	2702	2270	3173
Atomic Vol. (cm^3/mole)	9.986	27.311	44.212
Young's Mod. (GPa)	71.9	72.0	150
Poisson's Ratio	0.34	0.16	0.25
Thermal Cond. (W/mK)	238.00	1.41	22.00
Thermal Diff. (*10^{-6} m^2/s)	98.009	0.6	9.78
Specific Heat (J/g K)	0.899	1.0	0.71
Reflectivity @ 1050μm	~94%	~0%	~0%
Coef.Lin.Therm.Exp. (*10^{-6}/K)	23.55	0.75	3.0

4.1 Model of Cracking

Y.-L. Shen *et al.* at the Massachusetts Institute of Technology have used finite element numerical simulations to predict the crack trajectory for different geometries and process parameters [43]. A summary of these findings is given here in order to provide a deeper understanding of linking and to lend a theoretical justification for the experimental results reported in Chapter 6.

4.1.1 Cracking Model Premises

The nature of laser linking implies that determination of the crack trajectory will necessarily determine the metal's linking path. Additionally, since the difference in thermal conductivity between Al and the surrounding materials is so large (see Table 4.1), SiO_2 and Si_3N_4 remain at room temperature while the Al domain rises in temperature (see section 4.2.1 for justification). It is assumed for simplicity that the temperature distribution in the Al is uniform.

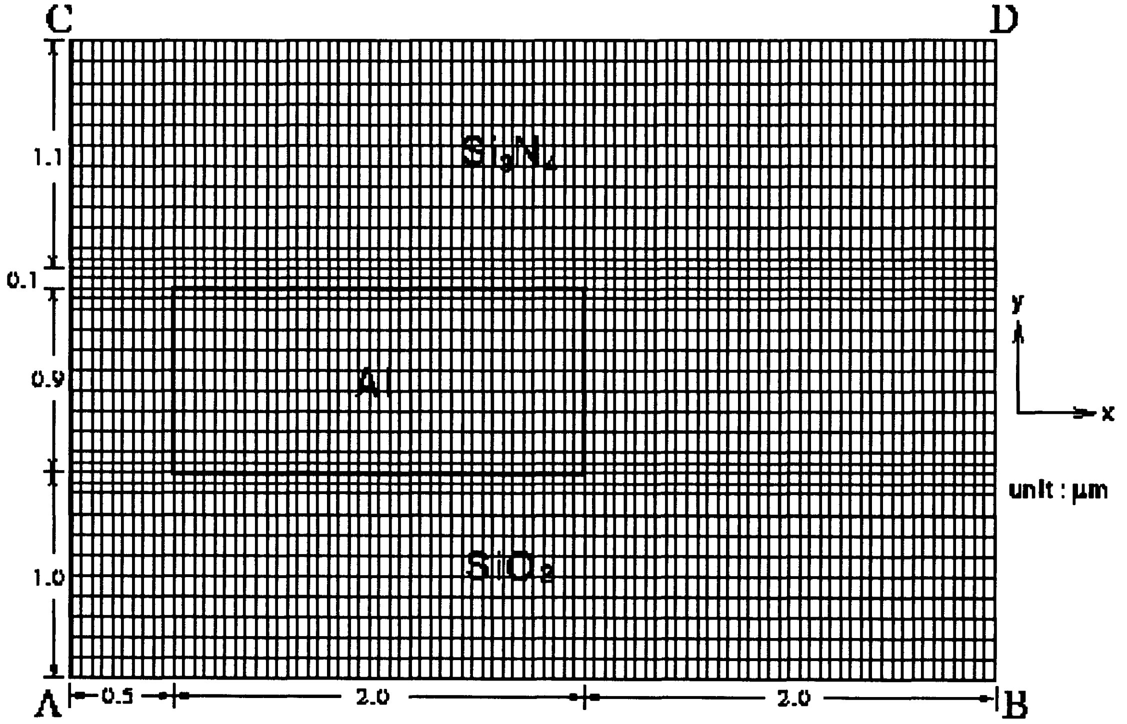

Figure 4.1: Model scale, geometry, and finite element mesh [43].

Figure 4.1 presents the modelling geometry and scale of the simulation structure. The laser-illuminated edge, CD is taken to be a free surface, and AC is the axis of symmetry where displacement in the x direction vanishes. The x displacement at side wall BD is also taken to be zero, meaning that no material past BD is affected by the Al's expansion. This corresponds to a symmetry condition, so the model can be thought of as a periodic array of metal lines in the x direction. The bottom edge AB is fixed to the lower level of metallization and substrate, so no displacement in the x or y directions is allowed.

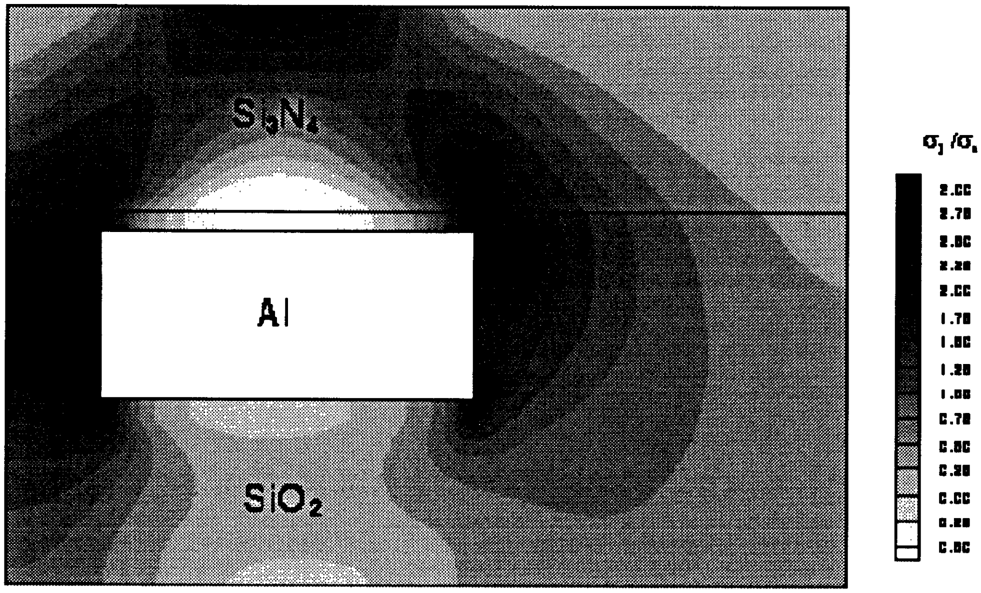

Figure 4.2: Stress contour map [43].

Figure 4.1 also shows the representative finite element mesh. At least 3240 quadrilateral elements are used in all numerical calculations. With data from Table 4.1 and taking into account linear temperature responses for an increase from 20 to 300°C in the Al, a contour map of maximum principal stresses in the oxide and nitride layers was created (see Figure 4.2). In the figure, the maximum principal yield stress σ_1 is normalized to the room temperature yield stress σ_0 of 200MPa for unpassivated, continuous thin film Al [44, 45]. It is apparent that the highest tensile stresses occur near the upper left and right corners and the lower left corner of the Al domain. Initiating from the two top corners, the cracks will tend to move perpendicularly to the local maximum principal tensile stress. Figure 4.3 shows the path of the crack through this localized stress field.

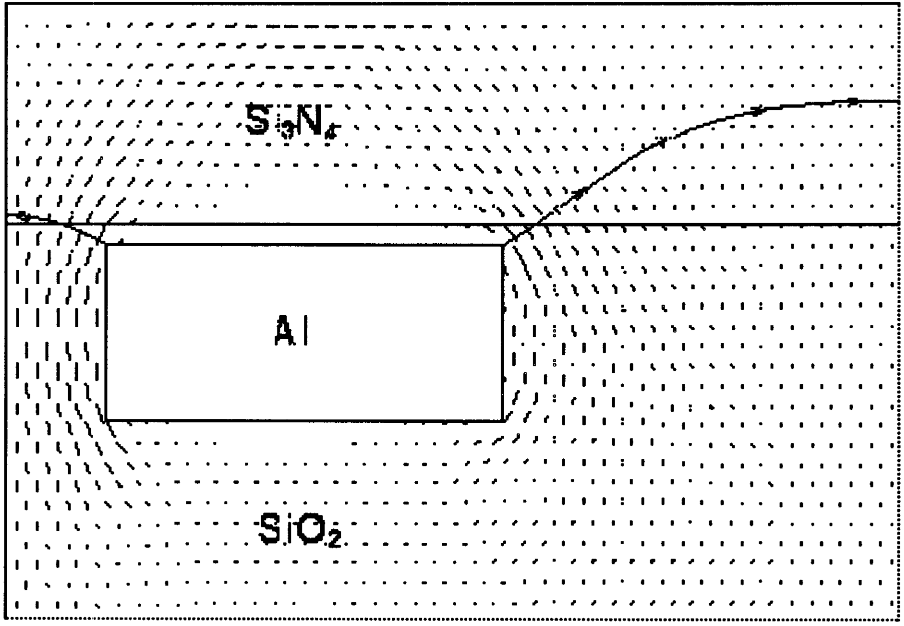

Figure 4.3: Crack trajectory through stress field [43].

A final Al temperature of 300°C was used for all simulations, since simulations done at 400°C and 500°C resulted in virtually the same cracking path.

4.1.2 Cracking Model Under Different Geometries

In order to keep the crack from entering the nitride passivation layer, simulations were run with an additional 1.1 μm of SiO_2 between the Al and Si_3N_4. The results show that although the initial magnitude of the stresses around the Al were slightly reduced, the cracks still followed similar trajectories and never entered the nitride passivation [43].

Another simulation explored the width of and spacing between the Al lines. Other than exhibiting a slightly higher arc in the crack trajectory, the simulation using reduced line widths behaved the same as when using the original line widths. However, when line widths shrank, the principal stresses around the Al diminished. To compensate for the drop in stress, the simulated laser power was increased. Though the stresses increased, it became more likely for cracks to initiate from any of the four corners of the line. This implies that a mid-range laser energy is optimum in order to heat the smaller width Al lines to reach the necessary stress levels without causing unwanted extra cracks from the lower corners. The simulation was also run as a function of line spacing, and results showed that smaller line spacings increase the chances of forming a link [43].

4.1.3 Asymmetric Laser Heating

Simulations were also run with asymmetric laser heating to predict crack trajectory. Such a case results from a laser spot off-center from the linking target. The resulting trajectories are presented in Figure 4.4 and include the suggested increase in oxide thickness mentioned above. It is apparent from the resulting simulations that the likelihood of link formation declines as the laser spot moves further off-center from the target. It was proposed and has been shown that this problem can be reduced by simply increasing the laser beam diameter [25, 43].

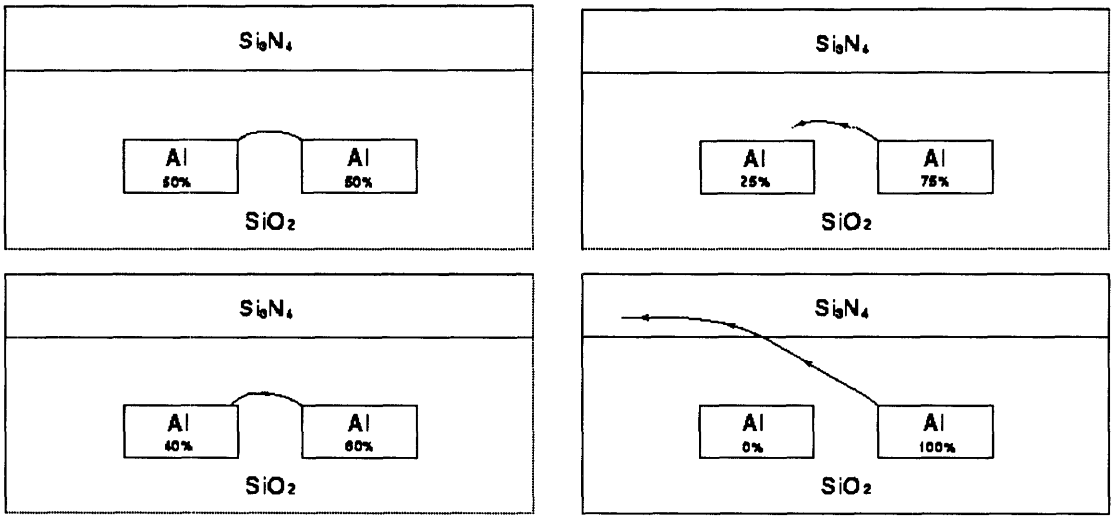

Figure 4.4: Predicted crack paths under asymmetric heating conditions. The percentages correspond to the portions of laser energy absorbed by the metal domains [43].

4.1.4 Crack-inducing Tensile Stress in Silicon Dioxide

Y.-L. Shen calculated the induced tensile stress in the SiO_2 at isothermal Al temperatures of 300, 400, and 500°C (see Section 4.1.1). It was also previously shown that the maximum stresses in the SiO_2 occurred near the Al corners. Taking the average tensile stress over a distance of 0.1 μm near the Al corner for these three temperatures, we present Table 4.2.

Table 4.2: Approximate Tensile Stresses in SiO_2 Over a Distance of 0.1 μm near the Al Corners (Al Temperatures of 300, 400, and 500°C).

Al Temp (°C)	Approx. Corner SiO_2 Tensile Stress (MPa)
300	~550
400	~750
500	~970

Though the failure strength of bulk silica glass is only about 110MPa [46], thin-film SiO_2 (1.5-8 μm thick) is calculated by J. Lloyd and P. Smith to have an ultimate tensile strength of approximately 1,200 MPa [47]. We may thus estimate from Table 4.2 that crack initiation begins at Al temperatures just above 500°C.

Table 4.2 is based on isothermal Al heating conditions and a zero stress condition at room temperature. In reality, this does not occur; the Al is heated preferentially by the laser, and the oxide exhibits a slight compressive stress (<200MPa) at room temperature. Still, the previous discussion should provide one with a general feeling for the temperatures and pressures involved in link-crack formation.

4.2 Models of Heat Transfer

4.2.1 Heat Transfer in Silicon Dioxide

We can determine the effect of heat flow from one body into another using the differential equation for the linear flow of heat,

$$\alpha\frac{\partial^2}{\partial y^2}T = \frac{\partial T}{\partial t}. \qquad (4.1)$$

where α is the thermal diffusivity as defined by $\alpha = \kappa/\rho C_p$, T is the temperature of the system, y is the distance of diffusion, t is the time scale of diffusion, ρ is the density, κ is the thermal conductivity, and C_p is the heat capacity of the material. Equation 4.1 has been solved for the case of heat transport through a semi-infinite solid, yielding the total amount of heat transmitted during the time interval $0 \le t \le t_e$ [48].

$$Q_T = \int_0^{t_e} \frac{\kappa(T_0 - T_i)}{\sqrt{\pi\alpha t}}dt = 2\kappa(T_0 - T_i)\left(\frac{t_e}{\pi\alpha}\right)^{1/2} \qquad (4.2)$$

where Q_T is the total amount of heat transmitted during t_e, T_0 is the temperature at the surface of the transport medium, and T_i is the initial bulk temperature of the transport material. This solution is based on the following assumptions: the heat transport medium acts as a semi-infinite solid, heat loss is only conducted through the transport medium, and the thermal properties of the system are constant. Appropriate boundary conditions may then be defined as

$$T = T_i \quad \text{at} \quad t = 0 \qquad (4.3)$$

$$T \rightarrow T_i \quad \text{as} \quad y \rightarrow \infty \qquad (4.4)$$

$$T = T_0 \quad \text{at} \quad y = 0. \qquad (4.5)$$

We now treat the heating of an Al tab under these conditions. This presentation parallels a similar example put forth by Szekely and Themelis [48]. For this case, the Al tab is assumed to remain at a given temperature during the time interval t_e. The validity of this assumption, and that of a semi-infinite medium, will be demonstrated at the end of the calculations.

We consider the situation where the Al is heated to 1000°C and the SiO_2 is at room temperature (25°C). Since crack initiation is believed to take place within the time frame of the laser pulse, a t_e of 10ns will be used (a laser pulse lasts ~8ns) [25, 26]. Table 4.3 summarizes the rest of the pertinent data. The values given for C_p are average values over the given temperature range; all others are approximated at room temperature. Each parameter was converted to English units to be compatible with Equation 4.2.

Table 4.3: Material Parameters for Heat Transfer Equation

	SiO_2		Al	
Parameter	SI	English	SI	English
Density,ρ	2270 kg/m^3	142 lb/ft^3	2640 kg/m^3	165 lb/ft^3
Spec.Heat,*Cp*	~1 J/(g K)	0.239 Btu/(lb°F)	~29.1 J/(molK)	0.264 Btu/(lb°F)
Ther.Cond.,*k*	1.41 W/mK	0.81 Btu/(ft hr°F)		
Therm.Diff.,α	2.16×10^{-3} m^2/hr	0.0233 ft^2/hr		

We can now calculate Q_T to be 3.05×10^{-2} Btu/ft^2 (157 J/m^2). Multiplying Q_T by the surface area of Al in contact with the SiO_2 (40 μm^2 for a tab), we find a total heat loss of 13.11×10^{-12} Btu (13.8 nJ). To determine the tab's thermal capacity we take the product of its volume, density, and specific heat to arrive at 7.18×10^{-13}Btu/°F (1.36nJ/°C). By dividing the total heat loss of the Al to the SiO_2 by the thermal capacity of Al we find the decrease in Al temperature during time t_e to be 18.3°F (10.1°C). Since the temperature drop is so small, it follows that the assumption of a constant interface temperature was reasonable.

We must now prove that the assumption of a semi-infinite medium is acceptable. To do this, we show that the region of the temperature gradient is smaller than the dimension of the system in which conduction occurs [48]. Again paralleling Szekely and Themelis, we calculate the distance from the interface where the SiO_2 temperature has risen by 5% of the initial Al-SiO_2 temperature difference (1000°C-25°C). From the solution to heat transfer in a semi-infinite medium,

$$T = T_i + (T_o - T_i)\, erfc\left(\frac{x}{2\sqrt{\alpha t_e}}\right) \tag{4.6}$$

where T_i is the initial bulk SiO_2 temperature, T_o is the surface temperature, x is the distance from the surface into the SiO_2, α is the thermal diffusivity of the SiO_2, and t_e is the time of interest, we note that the value of x for which $erfc[x/2(\alpha t_e)^{1/2}]$ equals 0.05 can be calculated as 0.21μm. Within the scale of the system (see Figure 3.2), such a small temperature change over such a short length is insignificant, and thus the assumption for a semi-infinite medium is valid.

This calculation was based on a limiting case, where the Al temperature was assumed to be constant rather than diminishing over time, and the temperature was set quite high at 1000°C. Since this resulted in such a small temperature change in the aluminum and the assumptions were shown to be valid, we may disregard heat dissipation by SiO_2 for all further modelling situations.

4.2.2 Laser Penetration in Aluminum

We will now show that the depth of laser penetration in Metal 2 is small enough to be treated as a surface heat source. As will be recalled, the Al of interest has an overcoating of Ti. Thus, to demonstrate the validity of these calculations for the actual material system, we will determine the extinction depth of our laser in both Ti coated Al and uncoated Al.

Equations 4.7 and 4.8 may be used together to determine the extinction depth of a material. Utilizing the extinction coefficient k and the wavelength of the incident radiation λ in microns, the depth L may be determined. When the penetration depth x is equal to $3L$, 95% of the non-reflected incident irradiation has been absorbed.

$$\frac{1}{L} = \alpha = \frac{4\pi k}{\lambda} \tag{4.7}$$

$$I = I_o \exp\left(\frac{-x}{L}\right) \tag{4.8}$$

For each calculation we will use a wavelength of 1.05 μm. Ti and Al have extinction coefficients of about 3.32 and 10.5 and reflectivities of about 55% and 94%, respectively, for this wavelength [49, 50, 51, 52]. We may now calculate that 6.4% of the incident radiation makes it through the 0.05 μm layer of Ti (L=0.0257 μm). Of the transmitted radiation, 94% is reflected back into the Ti and the rest is immediately extinguished in the Al. For the case of plain Al with 94% reflectivity (L=7.96 nm), all of the penetrating radiation is absorbed within the top 0.02 μm.

Using the method presented by P. Yeh for wave extinction, interference, and attenuation for multilayered media [53], J. Hebb at the Massachusetts Institute of Technology has developed a computer simulation that may be used to determine the final percentage of radiation transmitted through a one-dimensional material stack [54]. Three simulations were run using this model to reinforce the validity of the previous calculations. To make the simulations more realistic, 0.2 μm of SiO_2 and 1.2 μm of Si_3N_4 were added above the Ti/Al layers. Though essentially transparent at the laser's wavelength, Si_3N_4 and SiO_2 contribute some reflection and interference effects which slightly reduce the irradiance hitting the metal.

The simulation's material stacks are presented in Table 4.4 and the resulting percentages of reflection, transmission, and absorption are tabulated in Table 4.5. A wavelength of 1.05 μm was used in these calculations. Again, we may note from Simulation 3 that most of the radiation is absorbed in the top 0.05 μm of the metal layers.

Table 4.4: Multilayer Material Stacks for Transmission Simulation

Simulation 1	Simulation 2	Simulation 3
1.2 μm Si_3N_4	1.2 μm Si_3N_4	1.2 μm Si_3N_4
0.2 μm SiO_2	0.2 μm SiO_2	0.2 μm SiO_2
0.9 μm Al	0.05 μm Ti	0.05 μm Ti
	0.9 μm Al	

Table 4.5: Results of Multilayer Stack Transmission Simulations

	% Reflected	% Transmitted	% Absorbed
Simulation 1	97	0	3
Simulation 2	67	0	33
Simulation 3	65	4	31

From both of these methods it is evident that the radiation only affects the top 0.05 μm or less of the metal system. Since the Ti/Al/W line is 1.04 μm thick, we can safely assert that the laser radiation acts as a surface heat source of insignificant depth.

4.2.3 Laser Melt Depth in Aluminum

A method for calculating one-dimensional laser melt depths in common metals has been demonstrated in the literature [55, 56]. Utilizing the assertion that our laser acts as a surface heat source and assuming a constant laser flux, we may calculate the time needed for the surface of an aluminum film to reach its melting temperature using Equation 4.9.

$$T(0,t) = \frac{2I_o(1-R)}{\kappa}\sqrt{\frac{K_d t}{\pi}} + T_o \tag{4.9}$$

where I_o is the laser flux, R is the reflectivity, κ is the thermal conductivity, K_d is the thermal diffusivity, t is the time, and T_o is the ambient temperature. Using the appropriate values for our situation ($I_o = 2.2 \times 10^8$ W/cm^2, $R = 0.94$, $\kappa = 2.38$ W/cm-^{o}C, $K_d = 0.98$ cm^2/sec, $T_{melt} = 660^o$C, $T_o = 25^o$C), we obtain a time of 10.5ns needed to melt the surface of the Al.

To make the calculation more realistic, we reduce the reflectivity to 84% to account for the more absorbent Ti overcoating. This brings the surface melt time to 1.4ns. Using Equation 4.10 we may calculate the approximate melt depth at the end of 10ns to be 0.95μm, the thickness of the Al line/tab.

$$T(x,t) = \frac{I_o(1-R)}{\kappa}\left[\sqrt{\frac{4K_d t}{\pi}}\exp\left(\frac{-x^2}{4K_d t}\right) - \left(x \cdot erfc\frac{x}{\sqrt{4K_d t}}\right)\right] + T_o \tag{4.10}$$

These calculated values have been considerably overestimated for our situation since neither the latent heat of melting nor the temperature dependence of thermal constants was included. Further overestimation is caused by using a constant laser flux over the pulse time rather than the actual pulse's rise and fall. This overestimation of the melt depth is reduced somewhat by the assumption of a semi-infinite Al film instead of using the actual geometry. By estimating the reflectivity of the Ti/Al system, further imprecision was added. Figure 4.5 depicts more precisely determined melt depths vs. irradiation time and power for Al, Fe, and Ni. It is reassuring to note that submicron melt depths are typical for Q-switched lasers. However, to characterize fully the thermal profile and lend credence to the previous calculations, we present a detailed finite element analysis in the next section.

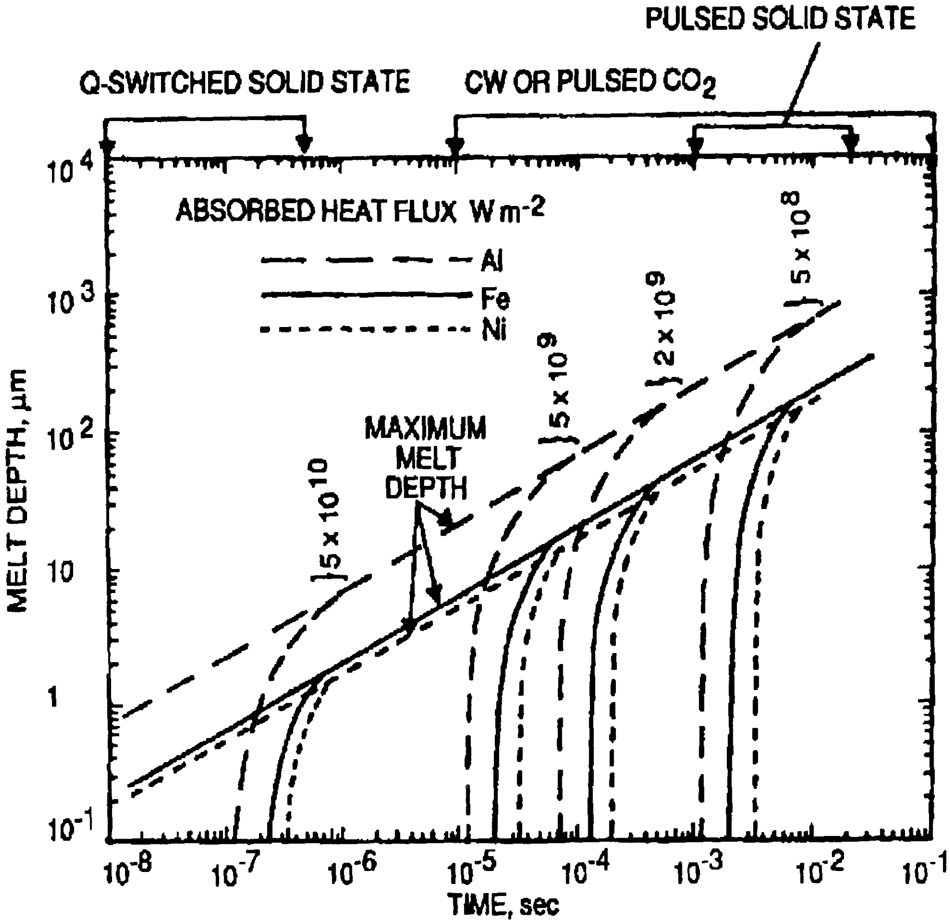

Figure 4.5: Calculated melt depths vs. irradiation time for Al, Fe, and Ni; based on a one-dimensional computer heat flow model [55, 56].

4.2.4 Finite Element Model of Heat Transfer in Aluminum

MARC Analysis Research Corporation's Mentat II software was used to create finite element models of heat transfer in cross-sections of Metal 2. We developed three two-dimensional simulations to determine the thermal profile within the Al at various times during, and following, the laser pulse. The negligible effect of heat transfer through SiO_2 was also established. Additionally, we learned what role the Ti overcoating plays in laser power absorption and temperature change in Metal 2.

By measuring an energy of 225 nJ over a 10-ns pulse from an XRL Nd:YAG laser, we calculated and used a laser flux of 2.2 x 10^8 W/cm^2 for each simulation. To mimic the pulse shape over 10ns, Mentat II was instructed to increase the flux linearly from zero (at time zero) to 2.2 x 10^8 at 4ns and then linearly return to zero in the next 6ns. This skewed triangular pulse shape over 10ns is a good approximation of the actual pulse shape detailed in the XRL manual.

Specific heat, latent heats, density, and thermal conductivity data were included for Al, SiO_2, and Ti. Since it is well documented, the variation of specific heat and thermal conductivity with temperature was utilized for aluminum. For Ti, the values for specific heat and thermal conductivity were taken at room temperature for the solid phase, and the melting temperature for the liquid phase. Only the room temperature values presented in Section 4.2.1 were used for SiO_2.

In each simulation, the overall geometry was the same. A rectangular SiO_2 trough with 0.2 μm thick walls cupped the 2 μm by 0.95 μm cross-section of Metal 2 (see Appendix A, Figure 1). Laser flux was incident on 1 μm of the metal at its top left edge. A 20ns time window was used in order to observe the thermal diffusion during the 10ns laser pulse and subsequent thermal diffusion for 10ns after the laser flux ended. 4,416 square finite elements were used in each analysis, as depicted in Appendix A Figure 1.

Only aluminum and silicon dioxide were included in the first simulation. A reflectivity of 97% was used for the Al as determined in Section 4.2.2. The top 0.05 μm of metal was converted to Ti for Simulation 2 and 3. The Ti reflectivity was based on tabulated data (55%) for Simulation 2, and calculations in Section 4.2.2 (67%) for Simulation 3.

Figures 2 through 10 in Appendix A present three resultant thermal profiles for each simulation at 4ns (the peak of the laser flux; Figures 2-4), 10ns (the end of the laser pulse; Figures 5-7), and 15ns (5ns of thermal diffusion after the end of the laser pulse; Figures 8-

10). The surface Al in Simulation 1 only increased 125 degrees at the peak of the laser flux. Visual analysis of Figures 2, 5, and 8 leads to the conclusion that for the given laser parameters and geometry, pure Al will not crack the SiO_2 since the required temperature range is not approached. This is clearly due to the high reflectivity of the Al.

Simulations 2 and 3 demonstrate the importance of including the Ti layer. Due to the lower reflectivity in these simulations, peak temperatures of 3500K and 2800K were reached at the surface of the Ti after 4ns (see Figures 3 and 4). This in turn increased the temperature of the Ti-coated Al well past its melting point. Both cases more than satisfy the temperature conditions for crack formation from the upper left corner. Though high temperatures were achieved, at no time in either simulation did the Ti or Al reach their boiling points.

Some other points of interest must also be noted. Inspection of the figures in Appendix A will verify the assertion that heat dissipation through SiO_2 is negligible when compared to the metal temperatures and areas involved. Another important and related effect of the boundary SiO_2 lies in its reflection of most of the heat back into the metal. As is clearly seen in Appendix A's figures, though the flux is uniformly incident on the top left half of the metal, the area closer to the SiO_2 reaches much higher temperatures. This in turn enhances heat diffusion directly below the incident flux rather than forming a radially uniform thermal profile. The result of this is that temperatures a given distance below the irradiated surface are much higher than the temperatures the same distance diagonally or laterally away from it. In essence, the area of molten Al is contained by the edges of the laser flux.

The last two figures in Appendix A detail the thermal profiles 5 ns after the laser pulse. Of most importance is the temperature of Al at the right edge of the cross-section. The upper right corner will crack if high enough temperatures and stresses are reached. As will be seen in Chapter 6, cracks from the outer-corner of Metal 2 are not desired. With the upper left crack relieving the pressure within the Al, the occurrence of unintended cracking from the right corner is reduced. However, for larger fluxes or greater areas of irradiation, a single crack may not suffice for pressure release and the outer-corer will crack.

Based on the calculations in Section 4.1.4, and requiring a temperature greater than 500°C (773K) to induce cracking, we conclude from these simulations that the entire depth below the laser beam will reach this temperature but that only about 0.3 μm of the metal beyond the edge of the flux will be similarly affected at the end of the 10ns laser pulse. However, since the metal at the irradiated corner reaches temperatures well beyond those needed for crack formation within the first 4ns, we expect crack formation and metal flow to begin within that time frame. By filling the crack, the flowing Al will reduce the volume of Al in the Metal 2 cross-section. Subsequently, the heat from the continuing laser pulse will have less bulk metal in which to dissipate and thus is expected to raise the temperature of the remaining metal. For this reason we assert that the 500°C boundary for lateral diffusion is actually slightly greater than 0.3 μm after 10ns. A value of 0.5 μm will be used in all further calculations.

Aside from augmenting the effects of temperature on Ti and SiO_2 data, three other refinements, beyond the scope of this work, could be added to this model. The first deals with the variation of laser intensity as a function of distance from the center of the beam. As mentioned in Section 2.1.1, the power distribution of a TEM_{00} laser beam is Gaussian, but in these simulations we used a uniform power distribution within the $1/e^2$ spot diameter. Including this would allow for more detailed analysis of laser-offset effects.

The second level of refinement includes an SiO_2 layer atop the Ti. The layer was omitted from this model because it poses insurmountable problems in Mentat II: since the flux was induced in the top edges of the Ti elements, bordering SiO_2 elements would share the same edge and would also experience the same flux. In effect, both the Ti and SiO_2 would be absorbing the laser energy. However, we know that this does not happen since SiO_2 is transparent to the laser radiation. Another modelling program or collaboration with MARC Analysis Research Corporation might alleviate this problem.

Finally, inclusion of induced stresses and crack formation would increase this model's utility in simulating the linking process. The problems caused by adding an over-layer of SiO_2 would have to be overcome to refine the model in this way.

4.3 Model to Determine Process Window

In this section we propose a method for approximating a process window based on laser spot size, laser energy, and heating asymmetry. As mentioned in Section 4.1.1, modelling of the linking process is considerably simplified by assuming that heat transport is contained to the Al. Arguments presented in Sections 4.2.1 and 4.2.4 validated the assumption. In Section 4.2.2 we justified the assertion that laser heating is purely a surface phenomenon in the linking process, and in Section 4.2.3 we calculated a one-dimensional melt depth of 0.95μm using an estimated reflectivity of 84% for the Ti/Al system. MARC Analysis Research Corporation's Mentat II modelling software was used in Section 4.2.4 to determine the temperature profile in the laser-pulsed aluminum in order to establish the relevant depth and lateral distance of thermally affected Al. Based on these results, we now present a simple model to determine the linking process window.

In previous work, Dr. J. Bernstein determined a laser energy window for linking. The setup involved a Nd:YAG laser from XRL Inc. with a spot diameter of 3.6 μm. The laser spot was centered on the link target and produced links between laser energies of 150 and 300 nJ for an 10-ns laser pulse. The lower bound of this energy window was determined as the energy at which occasional links could be formed. By contrast, linking was quite consistent at the upper bound of 300 nJ, but extensive passivation damage was evident. Based on this two-to-one ratio of laser energies (300nJ:150nJ) and some simple geometrical and thermal calculations, we may determine a processing window based on spot size, target offset, and laser energy for a given pulse duration.

First, we determine what fraction of laser energy actually hits and is absorbed by the Al line. (We will only be doing these calculations for the Al line since the spot size is too small to effect the tab any differently). For simplicity we assume a square, rather than Gaussian, laser pulse. Since the extinction coefficients of SiO_2 and Si_3N_4 are negligible at the laser's wavelength, we will treat the nitride and oxide over-layers as transparent to the laser. At the laser's wavelength of 1.05 μm, an evaporated film of Al has a tabulated reflectivity of about 94% (calculated as 97% in Section 4.2.2); however, since the Al line has a very thin overcoating of Ti, and its reflectivity at this wavelength is tabulated as 55% (calculated as 67%), we must determine an effective reflectivity for the Ti/Al system. As demonstrated in Section 4.2.3, an approximate one-dimensional melt depth of 0.95μm may be calculated for Al using a reflectivity of 84%. Since we know from Section 4.2.4 that the entire thickness of Ti/Al below the laser spot melts (0.95 μm), we will use an effective reflectivity of 84% for these calculations. The fraction of energy hitting and being absorbed by the Al line can now be calculated using Equation 4.7.

$$E_{Al} = E_{laser} \cdot \frac{\text{Area of Al line hit by laser}}{\text{Total area of laser spot}} \cdot 16\% \tag{4.11}$$

To convert this energy to a more generally applicable form, we need to determine what volume of aluminum is affected by the absorbed energy during the 10-ns laser pulse. We have already established that the entire area directly below the laser spot will melt. In Section 4.2.4 we noted that after 10ns, and assuming a crack-inducing temperature greater than 500°C, a lateral distance of about 0.5 μm beyond the laser spot is also affected. This allows us to calculate an approximate volume of Al affected by the laser pulse. Using the molar volume of Al (9.99×10^{-6} m^3/mole), we can determine the energy per mole of Al needed to reach the process window's range of incident laser energies.

Knowing the approximate minimum and maximum energy/mole Al needed to form a link, we can calculate the laser energy needed to achieve these energies/mole Al in both the Al line and tab for various misalignments. For example, if the laser spot is offset toward the line by 0.25 μm, we find that a laser energy window of 126 to 252 nJ and 182 to 364 nJ will be needed to reach the energy/mole Al for linking of the line and tab, respectively. The intersection of the needed line and tab energies defines an energy window in which both the line and tab are amenable to linking.

4.4 Effects of Laser Spot Size and Offset on Process Window

The method described above for determining the energy window for both an Al tab and line may be iterated for various laser spot offsets at given spot sizes. Figure 4.6 shows how the calculated laser energy window is affected by laser offsets toward the tab or line.

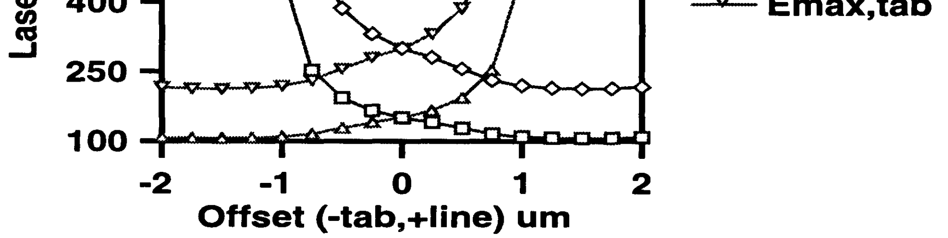

Figure 4.6: Calculated laser energy window for 3.6μm diameter spot (based on 2:1 XRL laser power window with centered spot)

The process window (where the line and tab curves overlap) is symmetric about a zero offset for this spot size. We would expect this symmetry since the laser spot diameter (3.6 µm) and the diameter of Al potentially affected by heat diffusion (4.6 µm) are smaller than the tab's length (6 µm). Thus, there is no apparent difference between the tab and line in this case. However, if the spot size were increased to the point where the tab's geometry entered into the calculations, the tab's energy window would not be symmetric to the line's energy window. This would result in a skewed process window.

Additionally, since the spot size is so small, one would assume a minimal offset would drastically affect the needed laser energies. Figure 4.6 shows this trend. If the spot size were larger, minimal offsets would be expected not to have a large effect on the energy window.

Figures 4.7 and 4.8 show theoretical process windows for spot diameters of 6 µm and 8µm, respectively. Both are based on the 2:1 values of energy/mole Al determined from the XRL linking power window calculations. The expected trends with increasing spot size mentioned above are clearly seen.

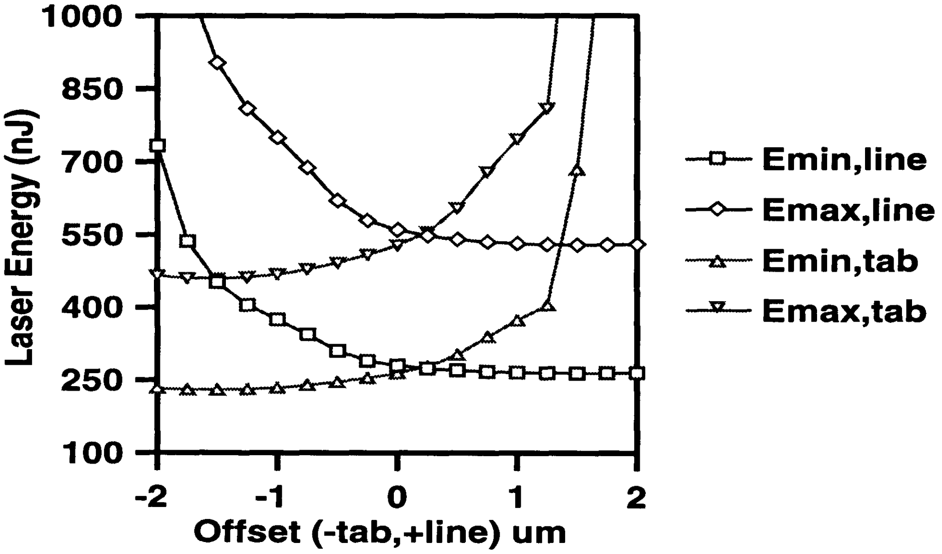

Figure 4.7: Calculated laser energy window for 6 µm diameter spot (based on 2:1 XRL laser power window with 3.6 µm centered spot).

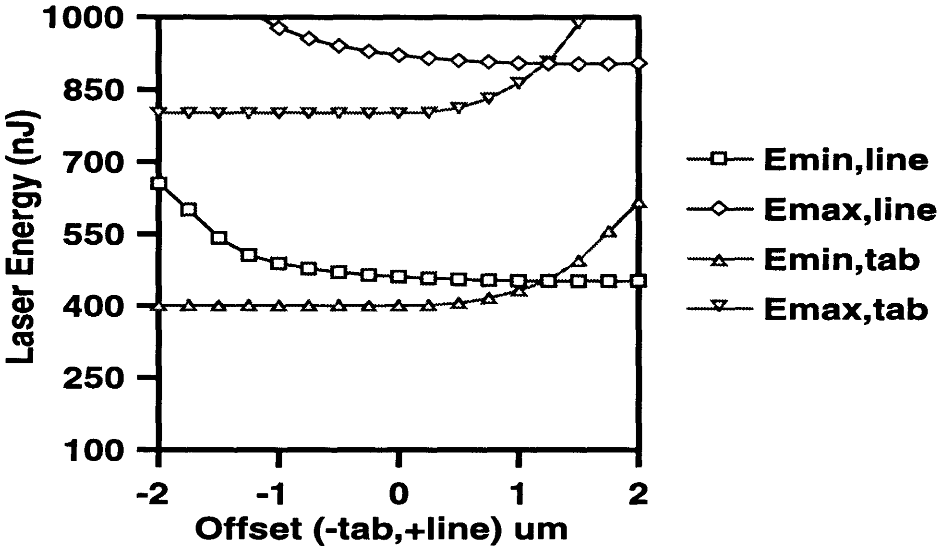

Figure 4.8: Calculated laser energy window for 8 μm spot diameter (based on 2:1 XRL laser power window with 3.6 μm centered spot).

By varying the spot size, target alignment, and laser energy, we can predict whether the Al line and tab will link. This will prove to be a valuable tool in calibrating laser systems for optimal linking. Adding more detail to the energy calculations and analyzing more experimental data will aid in refining this process window model.

4.5 Summary

The important features of these models may be summarized as follows:

1) Crack trajectory has been predicted by Y.-L. Shen based on stress concentrations in the SiO_2 and Si_3N_4 from heated Al. In a symmetrically heated system, the cracks initiate at the Al corners and propagate in an arc. Cracks from the inner corners meet and create a fissure into which the Al may flow. The outer corner cracks propagate into the nitride, thereby damaging the passivation. This may be avoided by increasing the oxide thickness.

2) Y.-L. Shen's model predicts that under asymmetrically heated conditions with only the hotter Al initiating a crack, the trajectory arcs to the other Al line due to the stress field in the oxide. As the simulated heat difference between the two Al blocks increases, the crack trajectory is less affected by the stress field and is expected to overshoot the other Al line.

3) A finite element model showed that the Ti overcoating is crucial to the linking process, thermal diffusion through SiO_2 is negligible, thermal reflection off the encasing SiO_2 quickens the melting of bordering Al, and that all the Al below the laser spot reaches its melting temperature after 10ns.

4) Assuming a surface heat source, using thermal profiles from a finite element simulation, and based on data from a previous laser linking experiment, a process window was created which predicts the approximate misalignment which will still produce a link for a given laser power.

The conclusions of this modelling will be compared with the experimental results in Chapter 6.

Chapter 5

Experiments

5.1 Heating Chips

The purpose of this experiment was to determine the effect of temperature on crack initiation in SiO_2. When the laser is pulsed, nearly all of its energy is absorbed by the aluminum which causes its heating, rapid expansion, SiO_2 cracking, Al flow into the crack, and subsequent linking -- all on the time scale of 10 nanoseconds. The question arises as to whether links could be formed by simply isothermally heating the chips. Presumably the Al would still heat up and expand thereby causing stress-induced cracks in the SiO_2. This was in fact seen by S. Prasad and U. Brahme at the site of an electrical failure following standard temperature cycling (see Figure 5.1) [29]. At higher temperatures, such cracks might then be filled with the compressed and molten Al creating links between adjacent lines.

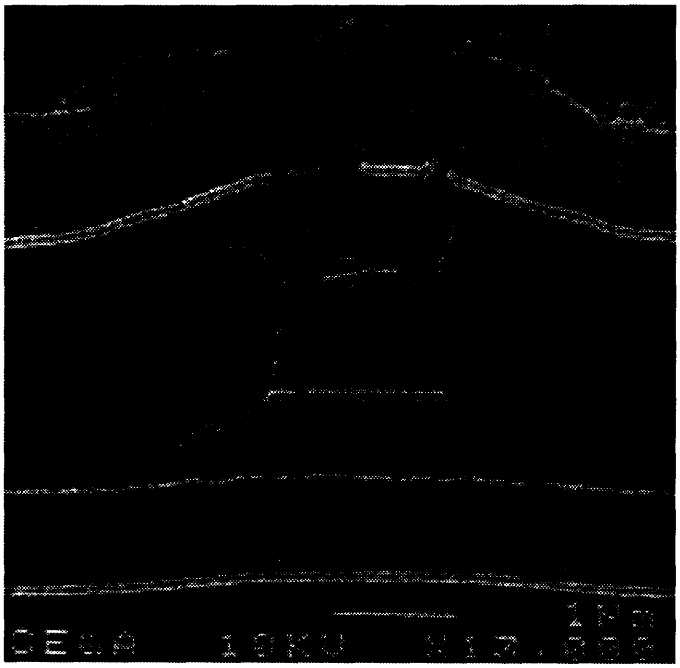

Figure 5.1: Scanning electron micrograph of defect site caused by induced cracking [29].

In this experiment, five chips were heated up to five different temperatures: 500, 600, 660, 700, and 800°C. The chips used were slightly different in architecture than those described in Section 3.1. The main difference was the lack of the lower level of metallization. Additionally, a comb-like metal line structure was fabricated at the bottom of the chip (see Figure 5.2). We expected that cross-sections through the interdigitated lines would reveal different cracking patterns for each temperature.

The comb-structure emanated from two neighboring bond pads. Three structures lay between Pads 27 and 30, while four more lay between pads 31 and 35. Since the lines were spaced 2 μm apart at the left side of the comb, but gradually increase in separation to 5 μm on the right side, we hoped to see the effects of line spacing on crack formation and trajectory.

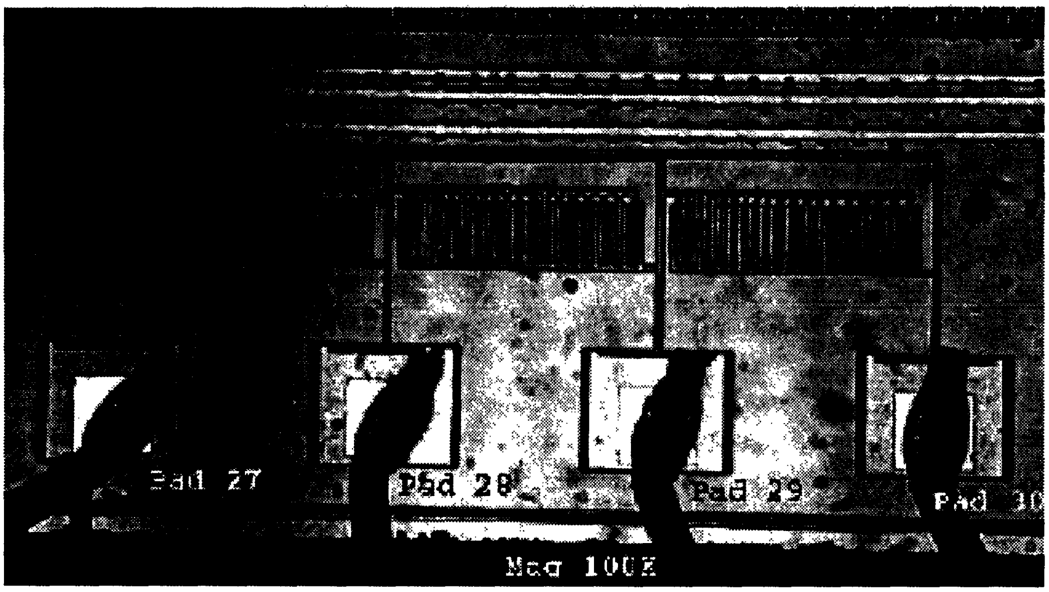

Figure 5.2: Optical picture of comb test structure.

All five chips were heated together in a furnace in air. The first chip was removed after the temperature had stabilized at 500°C for 15 minutes. The second chip was removed after the furnace temperature had stabilized at 600°C for 15 minutes. The other chips were treated similarly, in accordance with Table 5.1. A middling temperature of 660^{o}C was used since we know Metal 2 melts between 600 and 660^{o}C.

Table 5.1: Final Chip Temperatures for Heating Experiment

	Chip 1	Chip 2	Chip 3	Chip 4	Chip 5
T_{final} (C)	500	600	660	700	800

After all the chips were heated, optical pictures were taken in order to see if differences between an unheated chip and the heated ones were apparent. Most of the pictures focused on the comb structures and bond pad lines.

Following optical observations, electrical tests were done to determine if any of the comb structures linked. A probe station was used for this purpose. Each comb structure is connected to two lines emanating from neighboring bond pads, thus linking could be deduced by simply measuring the resistance between the bond pads in question.

Finally, a FIB was employed to cross-section and image areas of interest noted on the optical photographs.

5.2 Variable Power Linking

The purpose of this experiment was to gain understanding of how laser power affects linking dynamics and failure modes. A series of links was attempted using a $1/e^2$ laser spot size of approximately 6 μm in diameter over a range of pump powers, from 570 to 730mW. This window covered the entire regime of link-forming powers: 570mW is the onset of inconsistent linking and 730mW is the onset of visible passivation damage caused by linking. In this experiment, the laser pumping power began at 570mW and was increased by 20 mW every tenth link attempt. The spot was kept centered on the link target. Chips fabricated with the standard architecture, as described in Section 3.1, were used in both this experiment and those in the next section. A FIB was used to cross-section and image selected successful and failed links to categorize modes of failure and damage.

5.3 Off-center Linking

The purpose of this experiment was to determine what effect an off-centered laser spot has on linking and to compare the results with Y. Shen's model summarized in Section 4.1. In a procedure similar to that of the variable power experiment, a $1/e^2$ spot size of 6 μm and pump power of 650 mW were used to attempt a series of links. Linking trials began with the laser spot centered over the link target. After every tenth attempt, the center of the beam was displaced "up" by 0.25 μm toward the via-tab (see Figure 5.3). Then ten more links were attempted. This process was repeated until the last ten attempts were made with the laser displaced by 2 μm from the center of the link target.

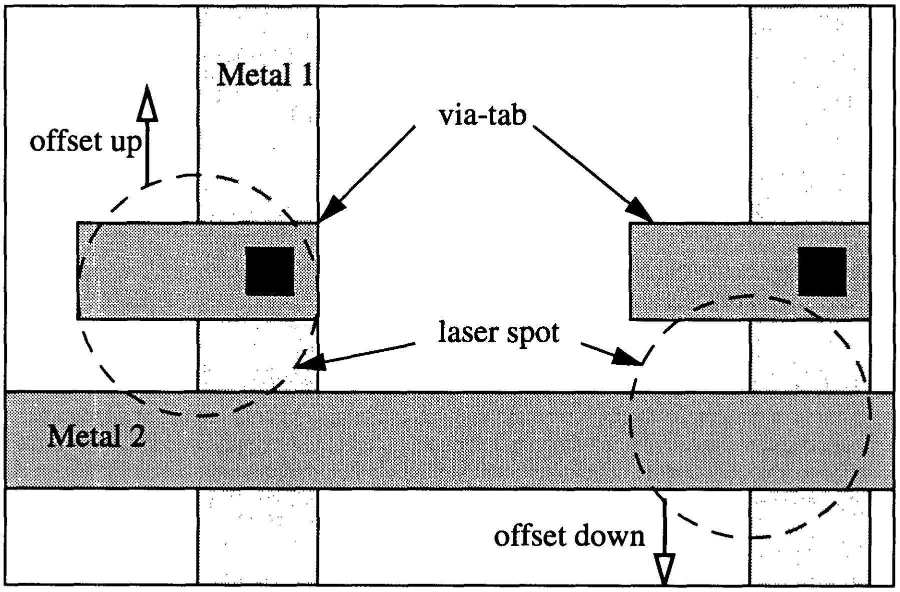

Figure 5.3: Schematic of chip with laser offset directions indicated (not to scale)

Another series of experiments was run in the same manner, but with displacement "down" by 0.25 μm away from the via-tab (see Figure 5.3). After all the linking was completed for both experiments, a FIB was again used to cross-section selected successful and failed links.

Chapter 6

Results and Discussion

6.1 Heating Chips

6.1.1 Optical Results

The results of optical observations are summarized in Table 6.1 and representative pictures may be found in Figures 6.1-6.5. These observations lead to the following general statements:

1) Visible changes begin at 600°C.
2) Visible damage is concentrated around the bond pads and the Al line emanating from them.
3) There is no visible damage in the bulk portion of the chips where laser linking would normally occur.
4) Small white patches are seen at the ends of some Al lines that run through the bulk of the chip (for temperatures of 600°C and greater).
5) As the temperature increases, the extent of damage increases; however, it still is concentrated around the bond pads and lines emanating from them.

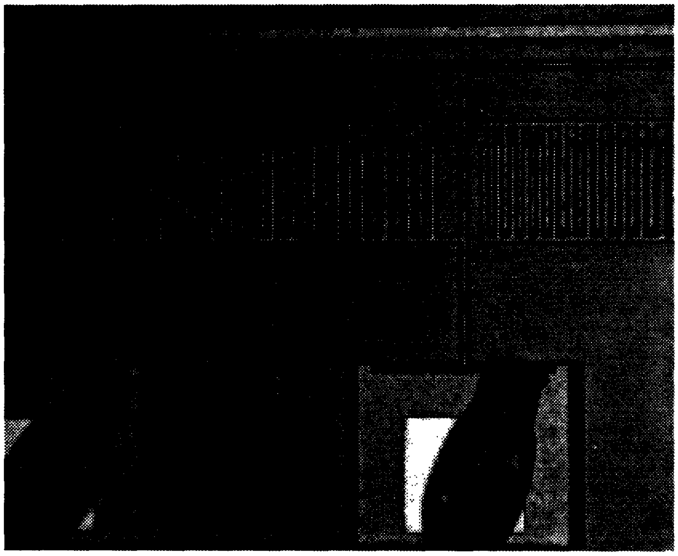

Figure 6.1: Optical picture of Chip 1. No visible change.

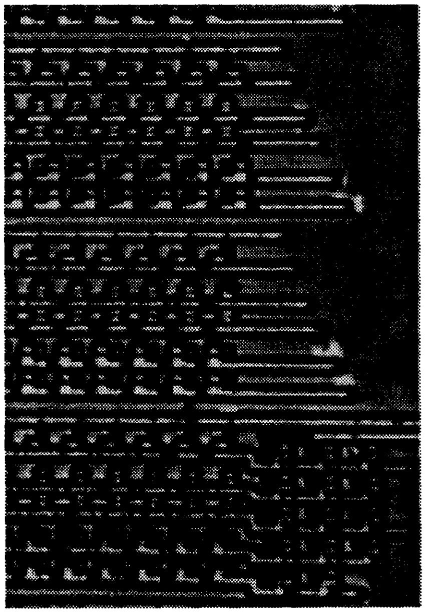

Figure 6.2: Optical picture of Chip 2. White patches visible at ends of lines.

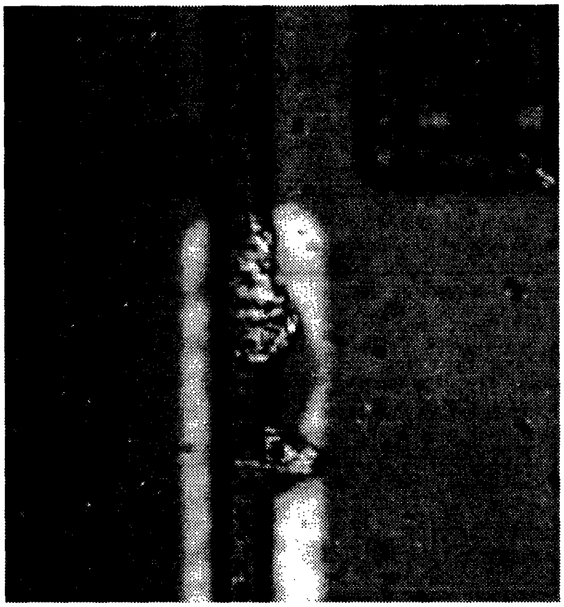

Figure 6.3: Optical picture of Chip 3. White discoloration surrounding Al line. Contamination.

Figure 6.4: Optical picture of Chip 4. Light and dark patches surrounding lines/comb.

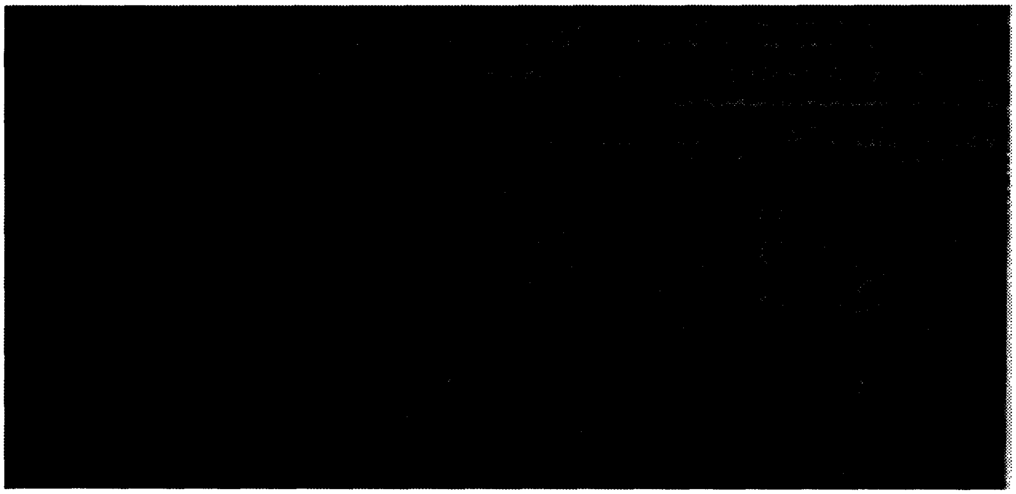

Figure 6.5: Optical picture of Chip 5. Extensive damage and discoloration.

Table 6.1: Optical Observations of Heated Chips

Chip/T_{final} (C)	Optical Observations
Chip 1/ 500	Nothing.
Chip 2/ 600	Light patches at ends of some lines.
Chip 3/ 660	As above and light areas around some Al lines.
Chip 4/ 700	Light and dark areas around lines and bond pads.
Chip 5/ 800	Visible cracking on surface. Extensive discoloration all around bond pads, lines, and into comb structures.

6.1.2 Electrical Results

A probe station was employed to determine if any links had formed in the comb structures. The results are presented in Table 6.2. Since typical laser links have a resistance of 10 to 90 Ohms, it appears that some type of connection did form at the higher temperatures (chip4/700°C, chip5/800°C). Additionally, some form of high-resistance connection is evident in chips 2-5.

Table 6.2: Electrical Results of Heated Chips Measured on a Probe Station

Chip/T_{final} (°C)	Between Pads	Ohms	Link?
Chip 0/ 25	all pairs	$0.4\text{-}2 \times 10^6$	no
Chip 1/ 500	all pairs	$0.6\text{-}3 \times 10^6$	no
Chip 2/ 600	all pairs	3,000-infinity	some?
Chip 3/ 660	all pairs	800-10,000	some?
Chip 4/ 700	all pairs but	1,000-9,000	some?
	29 & 30	80	yes?
Chip 5/ 800	all pairs but	100-5,000	some?
	34 & 35	20	yes?

6.1.3 Cross-section Results

Focused ion beam pictures of some of the more interesting cross-sections are displayed below in Figures 6.6-6.11. Generally, we see that at lower temperatures, nothing seems unusual. However, beginning at 660°C, the Al line and surrounding SiO_2 seem to change chemically; the white Al line turned grey and the grey SiO_2 region became white near the Al line. With higher temperatures, the white area in the SiO_2 spread farther out from the Al line. Additionally, we note that etch pits formed in the Si below the Al lines, possibly related to the SiO_2 breakdown. Though interesting, none of these temperature effects are relevant to the linking procedure.

Figure 6.6: Chip 1, Typical cross-section, Revealed nothing of note.

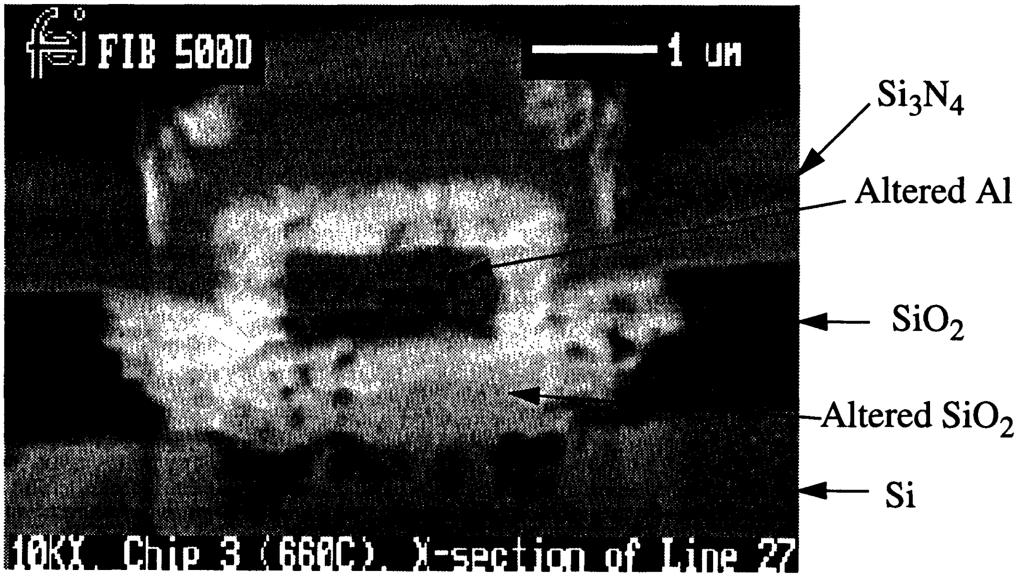

Figure 6.7: Chip 3, Chemically changed SiO_2 and Al noticeable.

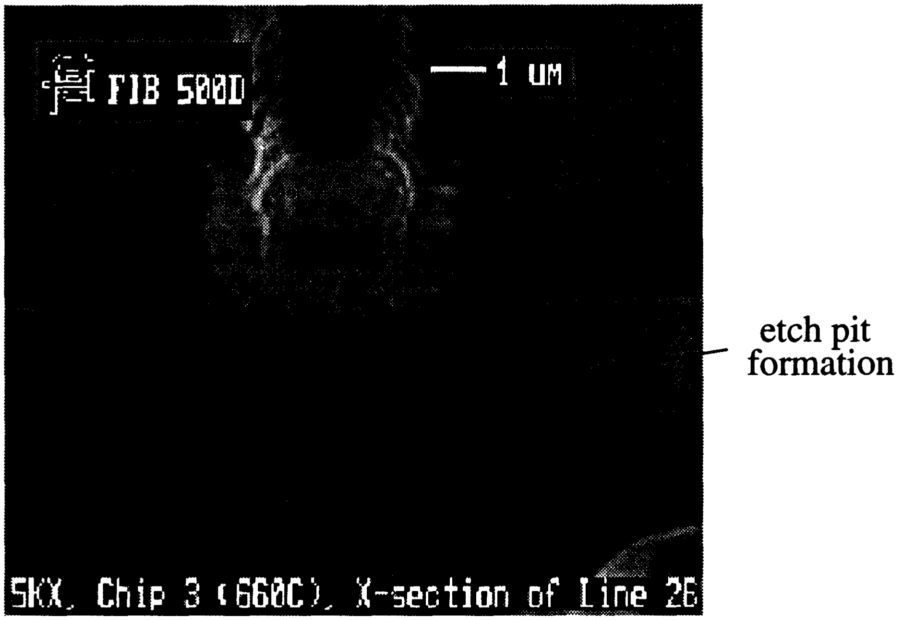

Figure 6.8: Chip 3, Chemically changed SiO_2/Al and formation of Si etch pit noticeable

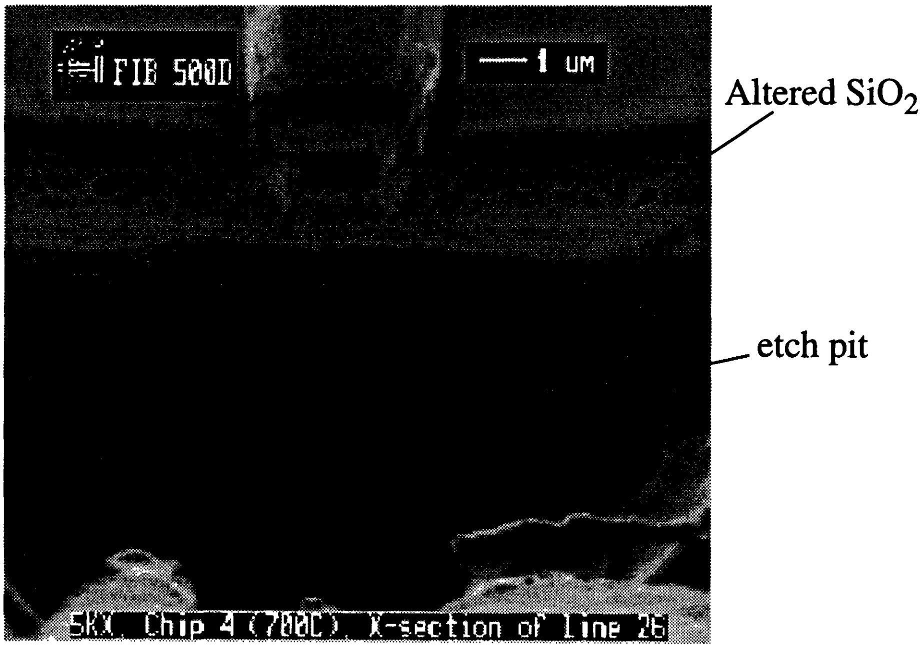

Figure 6.9: Chip 4, Etch pit in Si, Chemically changed SiO_2 region spreads laterally.

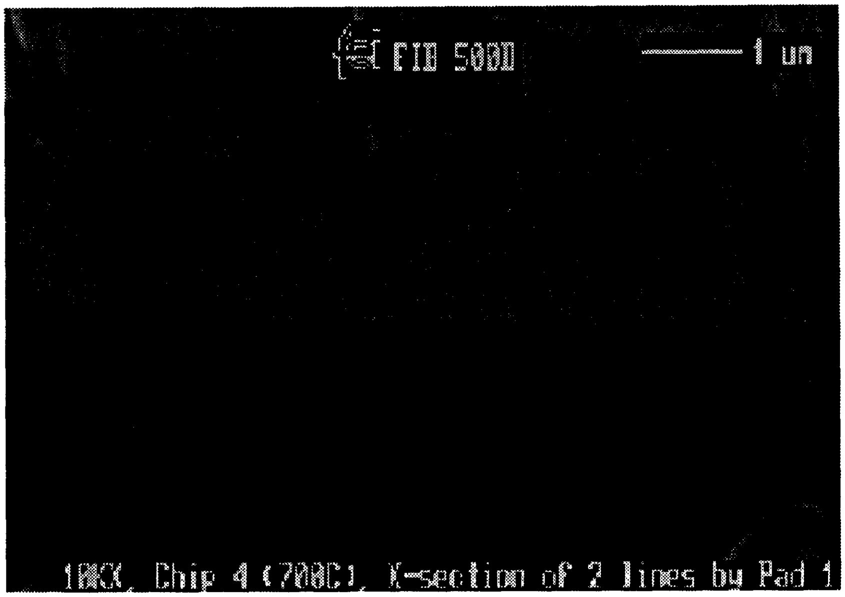

Figure 6.10: Chip 4, Mini-etch pits in Si, Altered SiO_2/Al

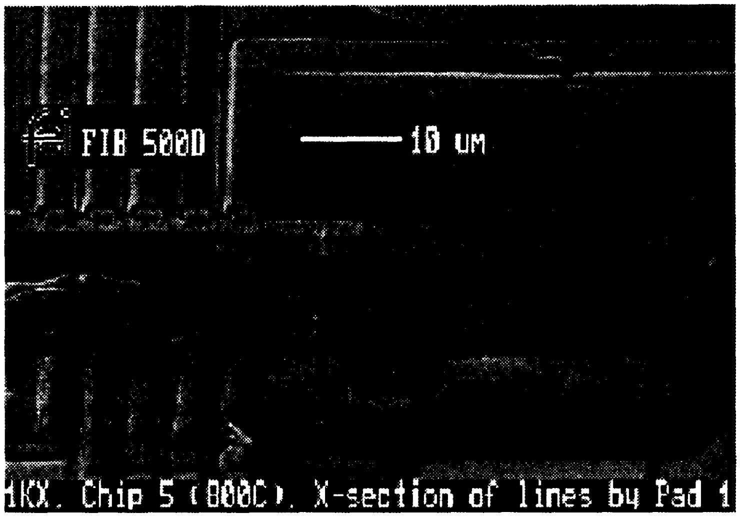

Figure 6.11: Chip 5, Large etch pit below surface crack, Extensive SiO_2/Al spreading.

The chemically changed Al line and whitened SiO_2 areas were characterized using energy dispersive X-rays (EDX). It was determined that at temperatures above 660°C, the grey rectangular area representing the Al line was in fact comprised of mostly Si, a little

Al, and very small amounts of Ti and W (see Figure 6.12). Similarly, the whitened SiO_2 areas were found to be mainly Al with a little Si (see Figure 6.13). In effect, the Si and Al seem to have switched places. It is presumed that oxide forms of Al and Si are present, but that is undetectable by EDX. The Ga revealed in both plots is attributed to the Ga^+ ion beam used for cross-sectioning. Once again, though interesting and puzzling, these findings have no direct relevance to the linking phenomenon and therefore were not pursued.

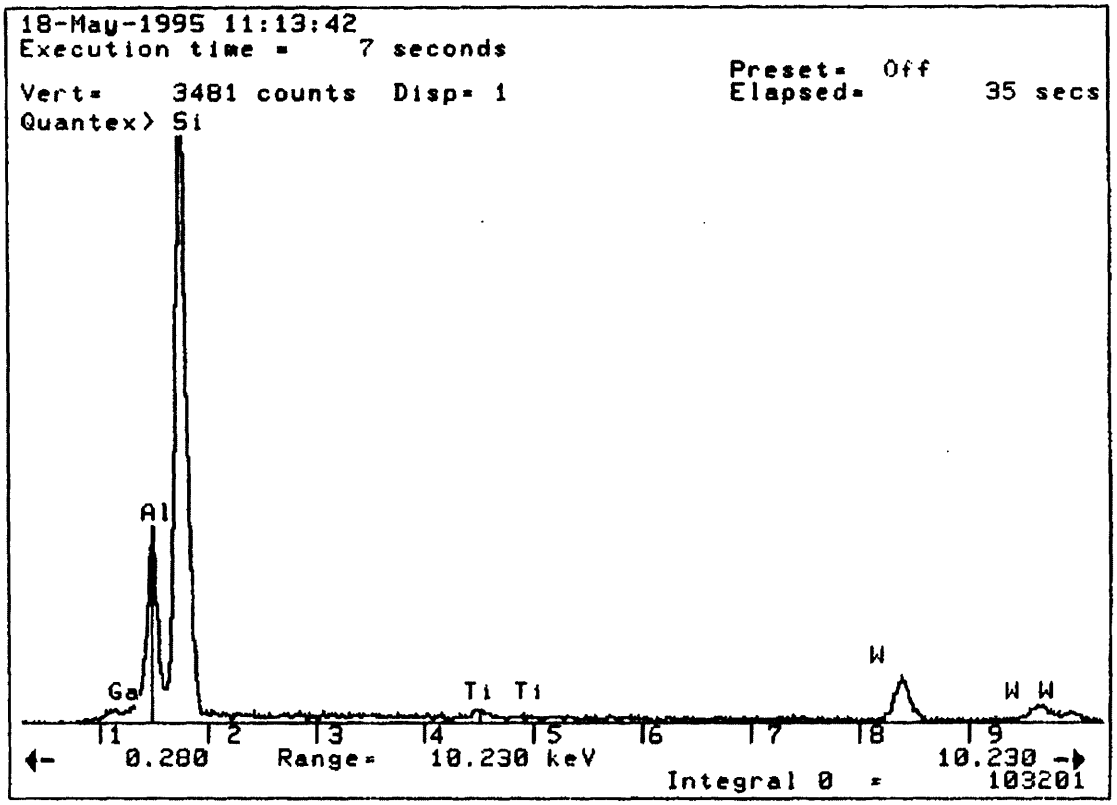

Figure 6.12: EDX analysis of what was originally an Al line with Ti and TiW coatings.

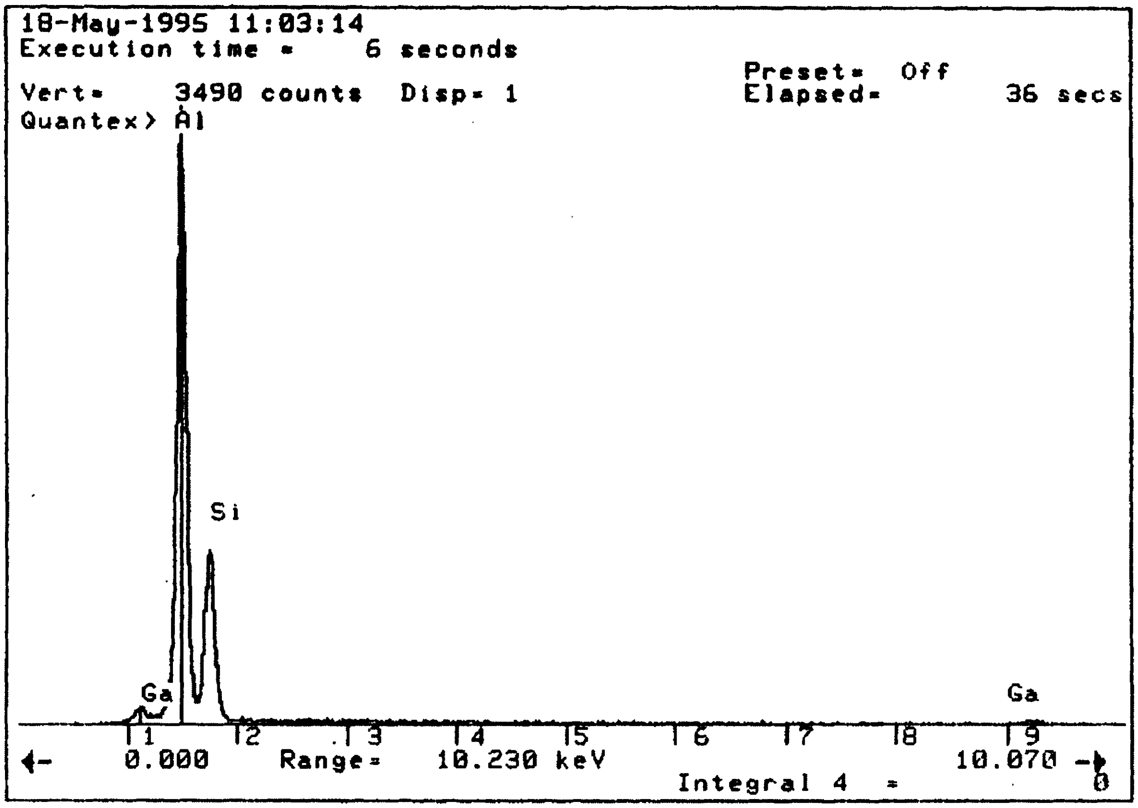

```
18-May-1995 11:03:14
Execution time =     6 seconds
                                          Preset=  Off
Vert=     3490 counts  Disp= 1            Elapsed=        36 secs
Quantex> Al
```

Figure 6.13: EDX analysis of what was originally SiO_2.

6.1.4 Discussion

High temperature isothermal heating does not result in high quality linking, and no oxide cracks were observed. The discolored regions noted in optical pictures were in fact Si etch pits and chemically altered SiO_2 rather than Al-filled oxide cracks. High temperature isothermal heating draws Si into the Al line and Al into the neighboring SiO_2 regions. The etch pits in the Si substrate were typically located directly below Al lines or surface cracks. This experiment proves that rapid and highly localized heating of the Al, and not constant, uniform heating of the entire structure, is crucial to the linking process.

6.2 Linking Yield for Power Variation and Spot Offset

Results from the linking trials described in Section 5.2 and 5.3 are presented in Figures 6.14 and 6.15 as the number of successful links out of ten attempts. Both variable power and spot offset ranges covered their entire respective process window. We note the onset of linking at the lowest power setting and visible passivation damage at the higher settings. With offsets, we see that yield diminishes as offset increases. Since poor stage alignment was noted during these latter trials, the actual offsets should be considered more of a guideline than quantitative rule.

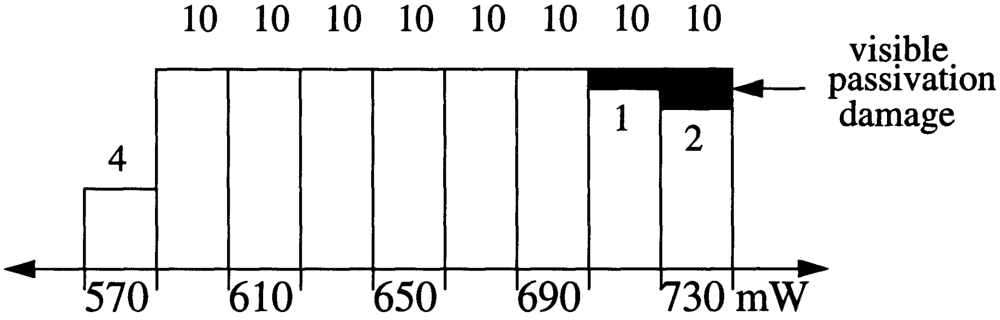

Figure 6.14: Number of successful links (out of 10) for each laser pump power. Dark areas represent links with visibly damaged passivation.

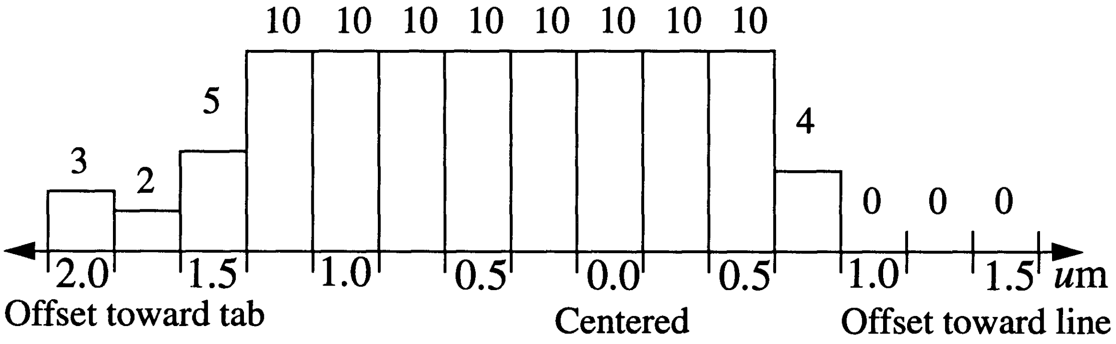

Figure 6.15: Number of successful links (out of 10) for each laser spot offset.

6.3 Variable Power Linking

6.3.1 Cross-sectional Results

The results of a 6 μm centered laser spot varied in power from the minimum needed to form links to the maximum forming links but causing visible passivation damage can be classified into four different categories (see Table 6.3).

Table 6.3: Results of Variable Power Linking

Case	Link?	Figure	Characteristics of Cross-section	Pump Power
1	Yes	6.16	Short cracks from outer-corners.	570-690mW
2	Yes	6.17	Either line or tab's outer-corner crack compromises passivation.	690-730mW
3	Yes	6.18,19	Both line and tab outer-corner cracks compromise passivation, large Al voids, passivation may be displaced upwards.	690-730mW
4	Yes	6.20,21	Passivation above line and tab ejected, extensive voiding forms Al troughs.	710-730mW

The line is on the left and the tab is on the right in all cross-sectional pictures of link targets presented in this work. Additionally, all FIB pictures of the cross-sectional faces were taken with the chip at a 50-70^{0} angle to the ion beam. As was expected, the cracks initiated from the upper corners of the Al. When molten Al filled the cracks, the resultant voids were sometimes visible in the line and/or tab.

Case (1) demonstrates the ideal linking condition of a link between the line and tab with minimal cracking from the outer-corners. In Case (2), the inner-corners again formed a link, but one of the outer-corner cracks propagated through the nitride to the surface. When both the outer-corner cracks compromise the passivation, Case (3) is created. Large voids in the center of the Al line and tab and occasional passivation displacement also characterize Case (3). Case (4) demonstrates the ejection of the entire passivation area over a linked target. The ejection reveals Al troughs in place of the line and tab.

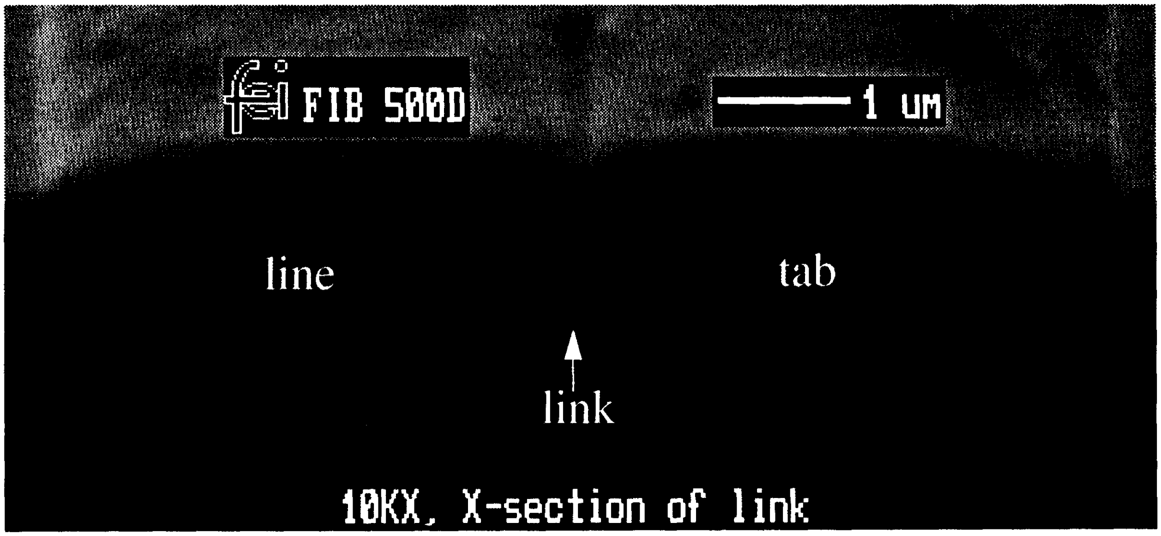

Figure 6.16: Case (1) for variable power: Linking, short cracks from outer-corners.

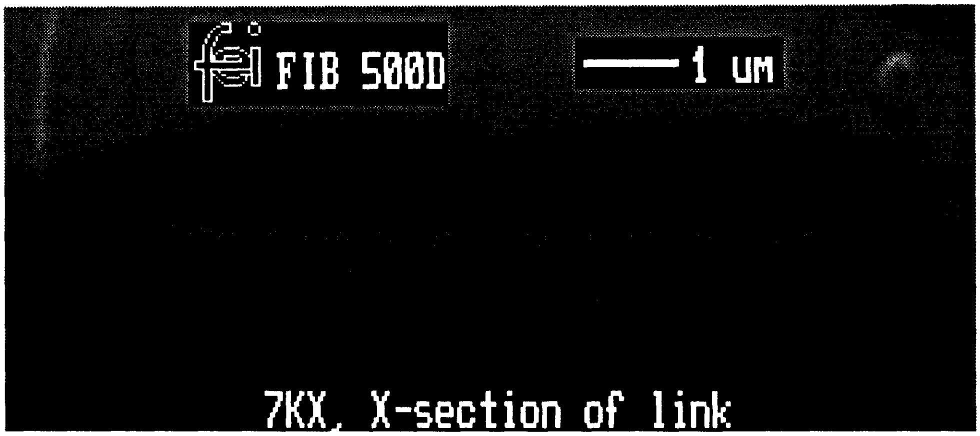

Figure 6.17: Case (2) for variable power: Linking, line's outer-corner crack compromises passivation.

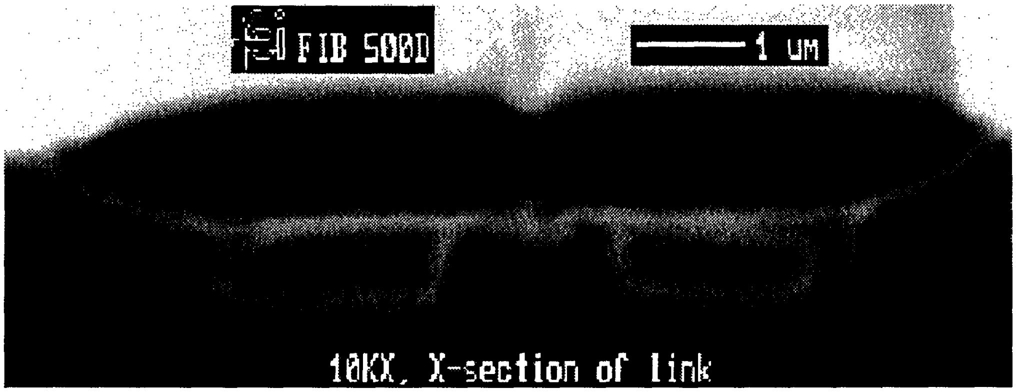

Figure 6.18: Case (3) for variable power: Linking, outer-corner cracks compromise passivation, large voids in Al from filling cracks.

Figure 6.19: Case (3) for variable power: Linking, outer-corner cracks displace passivation upwards, large Al voids from filling cracks.

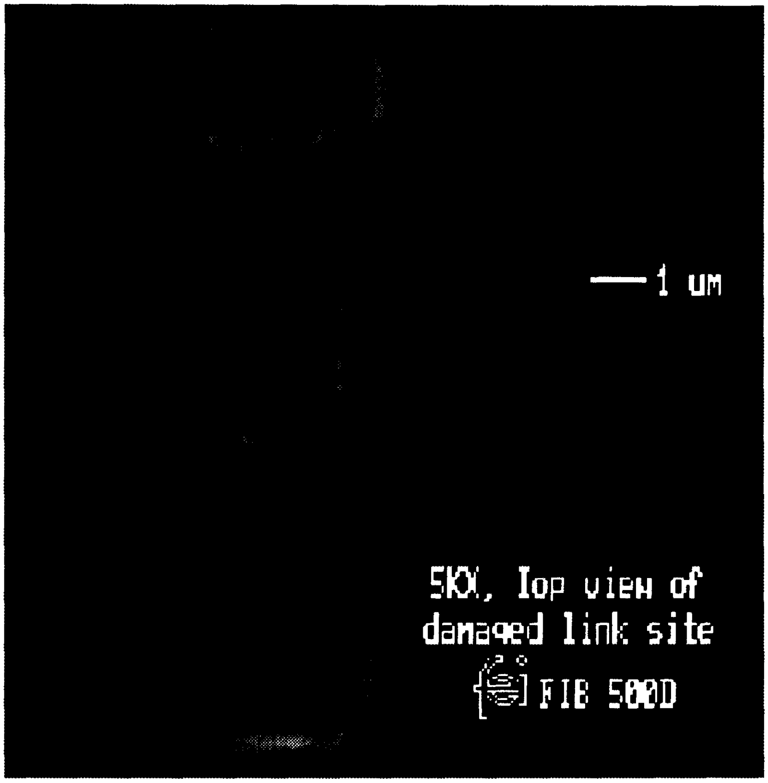

Figure 6.20: Case (4) for variable power: Linking, passivation ejected (top view).

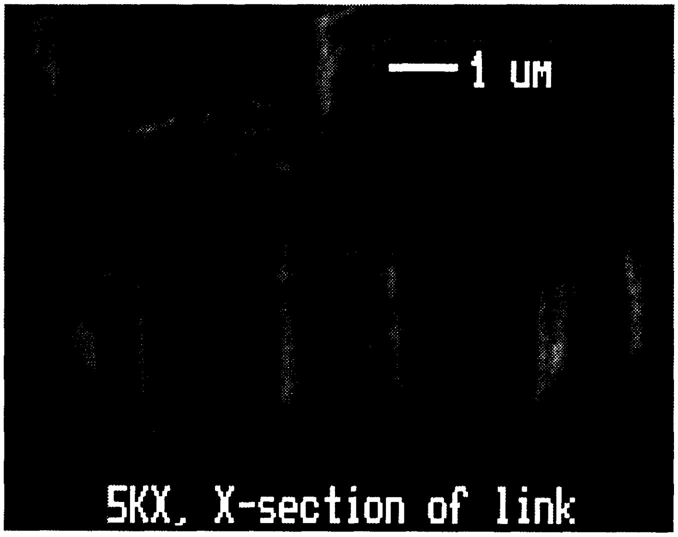

Figure 6.21: Case (4) for variable power: Linking, passivation ejected, tab and line resemble troughs (Cross-section of Figure 6.20).

Case (1) was seen for pump powers of 570 to 690 mW. The pump power range for Cases (2) and (3) were both 690 to 730 mW. Since the maximum laser pump power for this experiment was set at the onset of visual passivation damage, only pump powers of 710 to 730 mW produced some passivation ejection and trough formation as in Case (4).

6.3.2 Discussion

As might be expected, a centered laser spot at low to mid linking pump powers creates links with no passivation damage. This is because the Al stresses required for linking are less than those needed to propagate a crack all the way to the surface. At the low to middle range powers, there is enough thermally-induced Al expansion to promote link cracks and very short outer-corner cracks. However, as the higher linking powers are reached, passivation damage begins, quickly increasing in severity. As will be seen, the damage parallels that of Cases (2), (3), and (4) for the tab offsets. We may conclude that after a threshold in power per volume of Al has been reached, the amount of energy absorbed by the Al line and tab in 8 to 10ns is large enough to propagate cracks through the oxide and nitride to the free surface.

To create consistently undamaged links, the power window range for a centered laser spot should be established. One of the middle power settings should then be used for all further processing with the same spot size. This avoids passivation damage while still consistently forming links.

6.4 Off-center Linking

6.4.1 Cross-sectional Results

There are four primary classifications for link attempts with the 6 μm laser spot offset toward the tab by 0.0 to 2.0 μm (see Table 6.4).

Table 6.4: Results of Laser Offset Toward Tab

Case	Link?	Figure	Characteristics of Cross-section	Offset to tab
1	Yes	6.22	Tab's outer-corner crack compromises passivation.	0.0-1.5 μm
2	No	6.23	Tab's inner and outer-corner cracks compromise passivation.	1.5-2.0 μm
3	No	6.24,25	As in Case(2), but passivation displaced upward.	1.5-2.0 μm
4	No	6.26,27	Passivation above tab ejected.	1.75-2.0 μm

In Case (1) the inner-corner crack arcs toward the Al line and, though slightly displaced upward midway across the link path by the close proximity of the dip in the free surface above it, completes the expected link trajectory. The outer-corner crack follows a straight trajectory through the nitride and up to the surface where the passivation curves down and flattens out. Case (2) shows the inner-corner being fully deflected midway across the link path up to the dip in the free surface. The outer-corner crack propagates as before. Case (3) is a more extreme version of Case (2) where the nitride passivation above the cracks is displaced upwards. In Case (4) the passivation over the tab is actually blown completely off, demonstrating the effect of precipitous heating and violent cracking.

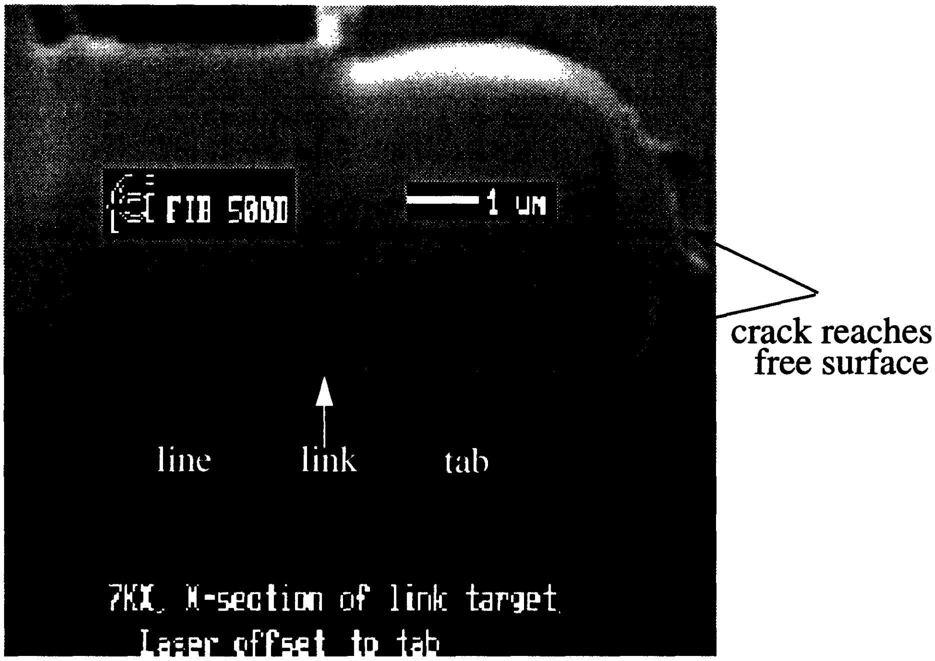

Figure 6.22: Case (1) for tab offset: Inner-corner links, outer-corner crack compromises passivation

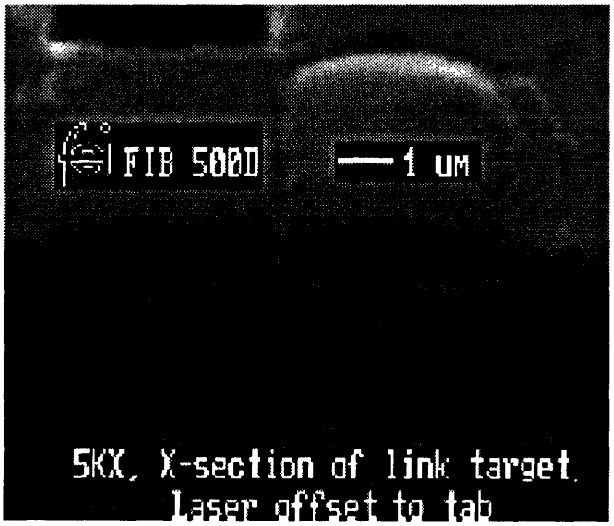

Figure 6.23: Case (2) for tab offset: Inner- and outer-corner cracks compromise passivation.

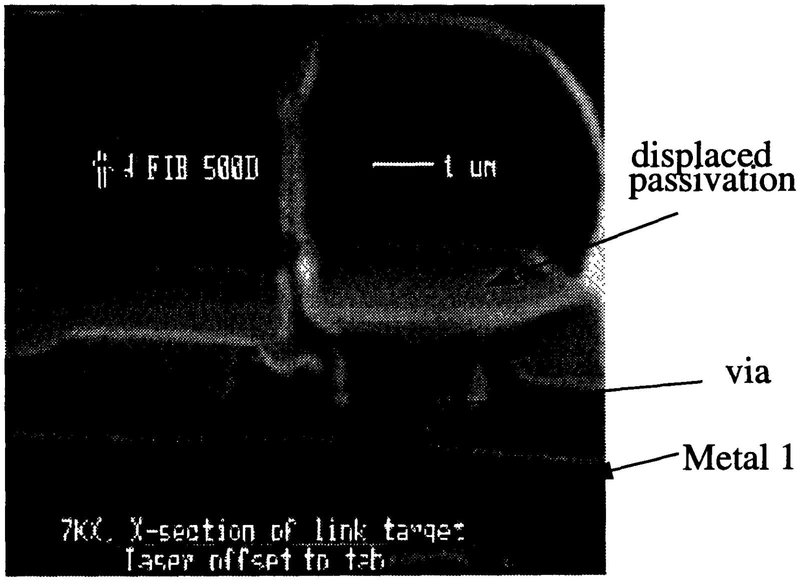

Figure 6.24: Case (3) for tab offset: Passivation compromised and displaced upward.

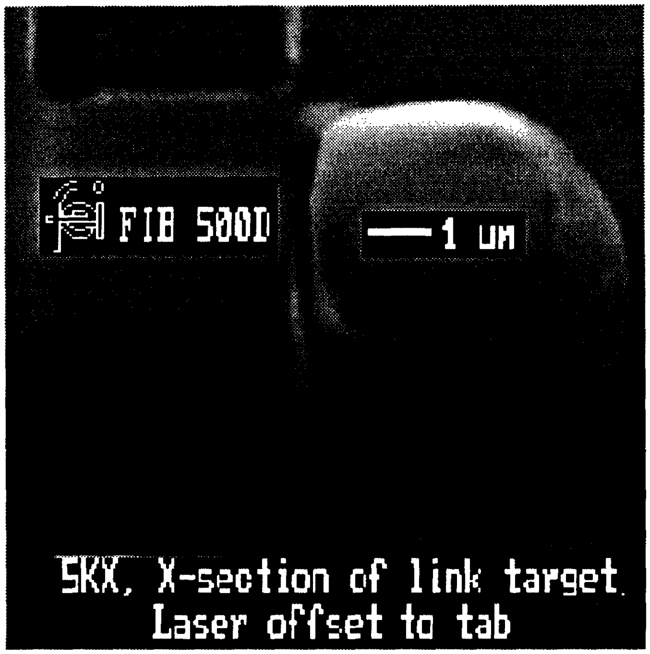

Figure 6.25: Case (3) for tab offset: Passivation compromised and displaced upward.

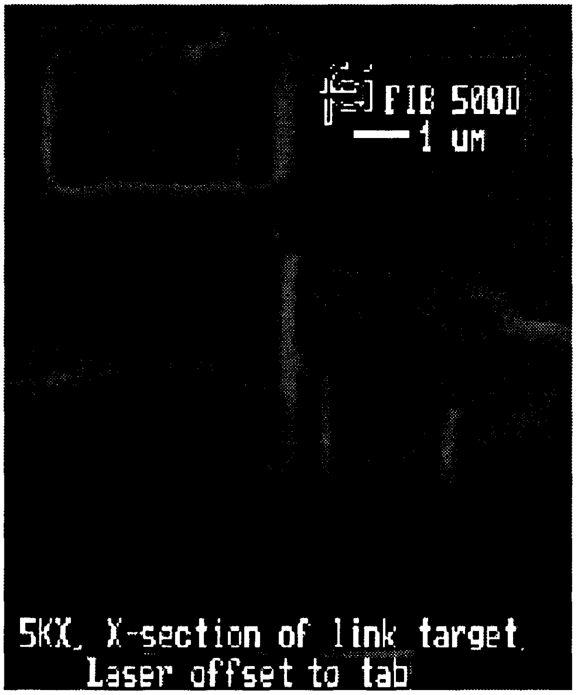

Figure 6.26: Case (4) for tab offset: Passivation ejected.

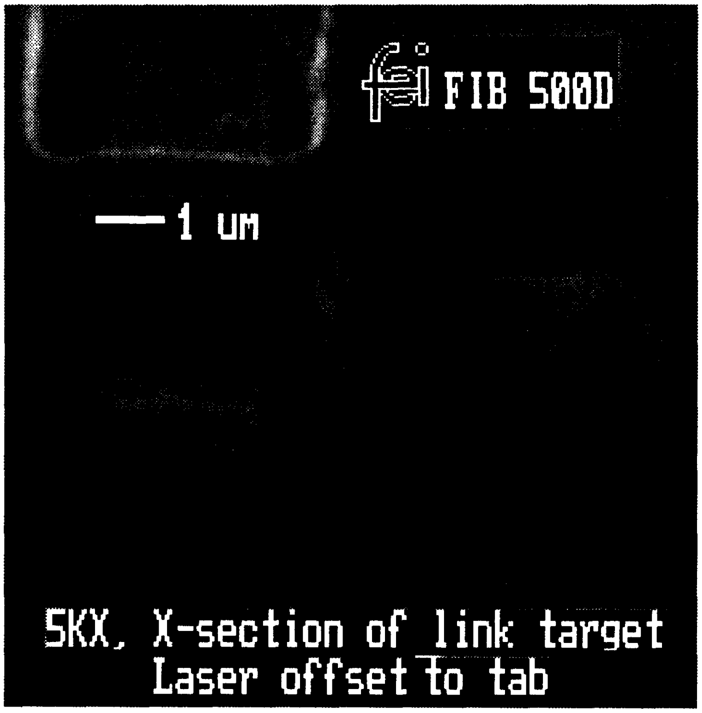

Figure 6.27: Case (4) for tab offset: Passivation ejected.

Case (1) was observed for offsets ranging from 0.0 to 1.5 μm, though the occurrence decreased rapidly after 1.25 μm. Cases (2) and (3) were noted in offsets ranging from 1.5 to 2 μm, while Case (4) was only seen in offsets of 1.75 to 2 μm.

Laser offsets of 0.0 to 1.5 μm toward the line resulted in one of two possible outcomes (see Table 6.5).

Table 6.5: Results of Laser Offset Toward Line

Case	Link?	Figure	Characteristics of Cross-section	Offset to Line
1	Yes	6.28	Line's outer-corner crack compromises passivation.	0.0-1.0 μm
2	No	6.29	Line's inner-corner crack terminates before forming link, outer-corner crack compromises passivation.	0.75-1.5 μm

Case (1) is exactly the same as Case (1) for tab offsets, but the cracks emanate from the line rather than the tab. Case (2) is similar to Case (2) for tab offsets except that the inner-corner crack terminates about half way across the link trajectory rather than making it through the passivation to the dip in the free surface.

Figure 6.28: Case (1) for line offset: Inner-corner links, outer-corner compromises passivation.

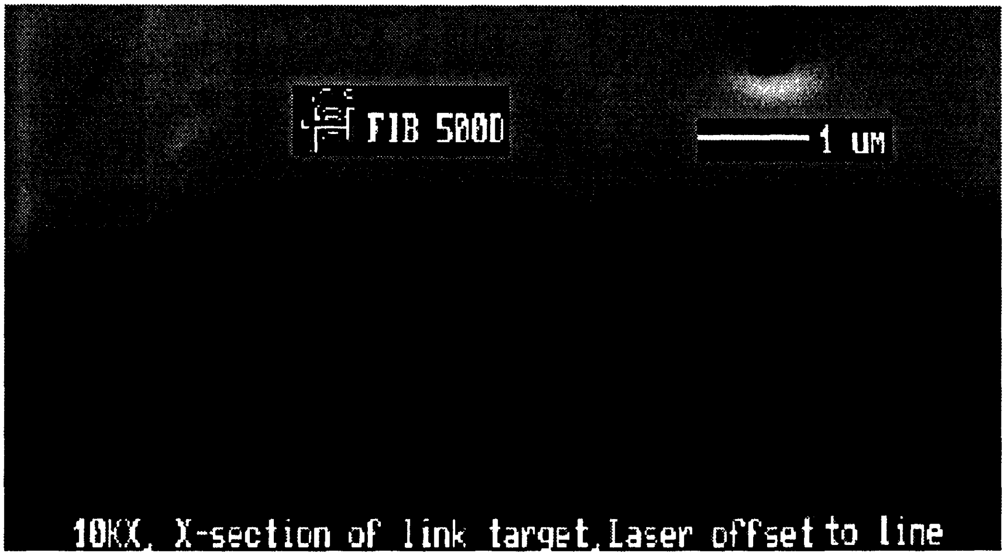

Figure 6.29: Case (2) for line offset: Inner-corner crack terminates halfway to free surface, outer-corner compromises passivation.

Case (1) was observed for offsets of less than 1.0 μm. Case (2) was demonstrated between offsets of 0.75 and 1.5μm. No passivation displacement or ejection was seen with laser offsets toward the line of 0.0 to 1.5 μm.

6.4.2 Discussion

As predicted by Y.-L. Shen's model, cracking initiates from the upper corners of the Al line or tab. The 60-40% and 75-25% asymmetric heating simulations also loosely parallels the experimental crack trajectories for small offsets. In both the model and reality, Al-filled cracks were seen to make a low arc from the line to tab (or vice-versa).

Some important differences must also be noted. Experimental cracks were seen to propagate through the nitride passivation layer and reach the chip's surface, while the model predicts the cracks will stay within the nitride and propagate laterally. The reason for this lies in the differences between the model's idealized rectangular geometry and the actual chip geometry which includes curved surfaces. Furthermore, the model uses an increased oxide thickness and assumes symmetric boundary conditions on both sides. In reality, the crack is influenced by the close proximity of (1) the dipping free surface between the line and tab and (2) the sloping one on both sides of the link target. This was not included in Shen's model. However, by increasing the oxide layer as Shen suggested, the distance between the cracks and the free surface would be increased and should thereby reduce the frequency of passivation damage.

Since the tab is a contained volume of Al, it would be expected that as the laser is displaced toward it, it absorbs more energy per volume than the line. This results in higher Al temperatures during the 8 to 10-ns process time. The higher temperature produces higher stresses in the SiO_2 which causes more violent cracking and results in a range of passivation damage from cracking or displacement to ejection.

We note that as the laser is offset more towards the line, linking is thwarted and the Al-filled crack hooks upward before terminating in the passivation layer. Unlike the tab, no passivation displacement or ejection occurred for offsets toward the line. There are two reasons for this. First, the Al line is not a contained volume and therefore some heat may be dissipated away from the link site by the line. The heat dissipation lowers the amount of heat per volume in the link-area of the line; and thus, it also lowers the stress induced in the oxide by the Al thermal expansion. Secondly, only offsets up to 1.5μm were tested. Greater offsets might provide the extra fraction of energy needed to promote the inner-corner crack to the free surface. The process window plots in Section 4.4 also support the trend that larger offsets can be tolerated toward the line than the tab before passivation damage occurs.

6.5 Summary

The key experimental results may be summarized as follows:

1) Isothermal heating provided no evidence of oxide cracking or of expected linking cross-sections; rather, rapid and highly localized heating of the target Al is required.
2) Oxide cracks initiate at the upper corners of the Al.
3) A middle-range pump power and centered laser spot will consistently produce perfect links with no passivation damage.
4) Laser offsets towards the tab or line increases passivation damage. Forms of damage range from crack propagation through the passivation to complete passivation ejection.
5) As the laser pump power increases to the upper edge of the power window, passivation damage increases in the same manner as in (4) above.

As modelled by Y.-L. Shen, cracking does initiate from the upper corners of Al (see Section 4.1). It is important to note that only the Al was heated in the simulation. From that and the results of the chip heating experiment, it can be concluded that localized heating of the Al and not the SiO_2 or Si_3N_4 is a necessary condition for linking.

Linking attempts using various laser pump powers suggest that a mid-window setting be used. This provided the most consistent linking without any form of passivation damage. At higher powers, passivation damage similar to that seen in the tab offset experiments was evident. At the lower end of the window, linking is inconsistent. Considering the process window models in Section 4.4 we note that at a mid-window power setting, the allowable offset range that still produces links is maximized. Since it is easier to control laser power than laser positioning, this is another reason for using mid-window laser power settings.

The offset experiments verified the general trends of Y.-L. Shen's asymmetric heating model, but also revealed the model's limitation of using idealized rectangular geometries and symmetric boundaries. Shen's model predicted that asymmetrically heated chips will eventually cause cracks to propagate laterally through the nitride passivation. In reality, the passivation conforms to the topology of the chip by curving over the Al line and tab instead of maintaining a uniform distance of 1.2μm above the Al. Crack trajectories therefore have a greater propensity to arc up to the surface rather than propagating laterally in the nitride. In extreme cases, the cracks reaching the free surface may displace or even eject the passivation. It was also noted that severe passivation damage occurs more frequently when the laser is offset toward the tab than toward the line. This is attributed to the finite volume of the Al tab as compared to the long Al line. For a given amount of energy, the line has a larger volume of material available for heat dissipation than the confined tab. Thus, if the tab is small compared to the laser spot size, the same amount of energy absorbed by the tab and line may cause a much greater temperature rise in the tab. Higher temperatures induce more thermal expansion which results in higher stresses in the SiO_2 at the corners of the Al tab. Hence, it is clear that passivation damage should occur more readily for the tab than line. This is shown by the general trends of the process window in Section 4.4.

Rationale for increasing the thickness of the oxide layer between the Al and nitride was given by Y.-L. Shen. From the experimental results presented above, it seems clear that a thicker oxide would reduce the propensity for crack penetration through the passivation layer. In effect, this could allow for a more robust process since the passivation damage caused by slight offsets or power variations would be negated.

Chapter 7

Conclusions and Future Work

7.1 Conclusions

The dynamics of laser linking were explored in this paper. Experiments included isothermal chip heating, laser linking over a range of pump powers, and laser linking with various beam offsets. Cross-sections were successfully created with a focused ion beam to reveal the link targets for each experiment. The imaged cross-sectional faces were used to categorize modes of failure and damage for each experiment. Models of crack initiation and propagation created by Y.-L. Shen were summarized and compared to the experimental results. Various sections of Shen's model were verified, and some contradicted, by the FIB cross-sections. Suggestions to improve the model and the linking architecture were made. Finite element simulations were created to explore laser absorption and subsequent thermal diffusion in Metal 2. A simple rationale for a process window was proposed based on these simulations, calculations, and some simplifying assumptions. The model can be used to predict qualitatively the effects of laser power and offset. With all of this in mind, we conclude that laser linking is a promising technology full of research possibilities.

7.2 Future Work

In order to characterize thoroughly the linking process and make it of commercial utility, more research must be conducted. Lifetime tests including electromigration effects and thermal cycling must be done to determine link robustness. Additionally, line widths and line spacings of the linking structures must be reduced to make the process compatible with today's semiconductor technology. More sophisticated models and creation of a quantitative process window should also be pursued. After these issues are dealt with, laser linking will prove a valuable tool in microelectronics processing and repair.

Appendix A

Finite Element Modelling Results

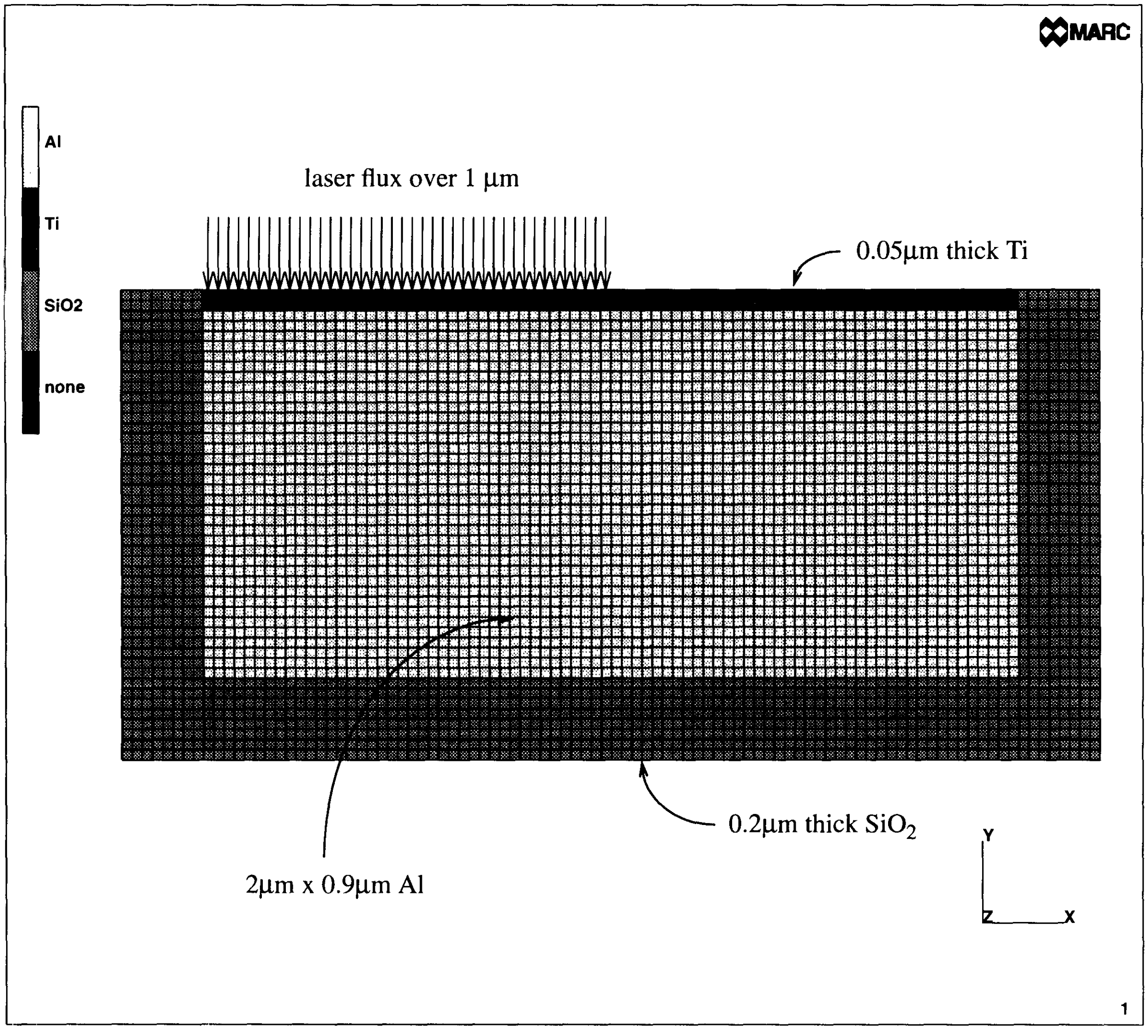

Figure A.1: Materials, geometry, edge flux, and finite element mesh for all simulations. Metal 2 (2 µm by 0.95 µm) is cupped by SiO_2 (0.2 µm thick). Each square element has an edge length of 0.025 µm.

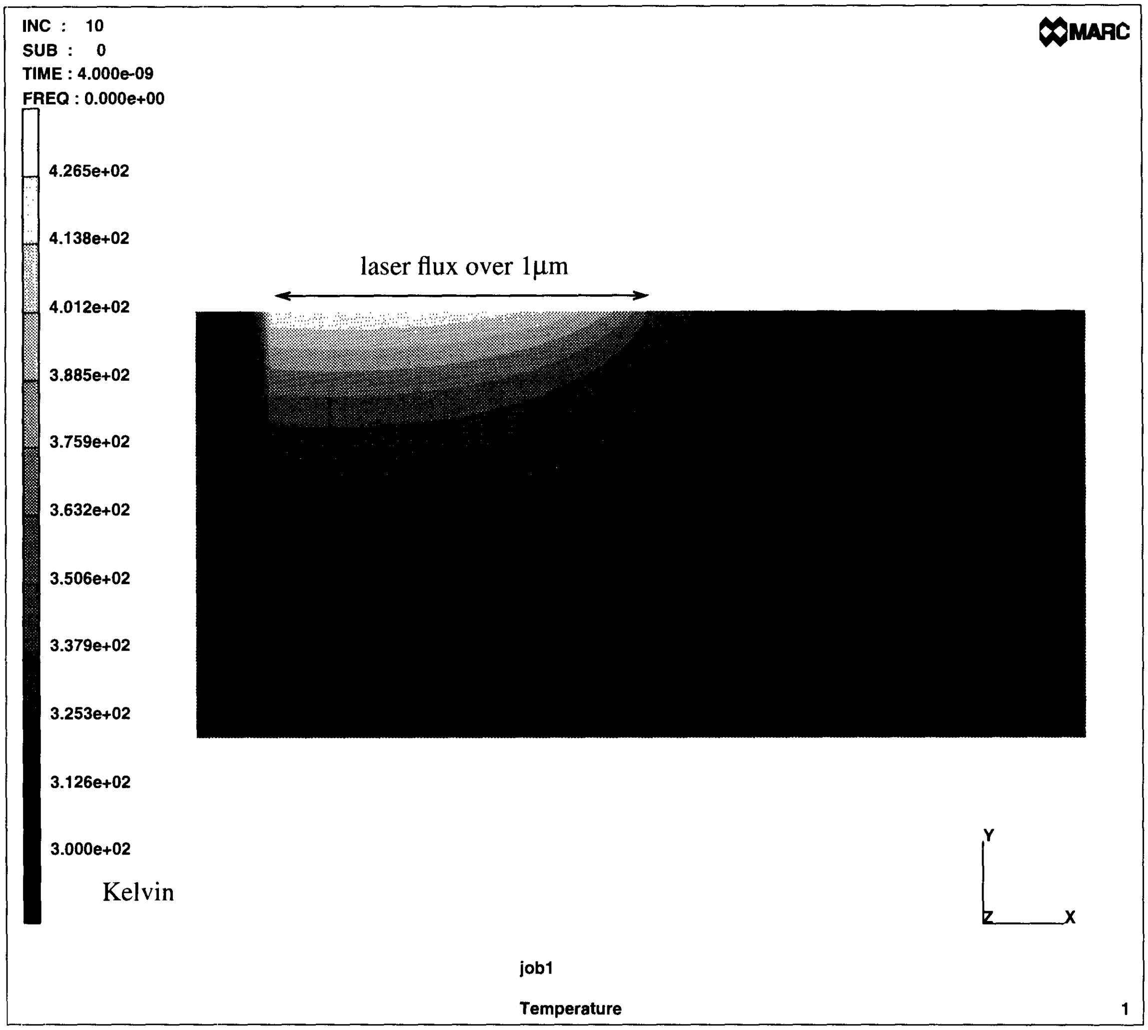

Figure A.2: Thermal profile of Simulation 1 (Al, reflectivity of 97%) at 4 ns (peak of laser flux). Temperature in Kelvin.

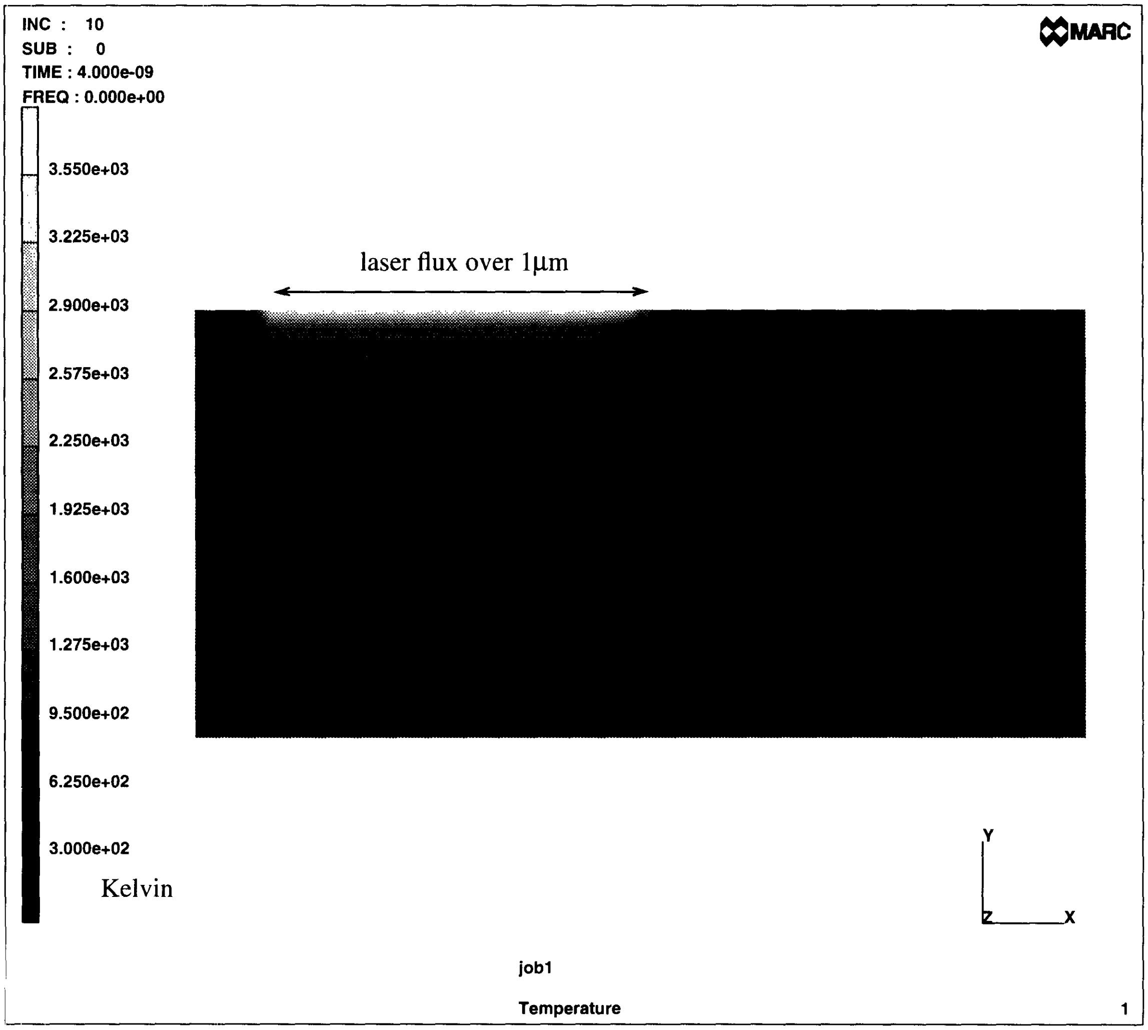

Figure A.3: Thermal profile of Simulation 2 (Ti/Al, reflectivity of 55%) at 4 ns (peak of laser flux). Temperature in Kelvin.

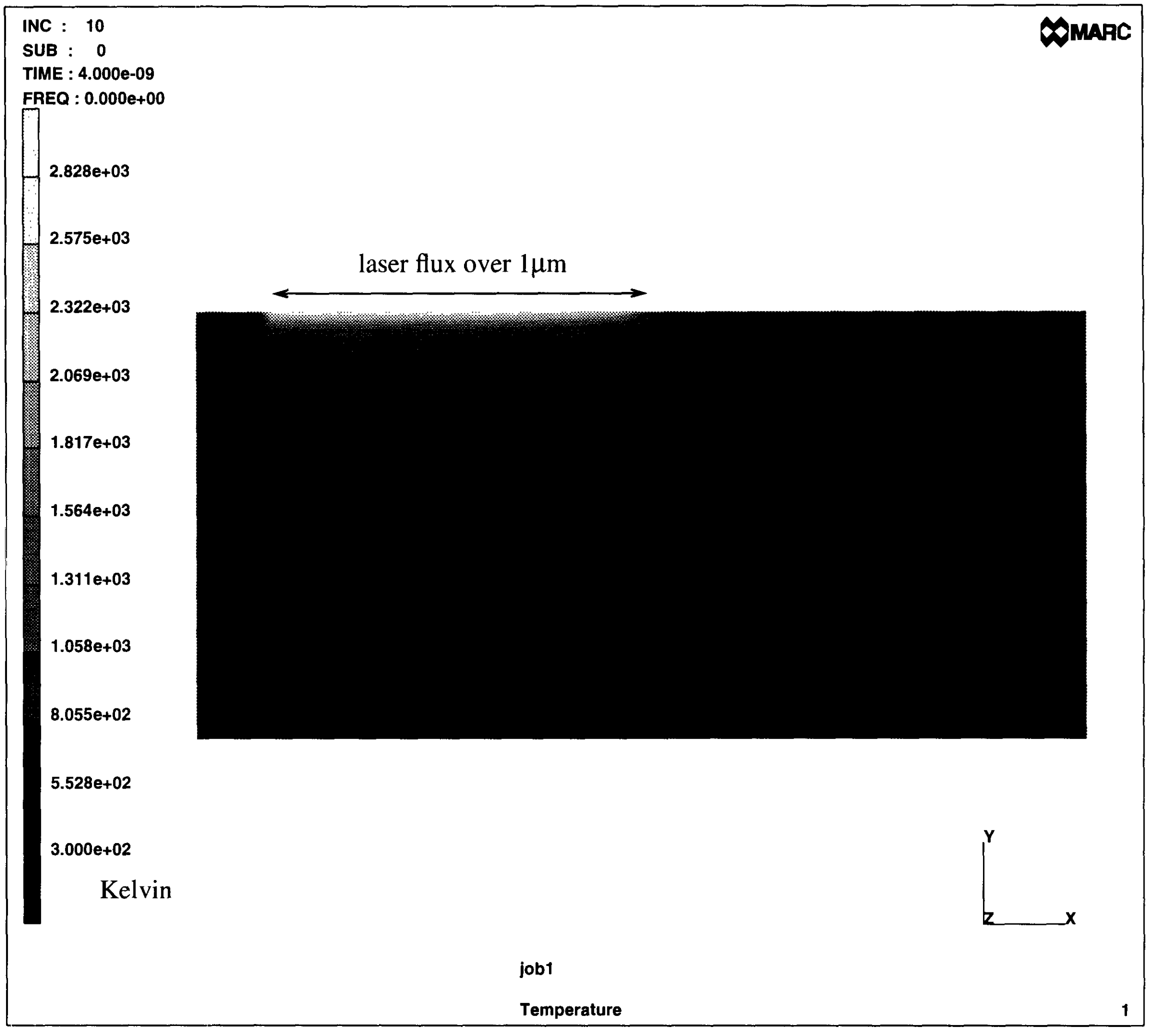

Figure A.4: Thermal profile of Simulation 3 (Ti/Al, reflectivity of 67%) at 4 ns (peak of laser flux). Temperature in Kelvin.

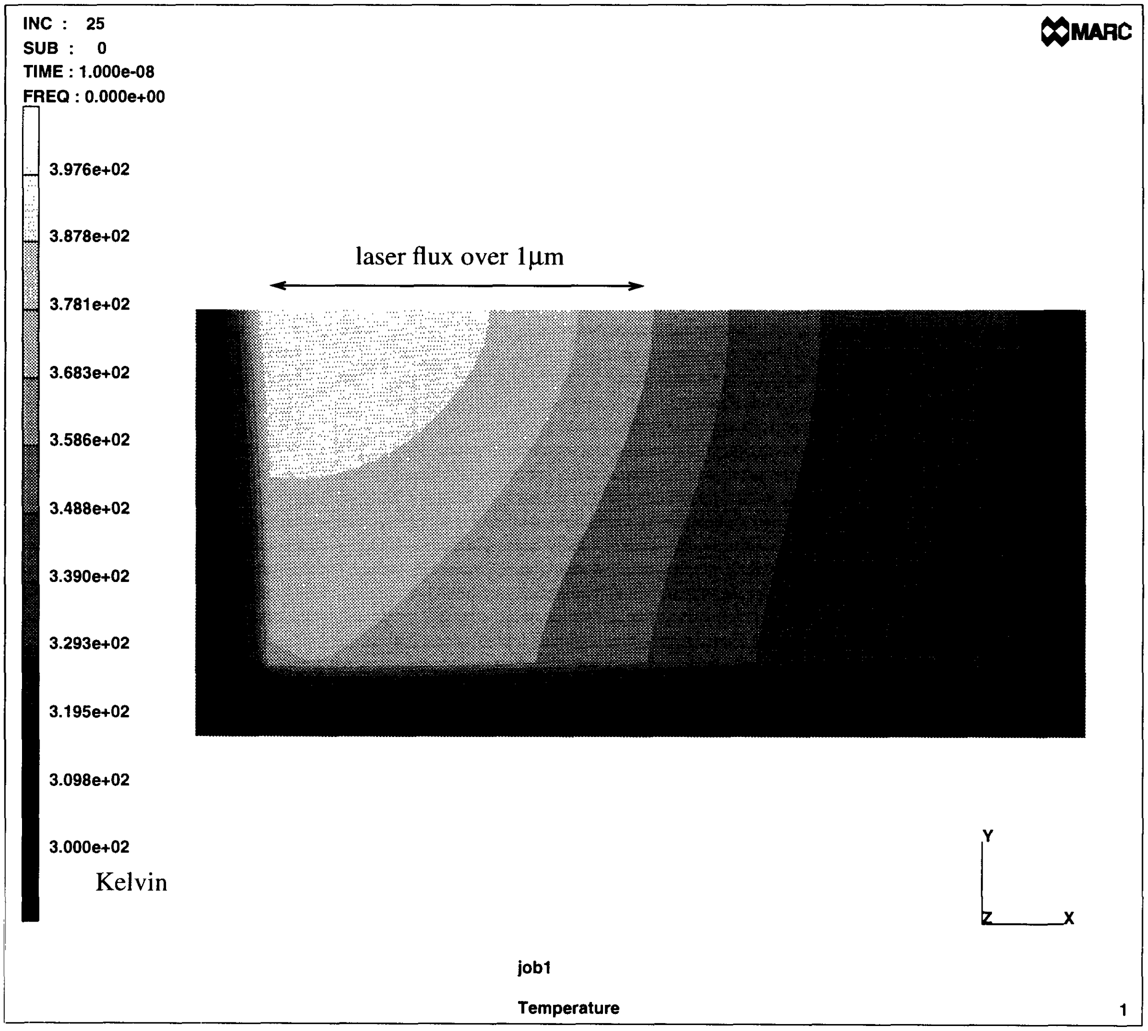

Figure A.5: Thermal profile of Simulation 1 (Al, reflectivity of 97%) at 10 ns (end of laser flux). Temperature in Kelvin.

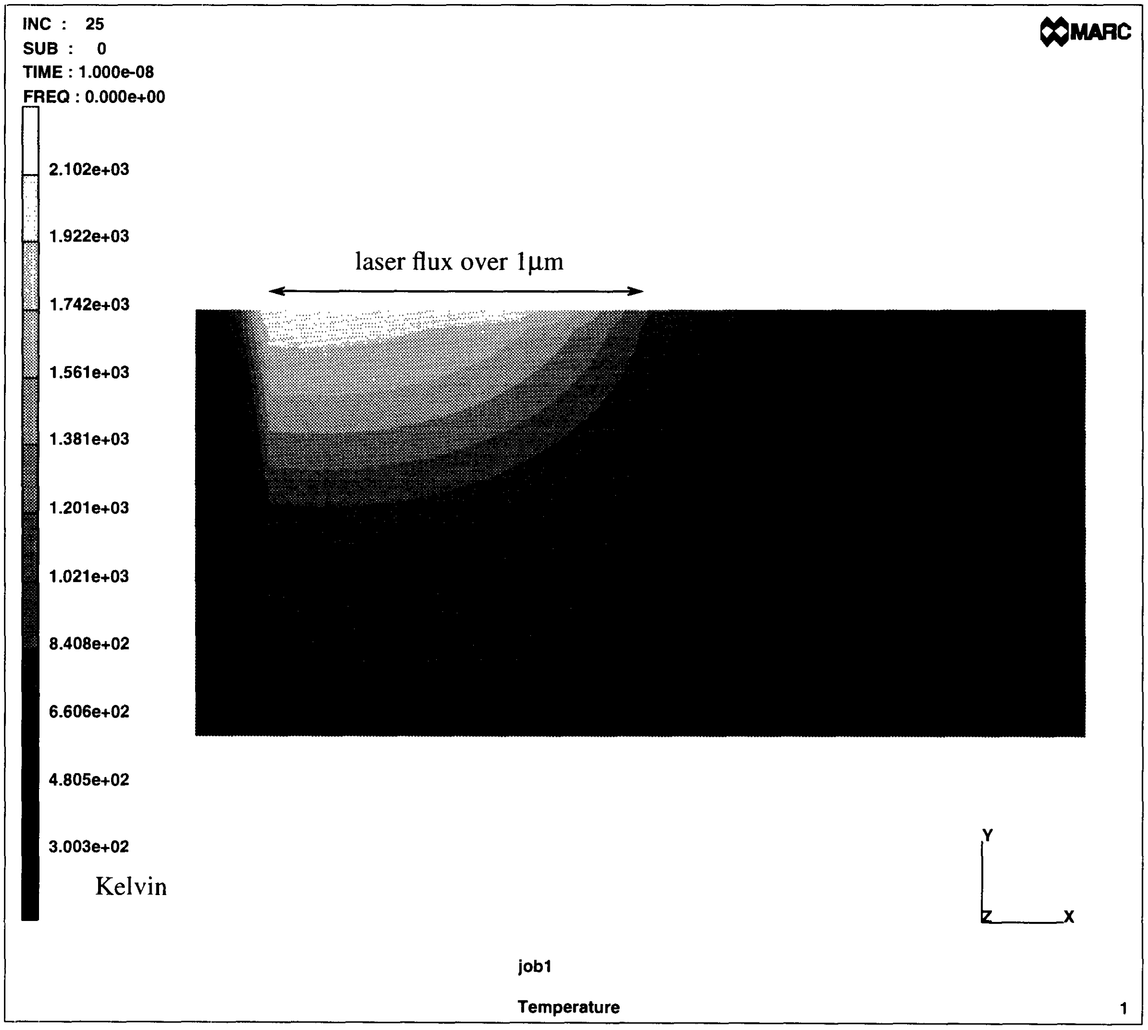

Figure A.6: Thermal profile of Simulation 2 (Ti/Al, reflectivity of 55%) at 10 ns (end of laser flux). Temperature in Kelvin.

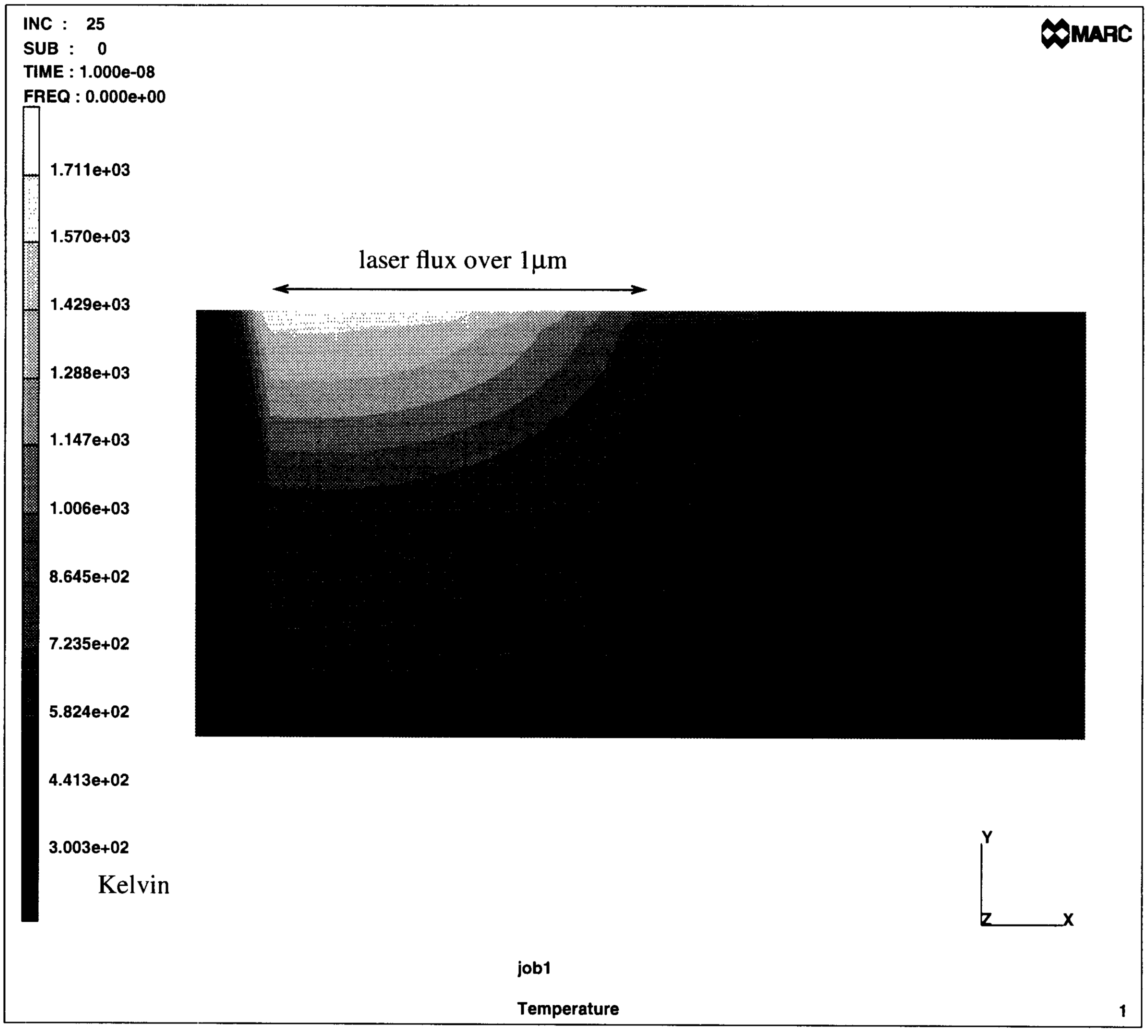

Figure A.7: Thermal profile of Simulation 3 (Ti/Al, reflectivity of 67%) at 10 ns (end of laser flux). Temperature in Kelvin.

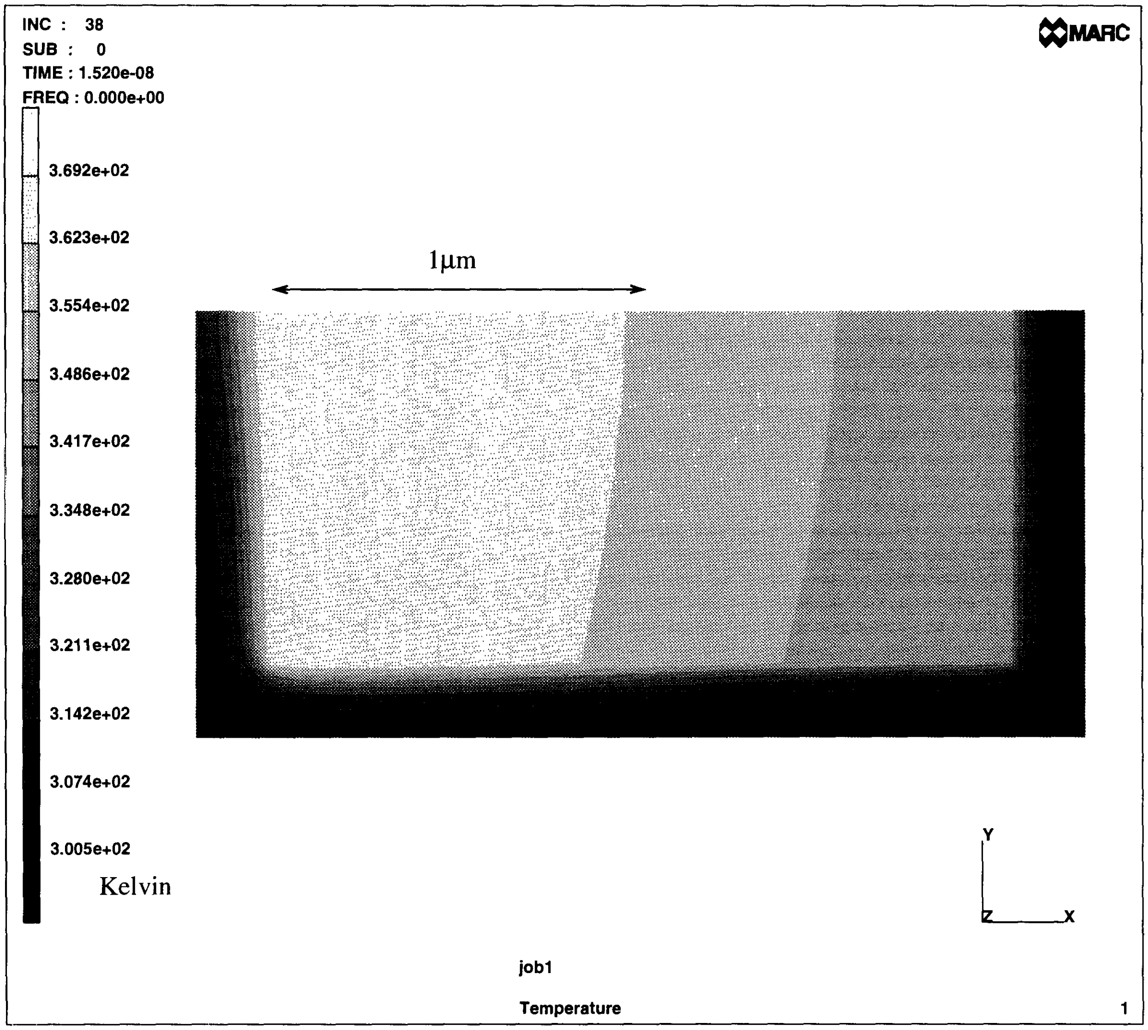

Figure A.8: Thermal profile of Simulation 1 (Al, reflectivity of 97%) at 15 ns (5 ns after the end of the laser flux). Temperature in Kelvin.

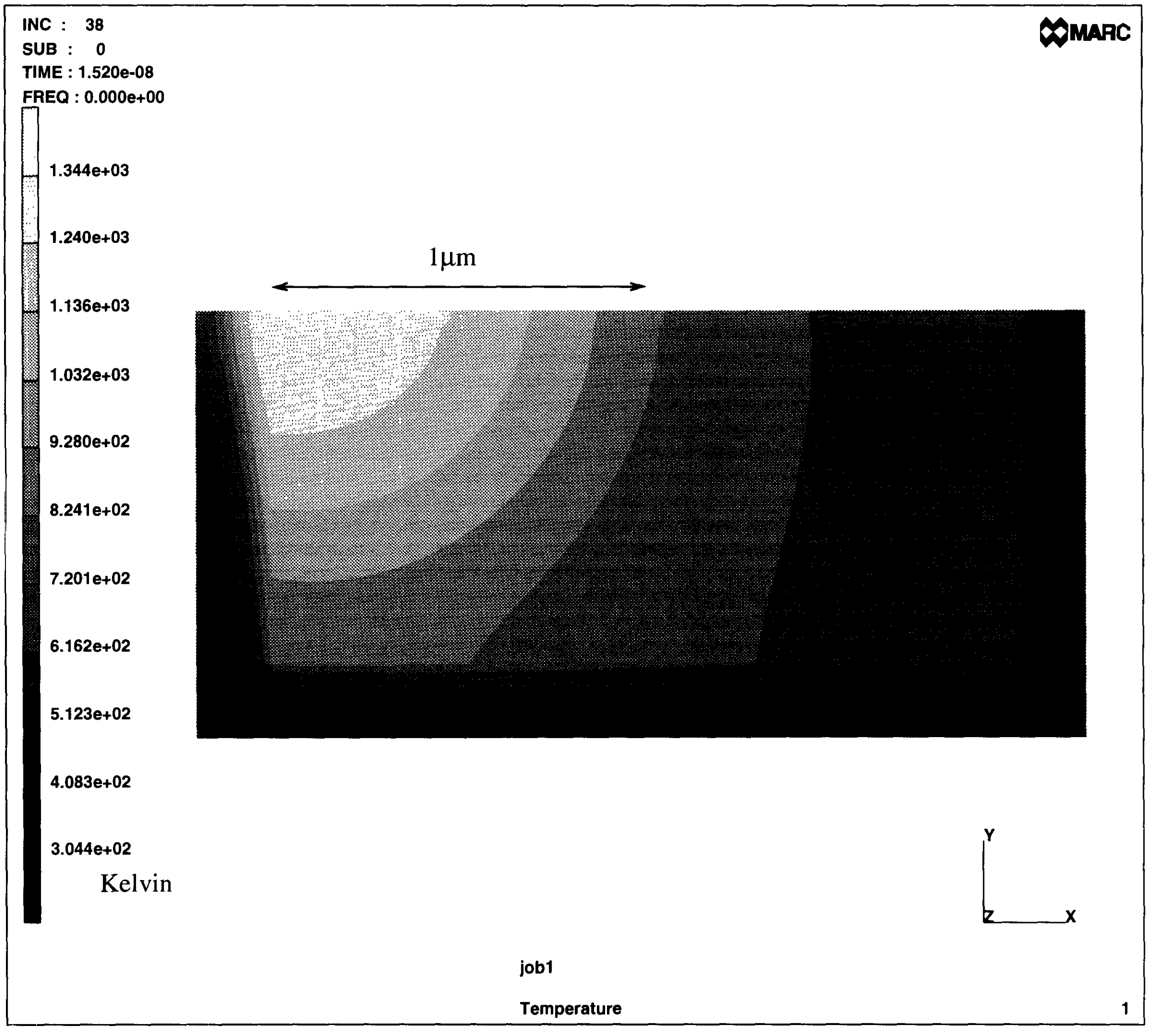

Figure A.9: Thermal profile of Simulation 2 (Ti/Al, reflectivity of 55%) at 15 ns (5 ns after the end of the laser flux). Temperature in Kelvin.

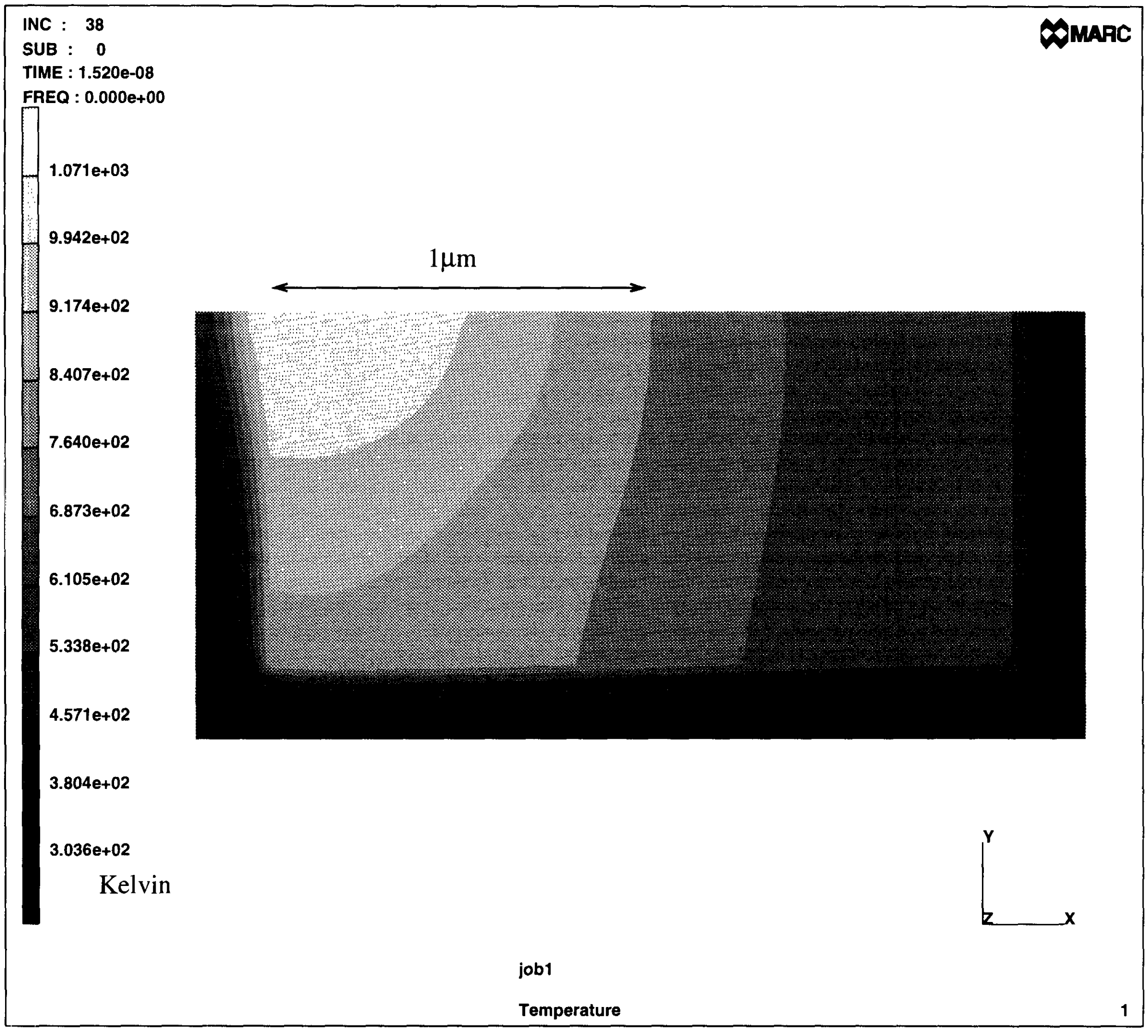

Figure A.10: Thermal profile of Simulation 3 (Ti/Al, reflectivity of 67%) at 15 ns (5 ns after the end of the laser flux). Temperature in Kelvin.

References

[1] M. Cohen, R. Kaplan, and E. Arthurs. "Micro-materials processing." *IEEE*, 70(6):545–555, June 1982.

[2] D. Ehrlich and J. Tsao. *Laser Microfabrication*. Academic Press, Inc., Boston, 1989.

[3] S. Logumer. *Laser Technology*. Prentice Hall, New Jersey, 1990.

[4] G. Matusiewicz, S. Kirck, V. Seeley, and P. Blauner. "The role of focused ion beams in physical failure analysis." *IEEE/IRPS*, pages 167–170, 1991.

[5] K. Gamo, N. Takakura, N. Samoto, R. Shimizu, and S. Namba. "Ion beam assisted deposition of metal organic films using focused ion beams." *Jpn. J. Appl. Phys.*, 23:L293–L295, 1984.

[6] K. Gamo, D. Takehara, Y. Hamamura, M. Tomita, and S. Namba. Microelectronic Engineering, Microcircuit Engineering 86, 1986.

[7] G. Shedd, H. Lezec, A. Dubner, and J. Melngailis. "Focused ion beam induced deposition of gold." *Appl. Phys. Lett.*, 49:1584–1586, 1986.

[8] L. Scarfone and J. Chlipala. "Computer simulation of target link explosion in laser programmable redundancy for silicon memory." *J. Mat. Res.*, 1:368–381, Mar/Apr 1986.

[9] C. Lu, J. Chlipala, and L. Scarfone. "Explosion of poly-silicide links in laser programmable redundancy for VLSI memory repair." *IEEE Trans. Elec. Dev.*, 36(6):1056–1062, June 1989.

[10] H. Yamaguchi, M. Hongo, T. Miyauchi, and M. Mitan. "Laser cutting of aluminum stripes for debugging integrated circuits." *IEEE J. Solid-State Circ.*, SC-20(6):1259–1264, December 1985.

[11] J. Chlipala and L. Scarfone. "Reliability aspects of laser programmable redundancy: Infrared vs. green, polisilicon vs. silicide." *IEEE/IRPS*, pages 163–170, 1989.

[12] K. Nikawa, K. Nasu, M. Murase, T. Kaito, T. Adachi, and S. Inoue. "New applications of focused ion beam technique to failure analysis and process monitoring of VLSI," *presented at the International Reliability Physics Symposium*, Phoenix, AZ, 11-13 April 1989.

[13] R. Smith et al. "Laser programmable redundancy and yield improvement in a 64K DRAM." *IEEE J. Solid-State Circuits*, pages 506–514, 1981.

[14] D. Bursky. "Laser programming turns 10-Kgate arrays around fast." *Elec. Design*, 40:30–31, 28 May 1992.

[15] J. Raffel, R. Frankel, K.Konkle, and J.Murguia. "A laser-restructurable logic array for rapid integrated circuit prototyping." *Lincoln Laboratory Journal*, 4(2):97–112, 1991.

[16] R. Osgood. *IEEE Cir. and Dev. Mag.*, 6(5):25, 1990.

[17] D. Ehrlich. *Appl. Surf. Sci.*, 69:115, 1993.

[18] P. Wyatt and J. Raffel. "Restructurable VLSI – a demonstrated wafer scale technology." *IEEE Proceedings of the International Conference on Wafer-Scale Integration*, pages 13–20, 3-5 January 1989.

[19] J. Raffel, A. Anderson, and G. Chapman. "Laser restructurable technology and design." *Wafer Scale Integration, Chapter 7*, page 363, 1989.

[20] R. Berger, A. Bertapelli, R. Frankel, J. Hunt, J. Raffel, J. Mann, F. Rhodes, A. Soares, and C. Woodward. "The Lincoln programmable image-processing wafer." *Proceedings of the International Conference on Wafer-Scale Integration*, 23-25 January 1990.

[21] R. Berger, R. Frankel, J. Raffel, C. Woodward, and P. Wyatt. "A laser-programmable multichip module on silicon." *Proceedings of the International Conference on Wafer-Scale Integration*, pages 30–35, 20-22 January 1993.

[22] H. Hartmann and T. Hillman-Ruge. "Yield and reliability of laser formed vertical links." *SPIE Proc. Multilevel Interconnections: Issues that Impact Competitiveness*, 2090:146–160, 1993.

[23] M. Rouillon-Martin, M. Chambon, and A. Boudou. "Laser programmable vias for reconfiguration of integrated circuits." *SPIE Proc. Optical Microlithography and Metrology for Microcircuit Fabrication*, 1138:190–197, 1989.

[24] J. Bernstein, T. Ventura, and A. Radomski. "High-density laser linking of metal interconnect." *IEEE Trans. Comp. Pack. Man. Tech.*, 17A(4):590–593, December 1994.

[25] J. Bernstein. "Dielectric fracture leading to metallic connections by laser heating," *presented at Materials Research Society Fall Meeting*, Boston, MA, 1994.

[26] J. Bernstein and B. Colella. "Laser formed metallic connections employing a lateral link structure," *Accepted for publication in IEEE Trans. Comp. Pack. and Manuf. Tech.*, 1995.

[27] I. Banerjee, B. Tracy, P. Davies, and B. McDonald. "Use of advanced analytical techniques for VLSI failure analysis." *IEEE/IRPS*, pages 61–68, 1990.

[28] C. Kim, H. Kim, J. Koo, and S. Choi. "Novel techniques for locating wiring short and open in multilevel interconnection." *Proceedings of VMIC Conference*, pages 323–325, 8-9 June 1993.

[29] S. Prasad and U. Brahme. "LPISEM: A faster approach to asic diagnosis." *SPIE Proceedings*, 2334:280, 20-21 October 1994.

[30] A. DellaRatta. "Focused ion beam induced deposition of copper." Massachusetts Institute of Technology, Master of Science Thesis, 1993.

[31] J. Luxon, D. Parker, and P. Plotkowski. *Lasers in Manufacturing*. IFS (Publications) Ltd., United Kingdom, 1987.

[32] Y. Baiborodin, L. Kriksynov, and O. Litvinenko. *Handbook of Laser Technique*. Kiev, Tehnika, 1978.

[33] R. Clampit and D. Jefferies. *Nucl. Instrum. Methods*, 142:739, 1978.

[34] J. Orloff and L. Swanson. *J. Vac. Sci. Tech.*, 15:845, 1978.

[35] J. Melngailis. *J. Vac. Sci. Tech. B*, 5(2):469, 1982.

[36] P. Prewett and G. Mair. *Focused Ion Beams from Liquid Metal Sources*. Research Studies Press LTD, England, 1991.

[37] G. Taylor and A. McEwan. *J. Fluid Mech.*, 22:1, 1965.

[38] K. Aitken. *Proceedings of Field Emission Day*, ESA, Noordwijk, Holland, page 23, 1976.

[39] A. Wagner and T. Hall. *J. Vac. Sci. and Technol.*, 16:1871, 1979.

[40] S. Papadopoulos. D. Phil. Thesis, Oxford University, 1986.

[41] G. Mair. *Nucl. Instr. and Meth.*, 172:567, 1980.

[42] R. Levi-Setti. *Adv. Electron. Electron Phys. Suppl.*, page 261, 1980.

[43] Y.-L. Shen, S. Suresh, and J. Bernstein. "Laser linking of metal interconnect: Analysis and design considerations," *submitted to IEEE Trans. Elect. Dev.*, 1995.

[44] Y.-L. Shen and S. Suresh. "Thermal cycling and stress relaxation response of Si-Al and Si-Al-SiO_2 layered thin films." *Acta. Metall. Mater.*, in press.

[45] R. Venkatraman and J. Bravman. "Separation of film thickness and grain boundary strengthening effects in Al thin films on Si." *J. Mater. Res.*, 7(8):2040–2048, August 1992.

[46] W. Kingery, H. Bowen, and D. Uhlmann. *Introduction to Ceramics, 2nd ed.* Wiley, New York, 1976.

[47] J. Lloyd and P. Smith. *J. Vac. Sci. Technol.*, A1(2):455–458, April-June 1983.

[48] J. Szekely and N. Themelis. *Rate Phenomena in Process Metallurgy*. John Wiley & Sons, Inc., New York, 1971.

[49] E. Palik. *Handbook of Optical Constants of Solids*. Academic Press, Inc., Orlando, 1985.

[50] J. Weaver, C. Krafka, D. Lynch, and E. Koch. *Physics Data, Optical Properties of Metals, Nr.18-1*. Fach-informations-zentrum, Germany, 1981.

[51] *ASM Metals Handbook, Vol.2, 10th Edition*. ASM International, USA, 1990.

[52] Landolt and Bornstein. *Eigenschaften der Materie in Ihren Aggregatzustanden-Band II, Optische Konstanten-Teil 8*. L&B, Berlin, 1962.

[53] P. Yeh. *Optical Waves in Layered Media, Chapter 5*. Wiley, New York, 1988.

[54] J. Hebb, K. Jensen, and E. Egan. "The potential effect of multilayered patterns on temperature uniformity during rapid thermal processing." *presented at Materials Research Society Spring Meeting*, 17-21 April 1995.

[55] M. Ohring. *The Materials Science of Thin Films*. Academic Press, Inc., Boston, 1992.

[56] S. C. Hsu, S. Chakravorty, and R. Mehrabian. *Metall. Trans.*, 9B:221, 1978.